La borsa di dottorato è stata cofinanziata con risorse del Programma Operativo Nazionale Ricerca e Innovazione 2014-2020, risorse FSE REACT-EU Azione IV.4 “Dottorati e contratti di ricerca su tematiche dell’innovazione” e Azione IV.5 “Dottorati su tematiche Green”

SAPIENZA
UNIVERSITÀ DI ROMA

Multi-scale wind flow observation based on SCADA operative wind turbine data and Satellite Remote Sensing

The Department of Mechanical and Aerospace Engineering
PhD in Aerospace Engineering (XXXVII cycle)

Jacopo Di Cave
ID number 1537736

Advisor
Prof. Maria A. Marsella

Co-Advisor
Prof. Carlo L. Bottasso

Academic Year 2024/2025

Thesis defended

Multi-scale wind flow observation based on SCADA operative wind turbine data and Satellite Remote Sensing
PhDthesis. Sapienza University of Rome

This thesis has been typeset by LaTeX and the Sapthesis class.

Author's email: jacopo.dicave@uniroma1.it

Dedicated to
my family

Abstract

This doctoral thesis investigates the potential use of operational data from wind turbines and wind farms to observe and characterize wind flow distributions around and within the plant at multiple spatial and temporal scales. A major objective is to explore how turbine-level measurements—typically used for operational diagnostics—can be leveraged to enhance wind flow analysis, from the scale of individual turbines to broader wind farm and mesoscale wind field distributions investigated.

At the turbine scale, the study explores the use of operative data to improve the characterization of intra-wind-farm wake interactions, with particular emphasis on applications for wind farm control and real-time performance monitoring. Particular emphasis is placed on the evolution and implementation of engineering wake models and their integration with operational data to capture localized flow dynamics within the wind farm layout.

At the wind farm and mesoscale levels, the thesis examines the integration of SCADA (Supervisory Control and Data Acquisition)-derived wind data with satellite-based wind field observations, particularly those obtained from Synthetic Aperture Radar (SAR) imagery. This integration aims to improve the accuracy and reliability of satellite-derived wind estimates, with significant implications for regional-scale wind monitoring and site assessment in complex coastal environments. A comprehensive review of current satellite wind retrieval techniques is presented, highlighting their limitations and potential, and proposing a novel methodology to combine remote sensing data with in-situ turbine measurements.

Case studies demonstrate how readily accessible operational data can effectively enhance both wind farm control and planning. By leveraging sensors already installed on turbines, this approach presents a cost-efficient strategy that maximizes existing resources. This method not only underscores significant economic advantages but also highlights its potential to drive technological advancements in wind energy management. Overall, this thesis provides practical examples of how turbine SCADA data—typically employed for operational diagnostics—can serve as a valuable observational resource for wind flow characterization across different spatio-temporal scales, with a broad range of applications for the wind energy industry. Furthermore, by integrating these in-situ measurements with remote sensing data—particularly satellite-based wind observations—the proposed approach expands its applicability to wind flow analysis at the wind farm scale, without requiring additional on-site instrumentation.

Contents

Acknowledgements

I would like to express my deepest gratitude to Prof. Carlo L. Bottasso for his invaluable support, constant guidance, and continuous inspiration throughout my PhD journey.

I am also sincerely thankful to Prof. Maria A. Marsella and Prof. Sergio Pirozzoli for giving me the opportunity to undertake this research path and for the encouragement along the way.

Special thanks go to Eng. Daniele Dessi for his helpful advice during the initial phase of the PhD.

I am truly grateful to my colleague and friend Robert for his collaboration and support, and to my other colleagues and friends at TUM for their kindness and availability, which contributed to making my stay at the Wind Energy Department in Munich a truly enriching and memorable experience.

Finally, but most importantly, I would like to thank my family for their unwavering support and encouragement, especially during the most challenging moments of this journey.

List of Abbreviations

Abbreviation	Definition
SCADA	Supervisory Control and Data Acquisition
SAR	Synthetic Aperture Radar
LiDAR	Light Detection and Ranging
OP	Observation Point
TI	Turbulence Intensity
FLORIS	FLOw Redirection and Induction in Steady-State
FLORIDyn	Dynamic extension of the FLORIS model
SOWFA	Simulator for Wind Farm Applications
LES	Large-Eddy Simulation
EnKF	Ensemble Kalman Filter
NNI	Nearest Neighbor Interpolation
REWS	Rotor Equivalent Wind Speed
BEWS	Blade Effective Wind Speed
SEWS	Sector Effective Wind Speed
RMSE	Root Mean Square Error
MAE	Mean Absolute Error
ERA5	ECMWF Reanalysis v5
WRF	Weather Research and Forecasting Model
GMF	Geophysical Model Function
NCRS	Normalized Radar Cross Section
MOST	Monin Obukhov Similarity Theory

List of Figures

Chapter 1

Introduction

1.1 Motivation

Climate change is one of the biggest challenges of our times. According to the UN Emissions Gas Report from 2023 [78], progress has been made since the Paris Agreement was signed in 2015: the increase of Greenhouse gas emissions (GHSs) dropped from an initial prediction of 16% to 3% for the year 2030. However, more efforts still need to be made to limit the rising of Global mean temperature above preindustrial levels: predicted 2030 GHSs still must fall by 28% for the Paris Agreement 2°C pathway and 42% to stay below the 1.5°C limit. Renewable energies will play a key role in meeting these ambitious targets towards the Decarbonization of National economies: the energy transition outlook for 2024 [35], published by the global certification provider DNV, reported that wind energy will contribute to 28% of global electricity generation by mid-century, corresponding to an 8-year-on-year growth in production. This will result, by 2050, in a total global generated wind power capacity of around 6.3 TW, a little less than one-fourth of the predicted total grid-connected capacity worldwide. On the technological side, the wind energy industry is shifting towards the development of wind turbines that are growing in size (**Figure 1.1**). There are two main reasons leading to this trend: first of all, increasing the dimension of the tower the rotor experiences higher wind speeds being less affected by the interaction with the ground. This is particularly relevant for onshore sites, where the morphology of the land affects the distribution of wind resources. Moreover, longer wind turbine blades span a larger rotor area. These two factors result in an overall increase in the power produced by the generator, which is a function of the cubic of the average wind speed blowing over the rotor and the rotor area itself. A turbine larger in rotor size can also reduce the levelized cost of energy ($LCOE$) for regions characterized by low wind intensities.

The offshore sector, in particular, can become a driver for the development of the wind energy industry. Wind speed distributions are usually higher on the seaside than onshore, therefore, on a levelized cost basis, offshore wind projects can sometimes be more cost-effective than onshore ones. Offshore plants also generally raise fewer concerns about visual and noise pollution, being located away from urban areas. On the other hand, managing large power plants located at the seaside presents different levels of complexity, not only related to the installation of the

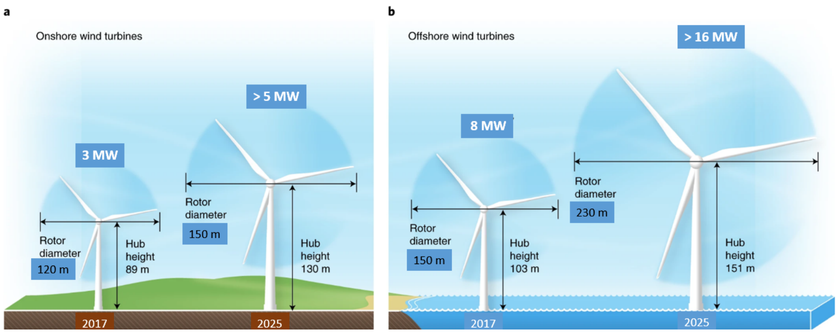

Figure 1.1. Size growth of commercial wind turbine (example trend) [59], [77], [30]
.

turbines but also to activities related to site assessment and the O&M (Operation and Maintenance) of the wind farm. The interactions between the wind flow and wind farms have a relevant influence on the productivity and endurance of the plant itself and neighboring clusters of turbines. At the Mesoscale level, the whole wind farm behaves as a "blockage" of porous disks to the incoming flow, reducing the average wind speed upstream of the plant. The intensity and extension of the "blockage - effect" are a consequence of the ambient conditions(i.e. wind direction, atmospheric stability, etc), the site, and plant layout. Moreover, the flow downstream of the wind farm is characterized by a reduced wind speed and increased turbulence levels resulting from the kinetic energy extraction by the turbines. The latter, called cluster wake, can propagate over distances in the order of tens of kilometers offshore in conditions of stable and neutral atmospheric stability, thus affecting the power output and the endurance of downstream plants. This means that production for clustered projects will be lower than for projects built in isolation. While different models are available in the literature for the wake of the single turbines, there is still a lack of computationally affordable models able to fully capture the physics and estimate the influence of cluster wakes and blockage on power plant production. With a trend towards the rising of offshore wind energy utilization now that industry and authorities have started to plan wind parks closer together for different reasons (e.g. nature conservation, bundling of grid access, public acceptance), cluster wake shadowing effects will occur to an increasing degree, leading to power losses and uncertainties in offshore wind resource assessment alongside the monitoring of existing plants. The size of wind farm-induced effects can extend the order of km. A multisensor approach could provide a valuable solution to fully investigate the physics of this complex phenomenon. Different studies analyzed the effects on energy yield of cluster wakes and blockage with a combination of Remote Sensing technologies, namely LiDARs, Doppler Radar and SAR (Synthetic Aperture Radar) with SCADA data. Given the spatial coverage of remote sensing technologies, especially SAR, they provide a fundamental tool to asses the extension and the effective presence of cluster wakes on downstream wind turbines. Also on a wind turbine scale, as mentioned before, given the growing size of wind turbines, the point measure provided by the nacelle anemometer can not give a representative knowledge of the wind flow blowing over the rotor area of the turbine which is essential for monitoring the state of the machines and provide information for the necessary wind farm control actions (eg., wake steering, pitch control, etc.). Nacelle LiDARs or LiDARs, in general, can provide a complete scan of the inflow but are an expensive technology, requiring the installation of other sensors. Wind sensing technologies, such as the one developed by [69, 20] correlate the bending loads to the distribution of the inflow, providing an economic and valuable solution based on sensors normally installed on the turbines (estensimeters, accelerometers, rpm, SCADA, etc.). This PhD thesis follows the steps of the works investigating the use of operative SCADA data to infer information about the wind speed distribution around and inside the wind farm on different spatial and temporal scales.On the wind turbine scale, the application of wind sensing methodologies which essentially turn the rotor into an anemometer for monitoring and wind farm control applications are investigated. The measurements provided by a wind observer over the rotor are used to correct the prediction of a low-fidelity wake model to provide a solution for wind farm control and monitoring at low computational cost. On the mesoscale level, operative wind turbine data are compared and combined with satellite acquisitions. The focus of this part of the thesis is the introduction of a methodology to recalibrate SAR-inferred wind speeds extrapolated to hub height around a wind farm, using solely operational data directly available from the wind farm itself. This approach effectively turns the entire plant into a cluster of in-situ sensors. Preliminary results from the analysis of an existing offshore wind farm show that, even without installing additional sensors such as LiDARs (Light ranging and detection) or employing complex algorithms, the information contained in anemometric SCADA data can potentially improve the quality of SAR extrapolations—addressing one of the key challenges in applying this remote sensing technology. The ultimate goal of this study is to provide a first step toward developing a cost-effective data fusion approach that combines publicly available satellite imagery (e.g., from Sentinel SAR sensors) with operational wind farm data. Such a method could be employed for site assessment and monitoring purposes, including analyzing the effects of coastal wind gradients on plant productivity.

1.2 Wind Turbine and Wind Farm flows

This section provides an overview of the wind flow regions that develop within and around the wind farm, resulting from its interaction with the plant [65], as reported in **Figure 1.2** .

The wind resource is highly variable over a wide range of spatial and temporal scales, affecting the productivity of a wind farm: Macroscale and mesoscale weather phenomena are responsible for the variability of the inflow in the free atmosphere at horizontal length scales larger than approximately 2000 km, and in the range of 2–2000 km, respectively **Figure 1.3**.

Warm air masses rise up from areas where the insolation is stronger, closer to the equator, and circulate in the atmosphere to sink back to the surface in cooler areas. The resulting global circulation patterns of the air are strongly influenced by Coriolis forces due to the earth's rotation. The non-uniformity of the earth's topography (e.g., because of the presence of mountains, hills, etc.), the presence of obstacles such as buildings, vegetation, and wind turbines, and thermal effects

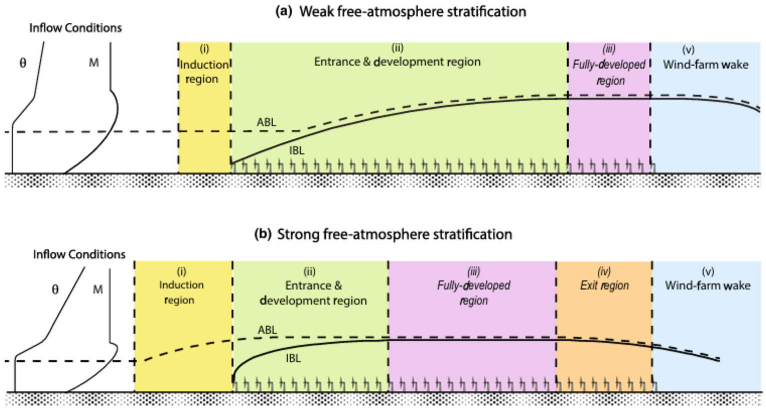

Figure 1.2. Wind flow distribution resulting from the interaction of a large finite-size wind farm with a conventionally neutral atmospheric boundary layer (ABL) under (a) weak and (b) strong free-atmosphere stratification. Inflow conditions are represented by vertical profiles of mean potential temperature (θ) and mean wind speed (M) [65].

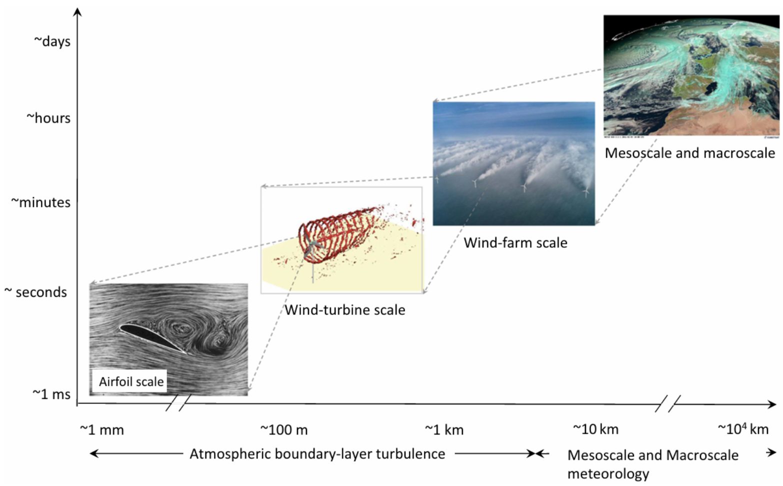

Figure 1.3. Spatio-temporal distribution of the wind flow scales relevant for wind energy [65].

related for instance to the difference in temperature between sea and earth's surface on coastal areas introduce additional variability on smaller regional and local spatial scales into the wind flow distributions. At a given location, wind fields might also present a temporal variability on different scales. Large-time scale variability refers to slow, long-term wind speed variability from one year to the other, with even longer scale variations on the order of decades or more. These long-term variations are very complicated to predict and may make it difficult to realize accurate predictions of the economic viability of particular wind farm projects. On the other hand, for timescales shorter than a year, seasonal variations are much more predictable [29]. The Weibull distribution function has been found to give a good representation of the variation in hourly mean wind speed over a year at many typical sites. However, there are still large variations on shorter timescales than seasonal changes, which, although reasonably well understood since they follow definite patterns, are often more random and not very predictable before than a few days ahead. These are the 'synoptic' variations, which are associated with large-scale weather patterns, such as areas of high and low pressure and associated weather fronts as they move across the earth's surface. The Coriolis forces induce a circular motion of the air as it tries to move from high to low-pressure regions. These coherent large-scale atmospheric circulation patterns may typically take a few days to pass over a given point, although they may occasionally 'stick' in one place for longer before finally moving on or dissipating. The frequency content of these variations typically peaks at around four days or so. Depending on location, there may also be considerable variations with the time of day (diurnal variations), which again are usually fairly predictable. On these timescales, the predictability of the wind is important for integrating large amounts of wind power into the electricity network, to allow the other generating plant supplying the network to be organized appropriately. Shorter timescales, in the order of minutes down to seconds or less, are characterized by fast wind speed variations, known as turbulence, which can have a very significant impact on the design and performance of the individual wind turbines, as well as on the quality of power delivered to the network. Turbulence refers to fluctuations in wind speed on a relatively fast timescale, typically defined as less than about ten minutes. To define the turbulence, the wind could be considered as consisting of a mean wind speed determined by the seasonal, synoptic and diurnal effects, which varies on a timescale of one to several hours, with turbulent fluctuations superimposed. Therefore, these turbulent fluctuations present a zero mean when averaged over about ten minutes. Turbulence is generated mainly from two causes: 'friction' with the earth's surface, which refers to flow disturbances caused by topographical features such as hills and mountains;and thermal effects which can cause air masses to move vertically as a result of temperature variations and, hence, in the density of the air. Often these two effects are interconnected. Turbulence is a complex process, that cannot be represented simply in terms of deterministic equations, but it is generally more useful to develop descriptions of turbulence in terms of its statistical properties. A common way to characterize the turbulence is using the turbulence intensity (TI) index, which is a measure of the overall level of turbulence [29]. It is defined as:

$$TI = \frac{\sigma}{\bar{U}} \tag{1.1}$$

where σ is the standard deviation of wind speed variations about the mean wind speed $\bar{U}$, usually computed over a time frame of ten minutes or an hour. Turbulent wind speed variations can be considered to be roughly Gaussian, meaning that the speed variations are normally distributed, with standard deviation σ, about the mean wind speed $\bar{U}$. However, the tails of the distribution may be significantly non-Gaussian. The TI depends on the roughness of the ground surface and the height above the surface. However, it also depends on topographical features such as hills or mountains, especially when they lie upwind, as well as more local features such as trees or buildings. It also depends on the thermal behavior of the atmosphere: for example, if the air near the ground warms up on a sunny day it may become buoyant enough to rise up through the atmosphere causing the generation of turbulent eddies. The lower portion of the atmosphere in proximity to the earth's surface, called the atmospheric boundary layer (ABL), strongly influences the characteristics of the inflow and the turbulence that are perceived by the wind turbines [79], [64]. In this area, the atmospheric variables change from their free atmosphere characteristics to the surface values: wind speed changes from the free wind aloft to zero at the ground, while scalars, like temperature and humidity approach their surface values. The properties of the Boundary layer are the result of the complex interaction among the different aforementioned phenomena including the intensity of the geostrophic winds, the surface roughness on the ground, Coriolis effects due to the earth's rotation and thermal effects.

As far as the influence of thermal effects is concerned, it can be classified into three main categories: stable, unstable, and neutral stratification (**Figure 1.4**). Unstable

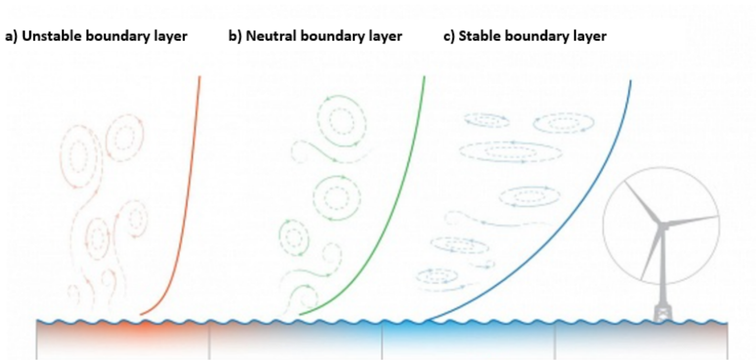

Figure 1.4. Average vertical wind shear profiles associated with (a) unstable (b) neutral (c) stable atmospheric stratification.

stratification occurs when surface heating causes warm air near the surface to rise. As it rises, it expands due to reduced pressure and therefore cools adiabatically. If the cooling is not sufficient to bring the air into thermal equilibrium with the surrounding air, then it will continue to rise, generating large convection cells. In this condition, the development of a thick boundary layer takes place with large-scale turbulent eddies. The high rate of vertical mixing and transfer of momentum in unstable conditions determines a relatively uniform wind shear profile characterized by small variations of mean wind speed with height. If the adiabatic cooling effect causes the rising air to become colder than its surroundings, its vertical motion will be suppressed. This condition is known as stable stratification. It often occurs on cold nights when the ground surface is cold. In this situation, turbulence is dominated by friction with the ground and wind shear, the increase of mean wind speed with height, can be large. In the neutral atmosphere, the adiabatic cooling of the air as it rises is such that it remains in thermal equilibrium with its surroundings. This is often the case in strong winds when turbulence caused by ground roughness causes sufficient mixing of the boundary layer. For wind energy applications, neutral stability is usually the most important situation to take into account, particularly when considering the turbulent wind loads on a turbine, because these are the largest in strong winds. Nevertheless, unstable conditions can be important because they can result in sudden gusts from a low level, and stable conditions can give rise to significant asymmetric loadings due to high wind shear. In other words, the atmospheric stability of the ABL is a measure of the degree of mixing in the air. When the heat flux is positive (the ground is warmer than the air) the atmosphere is characterized by rising air. The shear-produced eddies are enhanced by the thermal structure, and the situation is denoted as thermally unstable. If the heat flux is downward, the shear produced eddies and the general fluctuation level is diminished, for which reason the situation is denoted stable. The enhance mixing for unstable conditions reduces the wind shear, while the reduced fluctuation level for stable conditions allows a larger wind shear. Therefore, the resulting structure of the ABL is unsteady (because of the effects introduced by Synoptic forcing variations and diurnal cycles), non homogeneous (because of surface topography and roughness), and turbulent due to the interplay between thermal and mechanical (frictional) effects.Therefore, given the unsteadiness of the inflow, the determination of power performance and the optimization of the layout of the wind farm is a complicated task.

This thesis focuses on analyzing the interaction between the flow and the wind farm, both on the intra-turbine scale within the plant and on the larger wind farm scales (**Figure 1.3**). At turbine scales the single machine acts as a porous disk for the incoming flow, reducing its speed compared to the freestream conditions and, therefore, the effective available power for the machine. This upstream region is called the induction zone, The area downstream of the wind turbine, called wake, is characterized by a lower mean wind speed because of the extraction of kinetic energy from the main flux and increased turbulence, resulting in reduced available wind power and increased harmful loads for downstream wind turbines. During the downstream propagation of the wake, the advection of external flows , determined by the exchange of momentum with the ambient non-perturbed surrounding flow, causes the contemporary wake expansion and the reduction of the wind speed deficit until the full recovery of the original wind speed. The instantaneous and the time-averaged wind speed profiles of the flow regions generated from the interaction between the wind turbine and the incoming turbulent boundary layer are reported in **Figure 1.5** and **Figure 1.6** respectively. As it is reported in the figures, the wake itself can be further divided into two regions with different characteristics, namely the near-wake and the far-wake. The near-wake is the region immediately downstream of the wind turbine. Its extension can reach a distance up to 2-4 D (two to four times

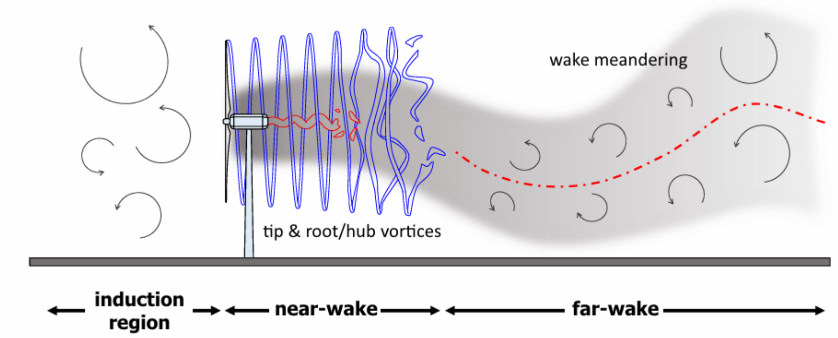

Figure 1.5. Instantaneous schematic profiles of the wind flow regions generated by the interaction of a wind turbine with the incoming turbulent boundary layer [65]

the diameter of the rotor). It is characterized by a highly unsteady and non-uniform inflow because of the shedding of 3D periodic vortexes from the blades and the hub (**Figure 1.5**). The frequency of the helicoidal root and tip vortices is three times higher than the rotor speed [65].

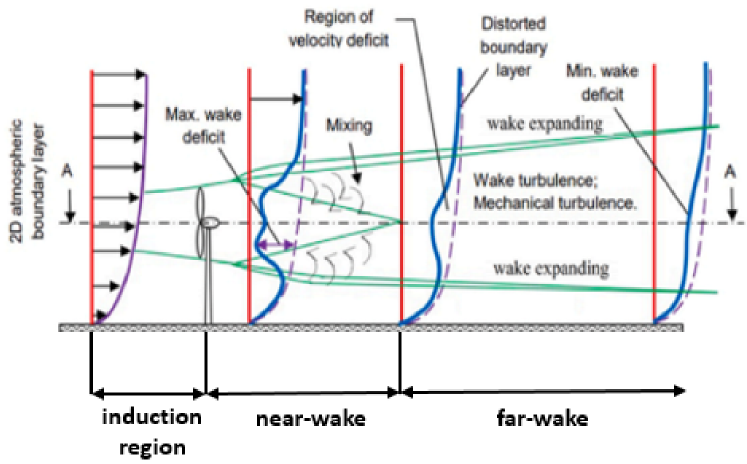

Figure 1.6. Time-averaged schematic profiles of the wind flow regions generated by the interaction of a wind turbine with the incoming turbulent boundary layer [65], [81]

The length of the near-wake with the associated breakdown of the vortices is correlated to different factors, including the tip speed ratio, the wind shear, the turbulence intensity of the incoming flow, and the mechanical shear generated from the wind turbine. The further downstream region, also known as far-wake, on the other hand, shows less dependency on the geometry of the turbine. In this area, the presence of large eddies, with characteristic dimensions greater than the size of the rotor diameter, can induce large low-frequency fluctuations of the entire wake with respect to the time-averaged wake centerline, referred to as Wake Meandering [52]. These random fluctuations of the whole wake provoke fatigue loads and power fluctuations on downstream wind turbines. A common characteristic observed in different simulation and experimental analyses of the wake meandering is the larger displacement in the lateral direction compared to the vertical one and the growth of the fluctuations with the distance downstream from the wind turbine. This effect is supposed to be correlated to the lateral meandering tendency in large turbulent structures of the incoming inflow and the constraining effect of the ground [65]. The study of wake evolution in these two regions is crucial for monitoring and optimizing the power performance of existing wind farms. Offshore wind turbines are typically spaced between 3 to 10 rotor diameters (D), placing them within the far-wake region. However, this spacing is not always feasible for onshore wind farms, where site constraints and project-specific requirements often result in a denser turbine layout. In some cases, turbines are spaced at distances shorter than the transition region between near and far wakes. Such compact arrangements can lead to substantial power losses and increased fatigue loading on downstream turbines, particularly under certain wind directions. **Figure 1.6** reports the mean profile of the wake distribution behind the wind turbine both for the near-wake and the far-wake. Different experimental and simulation studies have shown that the difference between the incoming flow speed and the wake, known as the velocity deficit, exhibits two peaks behind the rotor and is modeled as a double-Gaussian profile [68]. Further downstream, in the far wake region the shape of the wake becomes more regular, resembling a symmetric Gaussian profile except for the edges of the wake [12], [65]. Therefore, the resulting wake velocity trends present a distortion in the shear profile compared to the incoming flow. The rate of wake expansion and recovery is strongly influenced by the characteristics of the incoming atmospheric boundary layer. The wake width generally increases almost linearly with downstream distance from the wind turbine. Moreover, the wake recovery rate is higher in boundary layers with elevated atmospheric turbulence intensity. Surface roughness also contributes mechanically to the generation of turbulence, which is typically lower in offshore environments. This is the reason why offshore wind farms have, in general, lower capacity density than their onshore counterparts [65]. On the other hand offshore wind farms are also subject to reduced fatigue loads associated with wake-induced turbulence. In fact, as previously mentioned, another characteristic of the wake is the generation of additional turbulence in the downstream flow. The latter reaches its higher value on the top edge of the wake at the transition zone between the near and the far-wake regions. Different analytical models have been proposed in the literature to capture the main features of the average inflow behind the wake distributions [7]. The development of reliable Engineering models to describe the propagation of the wake is essential for applications such as wind farm control, monitoring, and layout optimization, where it is necessary to run multiple simulations before an optimal solution is found or achieving a real-time solution at low computational cost is crucial [38], [18]. The thermal stability of the ABL has also a large influence on the propagation of the wake since it affects the profile of the wind shear and the turbulence intensity in the incoming flow [29], [65].

Neutral and stable boundary layers are characterized by less momentum exchange and less turbulence. In this condition, the wake recovery is slower and the meandering of the wake is less accentuated compared to convective boundary layers, which, on the other hand, are characterized by higher TI and the presence of large scale turbulence structures, provoked by the convective movements triggered by the temperature difference between the earth/ sea surface and the upper levels of the atmosphere. In these unstable conditions, the brake of the vortexes in the near wake takes place more quickly at less distance from the wind turbine and also the Wake recovery and expansion are faster because of the higher exchange of flux momentum, but the production of TI increases as well. Atmospheric stability also has an influence on the fatigue loading of wind-turbine blades [65]. For example, increased atmospheric stability has been shown to increase the fatigue loading associated with mean wind shear, while it decreases the fatigue associated with turbulence. It should be mentioned that Stable ABL (SBL) is characterized by both a large vertical shear, associated with the relatively shallow depth, and a large lateral shear **Figure 1.4**), due to the change of wind direction with height produced by the Coriolis force. In some cases, the SBL can be so shallow that part of the rotor disk (or even the entire rotor, as shown in some field data) lies above it; in such cases, although the flow above the SBL is non-turbulent, the intermittent turbulence and bursting events commonly found at the top of the SBL can pose hazardous structural threats to wind-turbine blades. Moving from the turbine scale to the wind farm scale, it is possible to identify different regions resulting from the interaction between the whole plant and the flow (**Figure 1.2**). In the region upwind of the wind farm, besides the blockage of individual wind turbines, a cumulated blockage effect induced by the wind farm as a whole, called the wind-farm induction zone takes place. The whole wind farm behaves as a blockage to the incoming flow, reducing the average wind speed upstream at hub height. This produces a deceleration of the incoming boundary-layer flow and its deflection upwards and sideways, at the edges of the plant, due to mass conservation [29], [65]. The extent and strength of the farm induction region depends on the complex interplay between wind-farm size,layout, wind direction, turbine spacing, and thrust coefficient [25], [73]. Using both a cylindrical vortex wake model and actuator-disk simulations, it was shown that the wind speed at a distance of 2.5D in front of a wind farm may easily be reduced by 3% with respect to the actual incoming flow speed [25]. This reduction is similar to wind speed decrease derived from the RANS approach [22] as well as LES [65], for the case of wind farms inside a neutral ABL capped with a thermally-stratified free atmosphere (also known as a conventionally-neutral ABL) with relatively small lapse rates. A wind speed decrease of 4% over a distance of 25 D (2.9 km), upstream of wind turbines operating at high thrust coefficient, was observed in field measurement from a LiDAR in stable atmospheric conditions [67]. Different studies also showed that the extent and strength of the induction region, and therefore its effect on power losses in the wind farm, can be substantially larger in the case of a shallow conventionally-neutral ABL with relatively strong free-atmosphere stratification. This is due to the fact that, in such a case, the flow becomes subcritical and, therefore, the upward flow deflection induced by the wind farm triggers standing gravity waves, which are responsible for further flow blockage, also referred to as choking [22], [6], [58], [51]. Within some downwind distance from the upstream row of turbines, the flow is highly heterogeneous because of the presence of individual turbine wakes. Further inside the wind farm, the different turbine wakes expand and interact with other wakes, leading to a flow that remains highly heterogeneous at turbine level, but becomes more homogeneous at the upper part of the flow region influenced by the turbine wakes. This region is defined as the internal boundary layer (IBL).For large enough wind farms, the IBL reaches the top of the ABL and starts to grow with it by entraining momentum from the free atmosphere. This growth of the ABL continues further downwind until the flow reaches the fully-developed state. In this zone, the entire boundary-layer flow is fully adjusted to the wind farm and, therefore, the spanwise- and row-averaged flow is homogeneous in the streamwise direction. The power extraction by the wind turbines is balanced exclusively by the turbulent vertical transport of kinetic energy entrained from the flow above. This asymptotic case also referred to as the infinite wind-farm case, has been extensively studied in the literature [65]. The fully-developed regime could be attained after distances of one order of magnitude larger than the ABL height; however, LES studies of very large wind farms in the conventionally-neutral ABL have shown that much longer distances (about two orders of magnitude and larger) are required to achieve the fully-developed wind-farm flow [83]. More details on the fully-developed wind-farm flow are given in [65]. The region downwind of the wind farm is the wind-farm wake region as shown in **Figure 1.2**. The wind farm wake flow, which is the result of the cumulative effect of the wakes of all the turbines in the wind farm, recovers momentum with increasing downwind distance until the wake is negligible and the flow resembles that upwind of the wind farm. Satellite measurements [66] and numerical simulations [83] have shown that wind-farm wakes can have non-negligible effects on the surface-layer wind speed, which retains a 2-4% deficit at downwind distances from the farm in the range of 5-55 km, depending on the ambient stability and wind-farm size. Therefore, understanding and predicting these farm wake flows is essential to minimizing farm-to-farm interactions when large plants are to be deployed in proximity to each other. This is the case, for example, in the North Sea, where multiple wind farms are planned due to the combination of favourable high wind speeds and shallow water conditions [66], [62]. Different studies showed the extension over long distances, in the order of tens of kilometers offshore, in conditions of stable and neutral atmospheric stability, due to the lack of topology and surface roughness of the sea. This means that the production for clustered projects will be lower than for projects built in isolation. While several models are available in the literature to describe the wake of single turbines, a knowledge gap remains in accurately estimating the effects of wakes—and in particular blockage—on the production of offshore wind farm projects, where the proximity of neighboring farms becomes critical. The magnitude and design implications of cluster wake effects in large wind farm clusters are still the subject of ongoing debate within both the research and industrial communities. Some analysts and operators argue that wind farm wakes can significantly alter inflow conditions and energy yield, thereby requiring adaptations in layout or operational strategies, whereas others consider their practical impact secondary to economic or grid-driven design constraints. As discussed in [40], none of the mitigation or design strategies proposed so far have been able to reduce these effects by more than a small percentage. On the contrary, changes in layout design or control strategies often result in a deterioration of performance at the upstream farm that outweighs, by orders of magnitude, the gains at the downstream farm—ultimately leading to an overall net loss of output compared to scenarios without mitigation. Quantifying the impact of such effects on power output and structural loads, as well as evaluating the effectiveness of potential mitigation strategies, is therefore expected to become increasingly important given the ongoing trend toward larger turbines and denser offshore wind farm developments [35].

1.3 Wind field Observations: state of art

As described in the previous paragraph, the wind field around and inside a wind farm is the result of a complex interaction between different phenomena such as atmospheric effects and the morphology of the site where the plant is located. A wide range of spatiotemporal scales going from small fast fluctuations due to the turbulent nature of the flow to long-therm large eddies that can cover distances multiple time the rotor diameter of a wind turbine or even more plants are involved in this interaction. Different kinds of sensors therefore are more suitable according to the dimension of the area of interest, the wind-related scale under observation and the temporal resolution demanded [64].

The most common instruments used for wind energy applications are anemometers, which are among the oldest devices for wind measurement [15], [44]. They can provide punctual measurements of the inflow, and nowadays, different typologies are available, ranging from basic mechanical to high-tech devices. Wind velocity measurements are generally split into standard meteorological and micro-meteorological observations. The former are measured on scales from several minutes and larger, while the latter happen on far smaller scales down to instantaneous measurement. Nowadays a multitude of different anemometer types are available. Mechanical, propeller or cup anemometers (**Figure 1.7**) have their main use in standard measurements. They are characterized by high reliability, large dimensions, and delayed action, due to their moment of inertia.

Figure 1.7. Nacelle cup anemometer [44].

For short-term measurements, e.g. atmospheric turbulence, acoustic anemometers are the most widespread precision devices in wind energy. As far as the mechanical anemometers concerns, we can distinguish between two main types of rotating anemometers: a cup anemometer, which has three or four-cup wheels, and a propeller anemometer with propeller blades, attached to a rotating axis. While the cup anemometer has a vertical axis, consequently being independent of wind direction, a propeller anemometer has a horizontal axis which has to be oriented in the wind direction. This is generally done by a vane. Rotating anemometers, especially three-cup anemometers, are widely used as a routine instrument for wind speed measurement, offering simplicity in installation and reliability in operation. It is in common use at weather stations and around wind turbines. Without going into the details of the measurement principle of mechanical anemometers, the wind speed measurement provided by the device is based on the proportionality of wind speed to the revolution speed of the cup or propeller rotor. For both the devices one of the main limitations is related to the delayed response behavior to fast wind fluctuation changes because of the inertia of the system. Due to the limited time resolution, rotating anemometers are mainly used for mean wind velocity measurement. A common interval would be 10 minutes, where rotating anemometers are perfectly suitable, given a proper calibration. Sonic anemometers (**Figure 1.8**) instead, use ultrasonic sound waves to measure wind speed by the evaluation of the runtime between two transducers. While ultrasonic waves propagate at a speed of about 330 ms^{-1} in wind-free condition, sonic speed changes slightly in wind. Wind traveling in the same direction than sound increases sound velocity, thus reducing runtime while the opposite is true for contrary wind. The main disadvantage is the influence of the

Figure 1.8. Sonic anemometer [44].

transducer supporting structure on the wind flow. This causes aerodynamic turbulence, so the device requires thorough calibration. Another disadvantage is weather sensitivity. Sonic anemometer measurement achieves lower accuracy in precipitation when rain drops impair the speed of sound. This measurement principle offers a very fine temporal resolution (20 Hz or better), so that it is suitable for turbulence measurements. Depending on the configuration, measurements can be performed 1-, 2- or 3-dimensional. For wind turbine installations a 2D-sonic anemometer is the most common configuration. Anemometers have been for years the main reference standard equipment in the wind energy industry for a wide range of applications spanning from site assessment to power performance verification (power curve estimation) and wind turbine control. Cup anemometers are commonly installed at vertical locations on met mast reaching hub height following the prescriptions of international standards (ie. IEC Standards [25], [42]) both at onshore and offshore locations.

Care should be taken to avoid mast shadow effects, either by measuring on two sides of the mast or by using a slim open mast structure that is not cluttered by obstacles close to the anemometers.

However as turbines grow in height, higher meteorology masts are required and the instrumentation becomes more and more cumbersome and expensive correspondingly. Costs for installation of tall instrumented met towers increase approximately with mast height to the third power, and licensing permits can be time-consuming to obtain as well.

Therefore wind speed anemometric instrumentation becomes progressively more expensive to install, especially in mountainous and complex terrain, but also for offshore applications, where the machines usually reach a bigger size than onshore. Moreover, as mentioned earlier, anemometers can provide only punctual measurements of the wind. As turbines rotor planes reach the size of 120 m in diameter or more it is evident that the incoming wind field over the entire rotor planes cannot be completely described by few localized measures of cup anemometers. Accurate measurements of the inflow of today's huge wind turbines would require multi-point, multi-height wind measurements to characterize the wind speed and wind shear over the entire rotor plane. Also for control applications, the yaw signal is normally calculated from a nacelle mounted wind vane or sonic anemometer. These sensors are heavily disturbed for an operating turbine and are also measuring at a single point [64]. Other technologies have been introduced lately, among them those belonging to the category of Remote Sensing devices to measure the wind. These devices are equipped with an emitter and a receiver antenna. Their measurement principle is based on the use of light or radar emitted and backscattered signals to perform estimations of the wind speed (**Figure 1.9**).

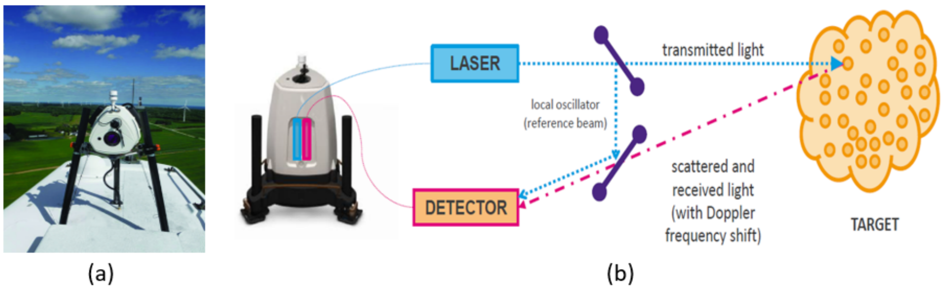

Figure 1.9. : (a) Nacelle LiDAR, (b) Wind speed measurement by LiDAR[84].

Among these LiDARs instruments are used for similar applications as anemometers [64]. A wind LiDAR is a wind measurement device that works by transmitting electromagnetic radiation (light) from a laser with a well-defined wavelength in the near-infrared band (around 1.5 μm), and by detecting the Doppler shifts in the backscattered light. These small frequency shifts (Doppler shift) result from the backscattering of light from the many small aerosols suspended and moving with the air aloft and are proportional to the wind speed in the beam direction of the wind LiDAR's adjustable measurement volumes.

Wind LiDARs available in the market for vertical mean and turbulence profile measurements are based on two different measurement principles: continous waves (CW) and pulsed LiDARs (**Figure 1.10**) [64]. The CW LiDAR focuses a continuous

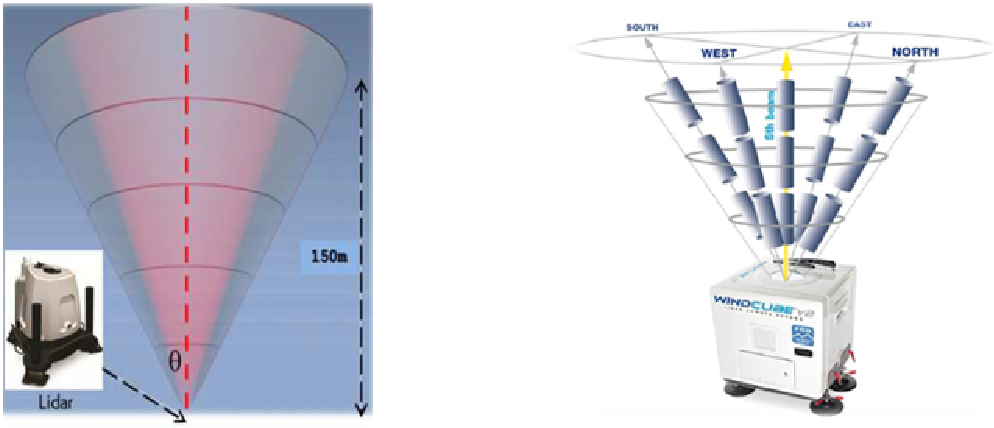

(a) continuous wave LiDAR (b) pulsed wave LiDAR

Figure 1.10. : (a) CW LiDAR, (b) Pulsed LiDAR

transmitted laser beam at a preset measurement height and determines, also continuously, the Doppler shift in the detected backscatter from that particular height. When wind measurements from more than a single height are required, the CW LiDAR adjusts its telescope to focus on the next height. A pulsed LiDAR, on the other hand, sends a sequence of many short pulses, and then it detects the Doppler shift in the backscattered light from each emitted light as they propagate with the speed of light. While a CW LiDAR measures from one height at a time, a pulsed LiDAR measures wind speeds from several range-gated distances simultaneously. A wind profiler is a ground-based wind LiDAR transmitting a continuous beam or a sequence of pulsed radiation in three or more different inclined directions. It determines the radial wind speeds in multiple directions above its position on the ground, or sea level for floating applications, providing 10-min averaged quantities of the vertical wind speed profile, the vertical direction profile, and the vertical turbulence profiles. The three-dimensional wind vector can be reconstructed by combining a series of radial measured wind speed components from several (at least three) different beam directions pointing at the same point. Wind LiDARs available on the market today offer the wind energy industry a wide range of applications, which can be summarized as follows [64]:

- Measurement of wind speed, wind direction, and turbulence profiles.
- Wind resource assessment campaigns, both onshore and offshore.
- Wind turbine performance testing, including power curve verification.

- Horizontal scanning for wind resource mapping over complex terrain.
- Nacelle Wind LiDARs are also used for turbine yaw control and individual pitch control. Since nacelle LiDARs offer better turbine-referenced accuracy across the rotor plane compared to ground-based profilers, they are usually preferred for offshore power-curve and validation campaigns to reduce uncertainty in turbine-level inflow characterization.

Compared to met masts, LiDARs, can provide a scan of the wind at different points in terms of heights and distances, overcoming the problems related to shadow effects. They represent therefore a mobile alternative to the installation of tall meteorological masts for many wind resource estimation assessment studies, on and offshore for ground-based wind turbine performance measurements. However, they present some complications: as it was mentioned, a single CW and pulsed LiDAR unit measures only line-of-sight (LOS) wind components in the direction of the transmitted signal, combining the measured radial wind speeds into a single wind vector. This wind field reconstruction inevitably provides an incomplete picture of the 3D vector flow when the wind over the probed "air" volume doesn't have a homogeneous distribution. While in conditions such as homogeneous terrain or offshore, this is a valid approximation and conventional signal processing produces very good results when compared to anemometers mounted on a meteorological mast, it leads to a wrong representation of the horizontal flow field in complex terrain where the flow undergoes stable and unstable non-uniformities. The true 3D velocity vector at a given point might actually only be measured by the provision of three (or more) profiling LiDAR units appropriately positioned, contemporary focused on the same location, increasing dramatically the cost of the measurements, or correcting the measurements with high-fidelity CFD simulations or linear models. Furthermore, the quality of the measurements is inherently dependent on the intensity of the received backscattered signal, which is significantly influenced by atmospheric conditions. In clear air, the lack of aerosols results in weak backscatter, while in foggy conditions, high atmospheric absorption of the emitted light similarly reduces signal strength. SAR (Syntetic Aperture Radar) and Scatterometers are other sensors belonging to the category of remote sensing, characterized by an emitter and a receiver antenna, but operating in the microwave range [64]. This technology is unique in its capability of capturing images at nominal fine spatial resolution (ie. 5-10 m for SAR) being less affected by weather conditions then optical sensors. They can provide wind speed measurements only for offshore applications: the intensity of the backscattered signal, detected by the satellite sensors receiver, depends on the roughness of the sea surface induced by the wind stress according to the Bragg reflection law. Empirical Geophysical Model Functions (GMFs), usually calibrated against in situ measurements, ie. anemometric buoies [75], are commonly used to correlate the Radar Backscatter to wind velocities acquisition at 10 a.m.s.l. (above mean sea level). The resulting SAR and Scatterometric surface winds are obtained by inverting the GMFs.

Therefore, compared to LiDARs or other remote sensing devices like SODARS, which will not be described in the paragraph, SAR and Scatterometers images represent indirect measurements of wind speed. Unlike the other sensors described

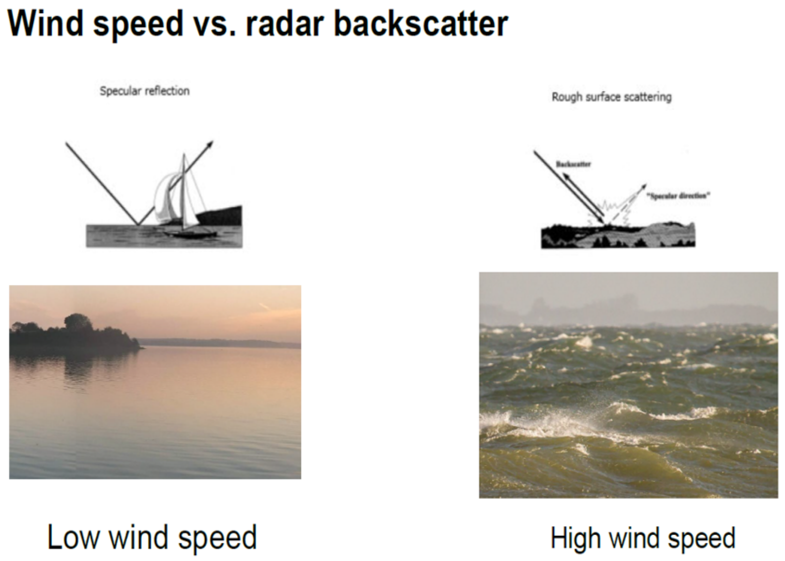

Figure 1.11. Backscattering principle

so far, they can provide with a single acquisition a snapshot of the wind fields over areas up to hundreds of kilometers, allowing the analysis of atmospheric phenomena occurring at the mesoscale lengths over the sea. Radar sensors are commonly installed on polar-orbit satellites for Earth Observation purposes or aircraft with side-looking geometry. SAR and Scatterometers have their strength and limitations.

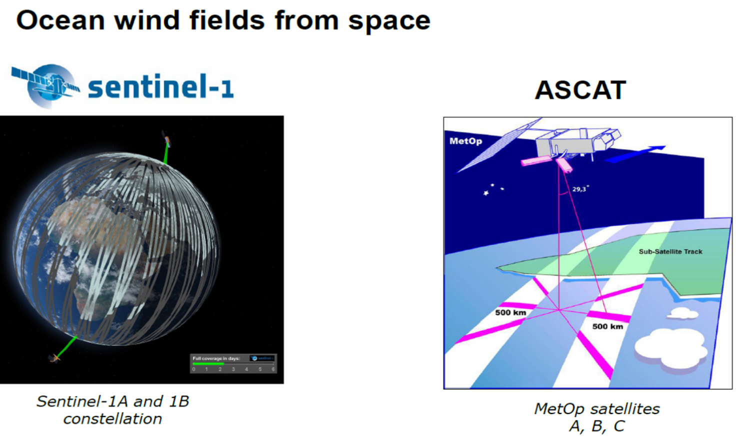

Figure 1.12. SAR and Scatterometers [64].

The SAR radar is able to provide images at higher spatial resolution compared to Scatterometers but at a lower sampling rate. On the other hand, Scatterometers are able to provide several sampling per days but at lower spatial resolution and lack of information in coastal areas because of calibration issues. The acquisition is done on multiple angles therefore wind speed and direction are both retrieved. Syntetic aperture radars instead use a single viewing angle to acquire the image, lacking the information about the wind direction: for real time processing a-priori knowledge of wind direction is required to retrieve the wind speed. The main limitations of these technologies are therefore related to the low temporal sampling rate due to consecutive satellite overpasses on the same area (in the order of days for SAR) and the need to extrapolate the measures to hub height. Furthermore,the acquisition from satellites sensors is affected by different sources of uncertainties.

In fact the spatial resolution would be normally high (10-5 m for SAR) but images need to be spatially average to bigger pixel sizes, around 500 m-100 m per pixel for SAR, on the order of km for scatterometers, applying a moving average window across the image , in order to reduce the effect of speckle noise, a randomic electromagnetic disturbace in satellite data resulting from the backscattering of the signal,and long therm period waves. This block-average process is referred to as multi-looking. A wide range of phenomena influences also the sea surface and hence the radar backscatter intensity (ie. tidal, bathimetry, reflections of hard targets such as the wind turbine itself), which are described more in detail in [64].As already mentioned, since the measurements from satellites are at 10 m a.s.l. the inferred wind speeds need to be extrapolated to hub heights, which are elevations of more interest for wind energy applications. The extrapolation of satellite data is a complex problem, usually requiring the use of sophisticated procedures to have enough accurate results and represents one of the main topics in the research field related to satellite winds. In this work of thesis a methodology based on using operative wind turbine data to improve extrapolated SAR satellite wind speeds will be introduced and explained in **Section 3.2**. Satellite images cover different applications for wind energy, includying site assesment activities and the observation of wind farm cluster wakes Since only SAR images were used for this thesis, a more detailed description with examples and best practices for the use of satellite images only derived from SAR,will be provided in **Section 3.1** and **Appendix B** underlining the specific advantages and limitations of this technology. The most widespread technologies both for site assessment and control applications are based on anemometric devices. However, as already explained, anemometers are only able to give a punctual measurement of the inflow, which is not representative of the wind field distribution over the rotor, especially given the growing size of the machines. Wind LiDARs provide a compact valuable alternative to conventional anemometers and despite their current limitation, the technology is constantly improving. However at the moment, their installation and deployment come along with significant economic costs. Following another approach, different studies have investigated the possibility of reconstructing from SCADA operative data the distribution of the wind inflow over the rotor. In the frame of this methodology, the rotor of the wind turbines is converted into an anemometer providing a measure of the wind field as it is sensed from the turbine itself [24]. The underlying idea behind wind sensing techniques is that any change in the wind conditions at the inflow will be reflected in the corresponding response of the rotor. In other words, there is in general a well-defined relation between some wind parameters and some specific features of the rotor response. Measuring such behavior (for example in terms of blade loads or accelerations, torque, rotor speed, blade pitch, etc.) is therefore possible, under certain hypotheses and conditions, to estimate these wind characteristics. This approach would bring about a significant reduction of the costs associated with the monitoring of turbines since they are based solely on data from sensors normally installed on the machines (e.g., strain gauges, rpm, torque, power signal, etc.). The following pages will give an outline of these wind sensing techniques and the use of operative data to reconstruct the inflow distribution.The first basic example of a wind sensing technique is represented by the dynamic torque balance-estimation equations. Thereby, turbine power or torque measurements are used to estimate an "average" rotor-effective wind speed (REWS), representative of the flow distribution over the entire rotor, by the power curve or power coefficients, assuming that the operational parameters (rotor speed, pitch setting, electrical torque) of the machine are measured at each instant in time. A review of the different formulations of the technique to compute the REWS is provided in [70]. However, as argued in [20], [68], several wind states can be reliably observed using blade loads, including wind speed, vertical and horizontal shears, lateral misalignment, and upflow. More sophisticated models, referred to as wind observers, which allow to estimate different information about the characteristics of the inflow blowing over the rotor from blade load measurements have been introduced by [24], [20]. The “sector-effective” wind estimator returns an estimated value of the wind flow velocity over four rotor sectors, called sector-effective wind speeds (SEWS), for the operating settings of the turbine in terms of pitch, rotor speed, azimuthal position of the blades, and measurements of the blade loads **(Figure 1.13)**. The method is based on the estimation of the wind speed at the rotor using measurements of the out-of-plane blade bending moment, as described in more detail in [24], [68]. In this context, a cone coefficient is defined to relate the measured out-of-plane bending moment at the blade root to an effective wind speed sensed by the blade, referred to as the Blade Effective Wind Speed (BEWS). Under the assumptions of uniform wind inflow and a quasi-steady structural response, gravitational effects on the blade are neglected, and the measured load approximates the aerodynamic moment.

The cone coefficient for the i-th blade is then expressed as:

$$C_m(\beta, \lambda, q, \psi_i) = \frac{m_i}{0.5\,\rho ARV^2} \tag{1.2}$$

where m_i is the out-of-plane root bending moment, ρ is the air density, A is the rotor swept area, R is the rotor radius, q is the dynamic pressure acting on the blade, V is the effective wind speed, and $\lambda = \frac{\Omega R}{V}$ is the tip-speed ratio. This formulation enables the use of blade load measurements to estimate local inflow conditions at the rotor disk. The derivation of the coefficient C_m from the application of the Coleman transformation [21] to the blade bending moments is explained in [24]. Values of C_m for a reference air density ρ_{ref} were computed from aeroelastic models of turbines implemented in OpenFAST [46], [68].

Once the cone coefficient has been determined, lookup tables (LUTs) were generated, as explained in [68]. These LUTs return an estimate of the BEWS at the azimuthal position of the blade ψ_i, for the operational settings of the turbine in terms of pitch ϕ, measured loads m_i, and rotor speed Ω, by inverting **Equation 1.2**:

$$BEWS = LUT_{C_m}\left(\beta, \Omega, \psi_i, m_i, \frac{\rho}{\rho_{ref}}\right) \tag{1.3}$$

Compared to the torque balance equation, the observer can provide a local estimate of the wind inflow as it is sensed by the blade, turning it into a sensor scanning the local variability of the wind with it's motion. Dividing the rotor area into four 90° sectors, the average wind speed over each sector is computed by time-averaging the instantaneous BEWS. The resulting values correspond to the aforementioned SEWSs [69], from which the name "sector observer" originates.

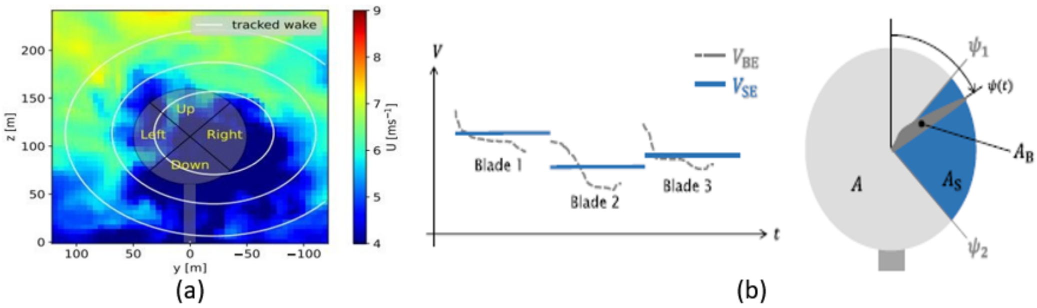

Figure 1.13. (a) Partitioning of the rotor into the four quadrants of the Sector Observer [33] (b) Definition of the BEWS and the SEWS [24]

From the computed SEWS values, the lateral and vertical shear components of the rotor wind field can be derived [68]. This enables the reconstruction of the main inflow characteristics using exclusively load-based measurements, thereby offering valuable insight into the wind conditions acting on the turbine.

The model was tested both against high-fidelity CFD simulations [24] and in the field [68], providing good agreement in terms of vertical wind shear estimated from out-of-plane bending moments with met mast reference measurements. The sector observer was also successfully employed as a wake detector: the trends of the SEWSs provide information regarding which side of the rotor has been impinged by the wake [69], [33]: for example, a decrease in the left SEWS compared to the right one is correlated with the positioning of the wake centerline over the left side of the turbine at a given instant. This wind sensing method presents therefore a valid straightforward alternative to other sensors for measuring the wind speed distribution over the rotor. It could potentially be employed for multiple applications ranging from wind turbine monitoring and control to forecasting given its ability to estimate the wind shear distribution, which is correlated to the stability of the atmosphere, and to have information about the position of the wake over the rotor of an impinged turbine. Compared to the other sensors, such as LiDARs, the method can provide measurements of the inflow as directly perceived locally by the rotor and not scanning the inflow in front of it. The observer model doesn't require external additional hardware but it relies on sensors normally installed on the nacelle and can be implemented onboard the machines at a negligible computational cost. Another wind sensing technique, described in [20], correlates the harmonic components of the root bending moments acting on the blade to the parameters of the wind inflow in terms of vertical and horizontal shear, and yaw and vertical upflow misalignment of the wind. Different reformulations of the "harmonic observer" model were proposed [50] and tested both in the field [19] and simulation environment [50], providing estimates with accuracies compatible with typical use cases in wind turbines and wind farm control and very similar results to the measurements obtained with the widely adopted profiling LiDAR, while avoiding its complexity and associated costs. .Hence, wind sensing technologies use the response of the rotor – in the form of loads, accelerations, and other operational data – to infer the characteristics of the wind blowing on the turbine. The technique can be regarded as a model inversion process, where the system response is used to estimate the disturbance, in this case represented by the wind. On a wind farm scale another example of wind field observation based on the use of the information contained in the operative SCADA data was presented in [28]. In this work, the wind farm as a sensor approach was introduced to improve the predictions of a wake engineering parametric wake model.This methodology uses operational SCADA data to simultaneously "tune" the parameters of the wake model and "learn" the parameters that define "a correction field" ("STL" methodology), resulting in a better ability to describe the heterogeneities in the flow field induced by the orography of the site (e.g., in the form of coastal gradients) and plant-internal effects related to the propagation of the wake inside the wind farm. The study shows how wind turbine operative data can be used to provide a better description of the flow distribution developing around and inside a wind plant. The whole plant effectively becomes a distributed sensor that "feels" the flow that develops within its boundaries; this has suggested to name "farm as a sensor" this approach, in an analogous way as the turbine as a sensor methodology converts the single machine into an anemometer. To summarize, this chapter provides an overview of the various methods and devices commonly used in the wind energy industry to measure wind fields. It also presents the current state-of-the-art in wind sensing techniques that utilize available operational data from turbines to reconstruct wind field distributions at both the turbine and wind plant scales. As previously mentioned, these methodologies—based on data-driven approaches—offer potentially cost-effective alternatives or complementary insights to conventional measurement devices. Their applications span several sectors, including Monitoring, Operations & Maintenance (O&M), wind forecasting, and plant control. This work of thesis explores the application of SCADA data to enhance the reconstruction of wind field interactions with wind farms, both at the scale of individual turbines and at the broader wind farm-mesoscale level. At the turbine scale, **Chapter 2** reports a study in which wind speed measurements from the described sector observer [24] are incorporated into an Ensemble Kalman Filter (EnK) [36] to correct predictions made by the low-fidelity wake model FLORIDyn (FLOW Redirection and Dynamics) [38]. This closed-loop formulation, which augments the wake model with observer-derived estimates, was tested on a simple two-turbine layout and compared to the results of a LES simulation. Preliminary analysis suggested that the closed-loop approach significantly improves predictions of wind flow characteristics and the wake centerline position compared to FLORIDyn's open-loop configuration, particularly under full wake conditions using SEWSs measurements [33]. At the wind farm scale, a data fusion approach is introduced in textbfChapter 2 using both operational turbine data and satellite imagery. The study focuses on the extrapolation of Synthetic Aperture Radar (SAR) wind speed data, proposing a novel method to recalibrate hub-height wind speed fields derived from SAR imagery using SCADA data from an offshore wind farm. This effectively transforms the wind farm into a large-scale in situ anemometer. The goal of this approach is to introduce a viable alternative to conventional methods, which typically rely on external devices such as wind-profiling

LiDARs, to bring SAR-derived wind speeds to hub height [55]. Preliminary results indicate that even a simple best-fitting procedure applied to residuals between co-located SAR and SCADA wind speeds can enhance the quality of the extrapolated wind field, without the need for complex algorithms or extensive datasets.

Chapter 2

Wind field observation at Wind Turbine scale

This section of the thesis examines the interaction between wind flow and turbines at the wind-turbine scale.

A closed-loop formulation of the FLORIDyn model, augmented with SEWS predictions from the data-driven wake observer introduced by [24], is presented. The results of this novel approach, discussed in **Section 2.2.1**, show that the augmented model—corrected using the observer's predictions—offers a more accurate representation of inflow propagation compared to the baseline open-loop configuration.

This study demonstrates how operational data from wind turbines can be effectively exploited to enhance the reconstruction of the flow field at both turbine and intra-turbine scales.

2.1 The FLORIDyn framework

In the context of this thesis, which investigates the interaction between wind fields and wind farms across different spatial and temporal scales, SCADA data represent a key resource for multiple applications, including monitoring and control optimization. In particular, the use of operational data has been explored to enhance the understanding and prediction of intra-turbine interactions.

The characteristic "fingerprint" of the wind field acting on a turbine rotor is embedded in the trends and patterns of SCADA signals. These signatures can be leveraged for various purposes, including the monitoring of inflow conditions and the optimization of the plant's energy yield.

In recent years, the topic of wind farm control has raised growing interest as renewable energies become more and more relevant for the current and future energy mix. Maximizing the power generated by a wind farm is not a trivial task as the turbine-to-turbine interaction is characterized by complex flow, large delay times, and an ever-changing environment. Wind-farm-layout optimization requires the prediction of wake flows for many (on the order of thousands or more, depending on the optimization technique) scenarios including, but not limited to, multiple layouts and variations in wind direction, wind speed, and thermal stratification. Such optimization can only be achieved using simple and computationally inexpensive wake models, referred to as parametric wake models. A detailed description about the current state of art of this models can be found in **Appendix A.1**.

FLORIDyn belongs to this category of models. The dynamics of the wake are captured via the propagation of *Observation Points* (OPs), which represent air masses moving downstream in a Lagrangian framework. These OPs originate at the turbine rotor planes **Figure 2.1** and carry in their motion, key operating information such as the yaw misalignment , the axial induction factor or the hub-height freestream velocity (**Figure A.4**). These quantities are relevant for the description of the flow dynamics since they determine wake characteristics in terms of shape, velocity deficit, and deflection. Therefore, changes in these variables "travel" downstream with the OPs at discrete time steps, providing a simplified yet dynamic representation of wake behavior **Figure 2.1**.

Alternative formulations of the FLORIDyn model are available in the literature. A brief description of the main ones can be found in **Appendix A.1**. In the version of FLORIDyn used for this thesis, wake and ambient flow quantities are described by two separate sets of OPs [26]. This separation allows for modeling the different advection velocities of the two flow regimes and their interaction: wake OPs propagate more slowly than ambient OPs, as the wake travels at a reduced wind speed. In addition, changes in the background flow influence the downstream evolution of the wake (**Figure 2.1**).

The dynamics are restricted to the horizontal plane at hub height, and vertical meandering motions are not included in the model description. The spatial positions of the ambient and wake OPs are defined in a two-dimensional Cartesian coordinate system:

$$\mathbf{x}_w^k = \begin{bmatrix} \boldsymbol{x}_{w,1}^k \\ \boldsymbol{x}_{w,2}^k \\ \vdots \\ \boldsymbol{x}_{w,N_w}^k \end{bmatrix}, \quad \mathbf{x}_a^k = \begin{bmatrix} \boldsymbol{x}_{a,1}^k \\ \boldsymbol{x}_{a,2}^k \\ \vdots \\ \boldsymbol{x}_{a,N_a}^k \end{bmatrix} \tag{2.1}$$

where N_w and N_a denote the number of wake and ambient OPs, respectively, and k refers to a generic time instant. The position of the generic wake OP $\mathbf{i_{t,h}}$ is expressed in the vector form as $\boldsymbol{x}_{w,i} = [x_{w,i}, y_{w,i}]$ and the location of the generic ambient OP is defined in an analgous way.

Figure 2.1 illustrates the dynamics of the flow according to the framework proposed in [26], depicting the steps taken to update the positions of ambient and wake OPs from a generic instant k to $k+1$. Ambient OPs represent undisturbed inflow conditions and carry the state variables wind speed $U_{a,i}$, wind direction Γ_i, and turbulence intensity $I_{a,i}$. These quantities are grouped into the following vectors, defined as **Equation 2.1**:

$$\mathbf{U}_a^k,\ \boldsymbol{\Gamma}^k,\ \mathbf{I}_a^k \in \mathbb{R}^{N_a \times 1} \tag{2.2}$$

On the other hand, wake OPs model the dynamic of the wake centerline and an engineering wake model is used to characterize the cross-wind profile of the flow. With their, motion, they carry the control inputs of the wind turbine at the time of their creation, specifically yaw misalignment γ_i and induction factor a_i:

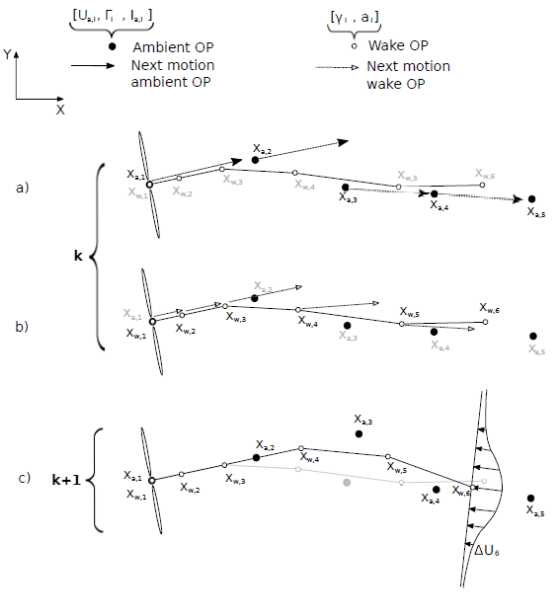

Figure 2.1. Steps of the position update of ambient and wake OPs according to the model proposed in [26]. A change in the direction (Γ_2 at $x^k_{a,2}$) of the ambient points (panel (a)) at state k affects the direction of the wake points (panel (b)), resulting in a modified wake trajectory in state $k+1$ (panel (c)).

$$\boldsymbol{\gamma}^k,\ \mathbf{a}^k \in \mathbb{R}^{N_w \times 1} \tag{2.3}$$

Each wake OP is associated with a velocity deficit ΔU_k, whose profile and magnitude can be computed with a suitable engineering model. For this implementation of FLORIDyn, the Gaussian wake model of [12] has been adopted, as it is shown in **Figure 2.1**. To compute the velocity deficit, the ambient conditions are firstly mapped with linear interpolation at the location of the generic i-th wake OP. The resulting delayed ambient conditions and control inputs, associated with i_{th} wake OP's position, are used to compute the reduction in velocity:

$$\Delta U_i^k(r) = f_w\left(r \mid \mathbf{x}_{w,i}, \mathbf{U}_{w,i}, \mathbf{I}_{w,i}, \gamma_i, a_i\right)^k \tag{2.4}$$

where r represents the radial distance from the wake center, $\mathbf{U_{w,i}}, \mathbf{I_{w,i}}$ the interpolated background wind speed and turbulence intensities at the $\mathbf{x_{w,i}}$ position of the $\mathbf{i_{t,h}}$ wake OP at time step k.

Additionally, the wake-induced turbulence intensity $I_{\text{add},i}$ is evaluated using a model adapted from [32].

Ambient OPs are advected with the background wind speed, while wake OPs propagate with a lower velocity due to the velocity deficit. The wake advection velocity is computed as:

$$u^k_{w,i} = U^k_{w,i} - \frac{1}{A_w}\int_{A_w} \Delta U_i^k(r)\, dA \tag{2.5}$$

where A_w is defined as the wake cross-sectional area where 99% of the ambient wind speed is recovered.

The OP positions are updated at each time step using:

$$\mathbf{x}_w^{k+1} = A\mathbf{x}_w^k + B\mathbf{x}_{w,1} + A\mathbf{u}_w^k \Delta t \tag{2.6}$$
$$\mathbf{x}_a^{k+1} = A\mathbf{x}_a^k + B\mathbf{x}_{a,1} + A\mathbf{U}_a^k \Delta t \tag{2.7}$$

The state matrices A and B are defined as in the original FLORIDyn formulation, reported in **Equation A.18** from the **Appendix A.1**. The ambient flow variables and control inputs evolve similarly:

$$F_a^{k+1} = AF_a^k + BF_{a,1}^k \tag{2.8}$$

where F_a is a generic environmental quantity. New ambient conditions and control settings enter the simulation domain at the upstream rotor. If this rotor is exposed to freestream flow, these conditions can be directly obtained from SCADA data or wind speed measurements [38], [26], providing the input source to the model (**Appendix A.1**) . A downstream turbine is considered to be affected by a wake when an external wake OP is located near its rotor. In this case, ambient flow values are at first, transferred from nearby wake OPs using inverse distance weighting at the waked rotor:

$$F_{a,\text{ext}} \rightarrow F_{a,1} \tag{2.9}$$

The velocity deficit is then interpolated onto the rotor plane:

$$\Delta U_{\text{ext}} \rightarrow \Delta U_1 \tag{2.10}$$

The resulting inflow velocity is obtained by subtracting the average velocity deficit ΔU_1 from the ambient wind speed $U_{a,1}$ mapped at the waked rotor:

$$U_{\text{in}} = U_{a,1} - \Delta U_1 \tag{2.11}$$

This formulation provides a physically consistent framework for dynamically resolving the wake's influence on downstream turbines using a reduced state representation suitable for real-time estimation and control.

2.2 Methodology: closed loop coupling of a dynamic wake mode with a wake detector

This section describes an application of operational SCADA data from wind turbines to infer the distribution of the wind field as perceived at the rotor. This information can be leveraged to improve the accuracy of engineering wake models, which, in their open-loop form, often fail to capture the flow dynamics with sufficient precision for wind turbine and wind farm control purposes. To overcome this limitation, a method commonly used in control applications has been adopted: the implementation of a Kalman filter [36]. This mathematical algorithm uses measurement data to correct the estimates provided by a model, taking into account the influence of random noise, and model inaccuracies. Specifically, the Kalman filter adjusts the predictions of the model using the so-called Kalman gain, which quantifies the relative confidence in the measurements compared to the model predictions. This gain is computed from the statistical properties in terms of variances and covariances of both the model and the measurement noise and determines how strongly the measurements should influence the correction of the predicted state.At each iteration, the model's prediction is initialized from the previously corrected state. This allows the estimation process to evolve over time, producing updated state estimates that progressively converge toward the actual system behavior. In this closed-loop formulation [38], [18], [27], the wind turbines themselves act as distributed flow sensors. Real-time measurements—such as generated power, wind direction at the nacelle vane, or rotor-averaged wind speed measured by onboard sensors—can be used to dynamically correct model predictions of the evolving wind field. These measurements are obtained solely from standard sensors already installed on modern turbines. The wind field, characterized by variability across multiple spatial and temporal scales, influences the dynamic response of the turbine (e.g., power output trends). This influence is encoded in the time series of SCADA signals, providing valuable information that can be extracted to estimate the current wind state. Different estimation methods, discussed in **Appendix A.1.1**, have been introduced in the literature, many of which employ the EnKF [36], a variant of the standard Kalman filter algorithm. The EnKF estimates the state of the system by simulating many different versions of the model with varying starting states. Each realization of the model is characterized by its own state and forms one member of the ensemble, which evolves slightly differently over time from the others. In this case, the wind speed states of different components of the ensembles diverge and so do the locations of the OPs [18]. Additionally, it is assumed, as with all Kalman Filter formulations, that both the states and the measurements are corrupted with a Gaussian white noise disturbance. This randomly generated noise, along with the different starting states, ensures that the states of the various components of the ensemble diverge over time. The states differ across all elements of the ensembles and diverge over time if not corrected. During the correction step, the differences between the ensemble states are used to approximate a state error covariance matrix P, which allows the calculation of the Kalman gain matrix. This approximation of the state error covariance matrix does not require the computation of derivatives, thus reducing the mathematical complexity of the EnKf compared to other Kalman filter implementations. On the other hand, the reduced mathematical effort comes at the cost of higher computational requirements in the simulations. However, as a result of the available increasing computational capacities and given the parallelizable nature of the EnKF, this trade-off has become more tolerable. The method can be used to estimate the state of complex non-linear systems as well as the uncertainty of an identified state, a property that is useful for robustly solving control problems.

An implementation of the EnKF was proposed by [27] and designed for the FLORIDyn version described in **Section 2.1**. The purpose of the work was to develop a closed-loop Wake model that is able to estimate the contribution to the wind field fluctuations related to different spatio-temporal scales affecting the power production and loadings of the wind turbines [27] Power measurements from a waked turbine were used for the implementation of the filter. The model was tested in a layout of two turbines. The downstream one was laterally staggered of $0.5D$. to generate partial wake conditions constantly impinging on one side of the downstream rotor, and compared to a high-fidelity LES simulation considered as reference ground truth. The meandering of the wakes causes power fluctuations, and the staggered layout was introduced on purpose to clearly correlate the effect of flow motion of the power fluctuations. The analysis of the filter statistics showed improved agreement in the predictions of the power output of the downstream turbine. Being this the targeted quantity of the filter used to correct the model, that was to be expected. However, using only power measurements as a quantity might lead to unrealistic corrections of the predicted states: an error in ambient flow speed predictions might be compensated by a non-physical wake displacement or viceversa.

To assess the ability of the model—corrected using only power measurements—to realistically follow flow fluctuations, a tracking algorithm [76] was used to identify the lateral displacement of the wake from CFD data. The analysis of the trends revealed that the corrected model showed improved agreement with the CFD reference, including a better ability to follow rapid fluctuations in the flow, compared to the open-loop configuration.

These results demonstrated that the EnKF can effectively improve the baseline open-loop model in capturing fast-scale dynamics which cause the meandering of the wake and the fluctuations observed in the power trends, despite relying solely on power measurements.

However, the investigated test case referred to a staggered wind turbine impinged only on one side of the rotor,where the correlation between power fluctuations and wake positions is statistically clear. In full wake conditions, it would not be possible only from the power trends, being a single scalar quantity, to correctly predict which side of the rotor is effectively impinged by the wake. As part of this work of thesis about the use of operative data to reconstruct the wind flow around and inside the wind farm and turbines, on a turbine scale level, a new implementation of the closed loop FLORIDyn model introduced by [26] has been investigated. In this new reformulation of the FLORIDyn model, wind speed measured by the sector observer described in **Section 1.3** and introduced by [24] are used to correct the prediction of the open loop framework. The new version of the model uses available wind speed measurements provided by the observer at the wake turbines to correct the estimates of flow quantities provided by the baseline model and since it is based on measurements of wind speeds over the rotor, can provide insights into the evolution of the wake even in conditions of full impingement of the downstream turbines. A description of the model implementation and the results from a case study will be provided in the following chapters.

2.2.1 Closed loop model formulation

The integration of the dynamic wake model with the flow observer is reported in **Figure 2.2** with the main elements highlighted. For a generic turbine T_z the full state vector can be written as:

$$x_k^T = \begin{bmatrix} x_w \\ y_w \\ U_\mathrm{a} \end{bmatrix}_{T_z}^{k} , \qquad (2.12)$$

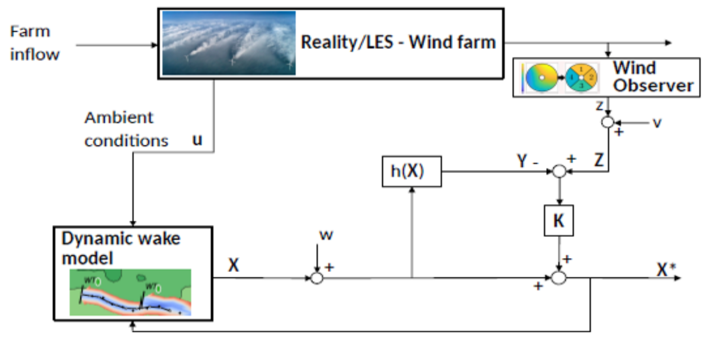

Figure 2.2. Flow chart of the dynamic model and Kalman filter correction [33].

However, the focus of the present study is on the simultaneous correction of the estimates provided by the state space model in the fluctuations of the ambient wind speed U_a, as well as lateral meandering motions of the wake position y_w. Accordingly, the state space vector used in the following Kalman filter equations is a subset of the full system state, containing only these two state variables. Therefore, for a generic turbine in the farm T_i, the equation of the state vector assumes the following form:

$$x_{T_z}^k = \begin{bmatrix} y_w \\ U_\mathrm{a} \end{bmatrix}_{T_z}^k \quad , \tag{2.13}$$

Considering a cluster of N_T turbines the single state can be rewritten as:

$$x^k = \begin{bmatrix} x_k^{T1} \\ . \\ . \\ . \\ x_k^{N_T} \end{bmatrix}^k \tag{2.14}$$

The dynamic wake model is driven by sampled flow quantities that correspond to measurements typically available from full-scale wind turbines. These include, for instance, wind direction obtained from the nacelle-mounted wind vane and the Rotor-Equivalent Wind Speed (REWS) for upstream turbines, which serves as input for the FLORIDyn model. These measurements can be obtained either from operational field data or from high-fidelity Large Eddy Simulations (LES) that replicate real-world conditions. The formulation of the ensemble X made of a number N_E of state vectors x is expressed as follows:

$$X = \begin{bmatrix} x_1 & x_2 & x_3 & \cdots & x_{N_E} \end{bmatrix} \tag{2.15}$$

, as mentioned before and explained in **Appendix A.1.1**, each member of the ensemble represent multiple evolutions of the x vector. The system covariance matrix is the sample covariance of the state vectors, $P = cov(X)$, defined as in **Equation A.70** from **Appendix A.1.1**. The whole ensemble is advanced in time as

$$X_k = f(X_{k-1}, u_k). \tag{2.16}$$

where the u contains the new flow quantities and turbine control states entering the system at the first OPs. For a simpler notation, superscript k is dropped from the following description of one Kalman filter iteration. Each ensemble member is perturbed with process noise individually. The noise is assumed to follow a normal distribution, $w = N(0, Q)$, where $Q \in \mathbb{R}^{N_S \times N_S}$ is the noise covariance matrix, and N_S is the number of system states. For this study, the rotor inflow measurements of the observer are used to correct the model estimate. As previously mentioned, this FLODIRDyn formulation describes only the lateral displacement of the wake. Therefore only the left and right sector velocities are the considered measured quantities.

The measurement for a downstream turbine T_q is consequently expressed as:

$$\mathbf{z}_{\mathbf{T_q}} = \begin{bmatrix} U_L^{\text{obs}} \\ U_R^{\text{obs}} \end{bmatrix} \tag{2.17}$$

These measurements $z \in \mathbb{R}^{N_{\text{meas}} \times 1}$ need to be additionally perturbed with measurement noise $v = N(0, R)$, where R is the measurement uncertainty matrix, to form an ensemble of observations $Z \in \mathbb{R}^{N_{\text{meas}} \times N_{\text{en}}}$. The measurement noise R and the process noise Q are used as tuning parameters, which can be found with an iterative approach . The process noise is modeled using an exponential function that accounts for the spatial correlation of turbulent flow fluctuations between two turbines, which are responsible for the wake meandering. This function describes the decrease of covariance with separation distance between two states, referred with indices i and j:

$$\sigma_{S,ij}^2 = \sigma_{S,ii}^2 \exp\left(-\frac{l_{ij}}{\Lambda}\right) \tag{2.18}$$

where $\sigma_{S,ij}^2$ models the variance of the added noise for a specific state type, e.g. ambient wind speed U_a. The symbol Λ indicates the integral length scale of the turbulent background field and l_{ij} represents the separation distance between the corresponding OPs. This implementation requires the update of Q and the calculation of distances between all observation points at every iteration. To reduce the computational cost, this is done for the average of the ensemble $\bar{X}$. To connect the model predictions with the available measurements and enable the correction of the targeted quantities, left and right effective predicted velocities are formulated as the outputs of a nonlinear function [33] of the system state matrix X **Equation 2.15**. $Y = h(X)$. Y is represented for a generic turbine as:

$$\mathbf{y}_T = \begin{bmatrix} U_L^m \\ U_R^m \end{bmatrix} \tag{2.19}$$

where the superscript m stands for "model", and for this impelentation consists of the modeled left and right sector wind speeds.

The state-to-output covariance matrix linking the system output to the system states is defined as (**Appendix A.1**):

$$P_{X,Y} = \frac{1}{N_E}\left(X - \bar{X}\right)\left(Y - \bar{Y}\right)^\top \tag{2.20}$$

the output covariance matrix is represented by:

$$P_Y = \mathrm{cov}(Y) \tag{2.21}$$

Finally, the Kalman gains are calculated according to:

$$K = P_{X,Y} \left(P_Y + R\right)^{-1} \tag{2.22}$$

which allows for updating the system state vector as:

$$X^* = X + K \left(Z - Y\right) \tag{2.23}$$

2.2.2 Case study

The new closed-loop formulation, augmented with the wake observer, was tested in a simulation layout of two aligned turbines under full wake conditions. A high-fidelity SOWFA [57] simulation served as the ground truth for the flow field evaluation.

The simulation setup consists of two IEA 3.4 MW turbines [23]. These onshore reference turbines have a hub height of 110 m and a rotor diameter D of 130 m. The turbines T_1 and T_2 are fully aligned in a streamwise direction, spaced $6D$ apart, with T_1 located $4D$ from the inlet. The inflow was characterized by an average free stream velocity of 7.7 ms^{-1}, a turbulence intensity of 12 at hub height, and a shear of 0.2. The simulation time is equal to 654 s. The same tracking algorithm of [27] was used to identify the location of the wake of the upstream turbine upon impingement, whose implementation is described in more detail in [76].For the wake meandering tracking, a cross sectional $Z - Y$ plane was placed $0.5D$ upstream of the waked turbine, as reported in **Figure 2.3a**.

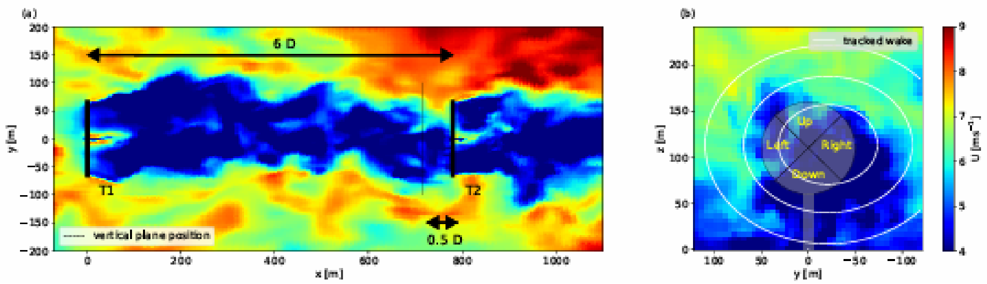

Figure 2.3. (a) Streamwise velocity at hub height after 360 s. The dashed line represents the location of the vertical plane. (b) Streamwise velocity at the vertical plane 0.5 D in front of the second turbine. The shaded area represents the outline and the four rotor sectors of the second turbine [33].

The tracking algorithm includes as free parameters firstly the wake width. Secondly, the offsets of the wake center from the origin in the lateral y-direction μ_{cy}, and from hub height in the vertical z-direction μ_{cz}. **Figure 2.3b** shows the streamwise velocity at the plane for the same time step as panel a. A statistical evaluation of the computed wake position station reveals that the wake meanders in the lateral as well as in the vertical directions. The standard deviations of the position in lateral direction $std(\mu_{cy}) = 0.35D$ is however larger than in the vertical $std(\mu_{cz}) = 0.18D$. The ground probably has a restraining effect on the wake in the vertical direction at this separation distance. The correlation of wake offset and power output of the downstream turbine is defined as $r_{c,P} = cov(\mu_c, P)/(std(\mu_c)std(P))$. In the lateral direction, a clear linkage with $r_{cy,P} = 0.63$ was found. On the other hand, in the vertical direction, there is no clear correlation as $r_{cz,P} = -0.2$. This result was probably affected by phases where the wake had large lateral offsets (higher power) but was close to hub height in the vertical direction, as well as the short simulation time. As mentioned, the measurements of the wind speed of the Sector observer provide information regarding which side of the rotor has been impinged by the wake [24], [69]: for example, a decrease in the left SEWS compared to the right one is correlated with the positioning of the wake centerline over the left side of the turbine at a given instant. Streamwise velocities were extracted from the LES simulation at the vertical $Z-Y$ plane placed $0.5D$ in front of the waked turbine T_2 reported in **Figure 2.3a**. The spatial averages of the velocities, sampled at points of the plane having the same $Z-Y$ coordinates of the four sectors at the rotor, are considered as a benchmark to evaluate the observer predictions. Overall, the plots

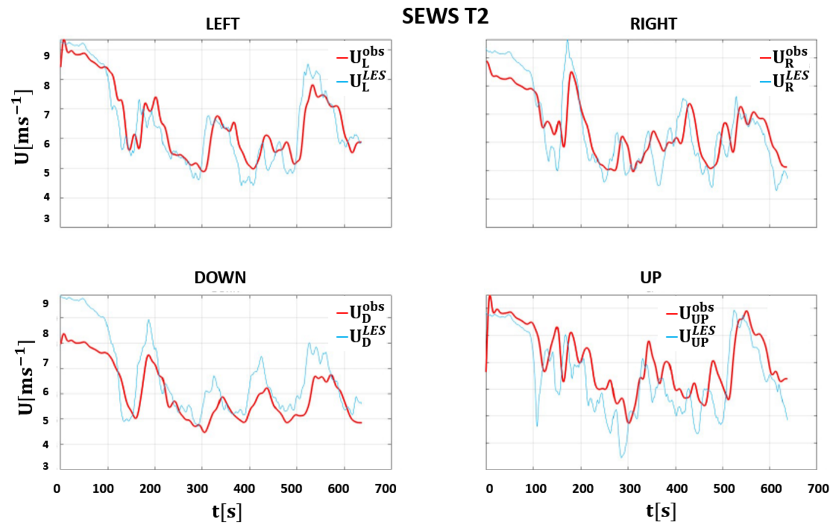

Figure 2.4. Time series of the SEWSs computed by the observer (U_L^{obs}, U_R^{obs}, $U_{\text{UP}}^{\text{obs}}$, U_D^{obs}) for the four sectors of the waked turbine T2 compared with the spatial averages of the streamwise velocity corresponding to each sector (U_L^{LES}, U_R^{LES}, $U_{\text{UP}}^{\text{LES}}$, U_D^{LES}), extracted from a vertical plane located at an upstream distance of $0.5D$ from the rotor plane in the LES simulation [33].

from **Figure 2.4**, show a good agreement between the predicted SEWS and the averaged velocities extracted from the CFD simulation. The discrepancies between the two trends are probably due to the different definitions of the wind speeds. As mentioned, the observer outputs refer to the resulting time average of the BEWS "sensed" by the blades over each sector. On the other hand, the reference velocities represent the spatial means of the streamwise wind speed computed at each time step of the simulation. A time delay of approximately 10 seconds between the two trends is also visible from **Figure 2.4**, which is directly related to the propagation of the flow from the upstream plan

2.3 Results

The predictions from the model in the conventional open loop configuration were compared to the closed loop version with an activated EnKF. The dynamic wake model was run with a timestep $\Delta t = 5s$. $N_w = N_{amb} = 30$ wake and ambient observation points resolve the wake and ambient flow. The input feed of environmental conditions to the dynamic model is sampled from the CFD simulation at the upstream turbine to resemble measurements, that would be available at a full-scale turbine. The ambient wind speed U_a is obtained through the power production of the upstream turbine, the wind direction Γ from a single point $0.5D$ upstream of the turbine. The upstream location was chosen over the possibility of sampling the flow at the top of the nacelle, at the normal installation point of a wind vane. This approach would have necessitated corrections for flow distortions induced by the rotating machine and its wake. Additionally, a precise solution of the flow field around the nacelle would have required a finer meshing of the area, increasing the computational cost. After 100 s of simulation time, the Kalman filter was activated with an ensemble size of $N_{en} = 100$. The elements of the Q and R matrix were tuned offline for a better performance of the filter to $\sigma_{U_a} = 0.2ms^{-1}$, $\sigma_y = 4.3m$ and $\sigma_{U,L} = \sigma_{U,R} = 0.5ms^{-1}$, respectively. The two panels of **Figure 2.5** show the modeled and observer-measured left and right sector wind speed. The closed loop

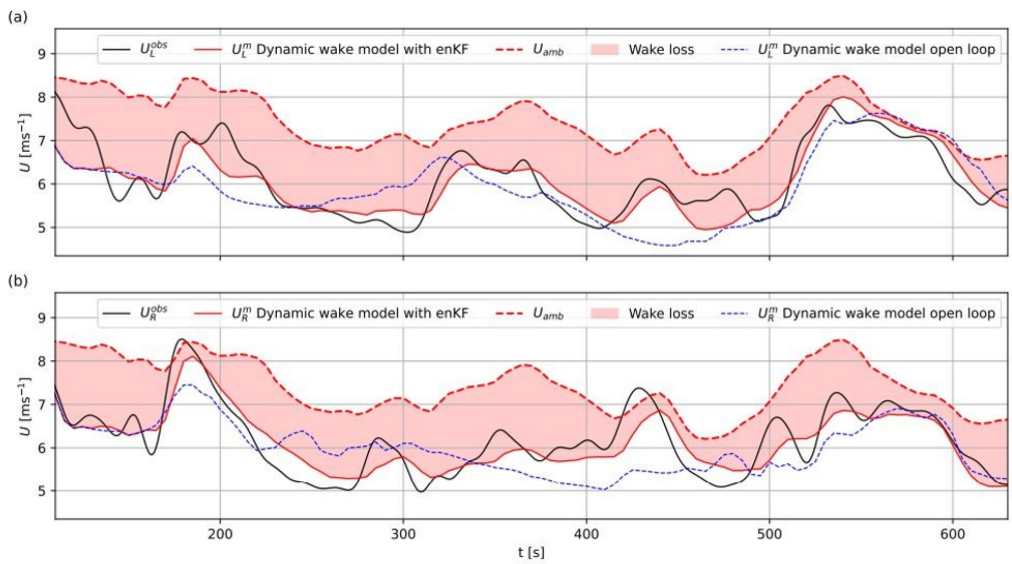

Figure 2.5. Inflow velocity at the left (a) and right (b) sector of the downstream wind turbine.

model shows a much better agreement on the fast fluctuations, as the sector wind speeds were the target quantities of the filter. The remaining discrepancies can, on one hand, be accounted for by the natural lag time of the filter. Corrections are constantly advected downstream through **Equation A.18** and **Equation 2.8** and leave the system, while new uncorrected states approach the turbine. Secondly, the real wake shape is at times torn apart, so it does not resemble the wake model Gaussian shape. Therefore, the filter cannot always match both sector wind speeds simultaneously. The plot additionally shows the modeled background wind speed as well as the modeled wake loss, defined as the difference between the ambient wind speed at the downstream turbine (**Equation 2.2**) and the SEWSs predicted (**Equation 2.19**) by the FLORDIyn model, for the closed loop system. At $t = 550s$, the wake loss reduces to a very small value on the left side of the rotor. This is because the model predicts a large wake offset to the right side (in negative y-direction) and therefore the left side experiences an almost clean (unwaked) inflow. As mentioned before, the wake position is used to verify if the applied corrections are physical.

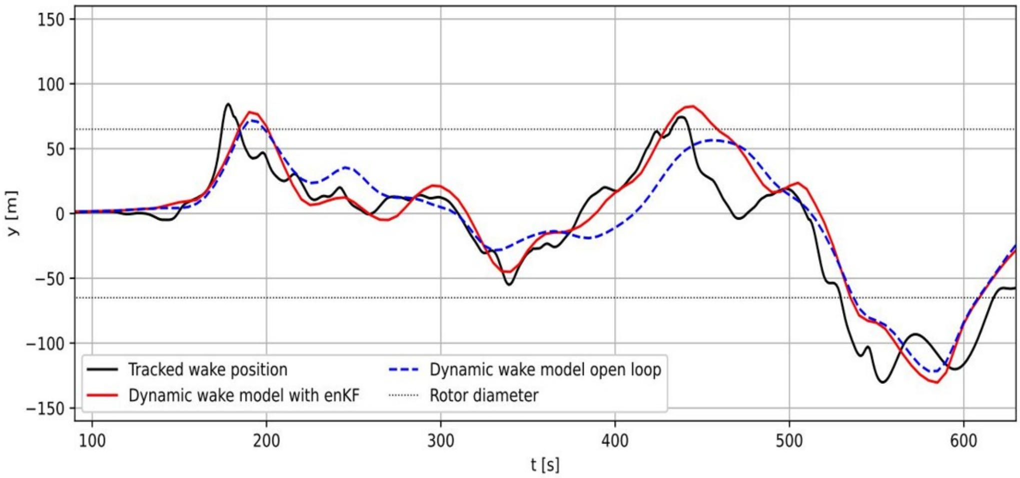

Figure 2.6. Lateral wake center position obtained from the tracking algorithm as well as estimated by the dynamic wake model.

Figure 2.6 reports the lateral position of the wake at the waked turbine over the simulation time. The measurement position is estimated by the wake tracking algorithm. It can be seen that the meandering wake center crosses the rotor several times, creating partial overlap conditions. This movement causes, together with further ambient turbulence, the fluctuations and differences in the sector wind speeds, as shown in **Figure 2.5**. The plane for wake position tracking is located $0.5D$ upstream of the rotor. To compensate the time delay, the measured curve was shifted in time by the assumed advection time of $U_w/D = 10s$. In the open loop configuration, the wake position is a result of the past input of environmental conditions at the upstream turbine and the advection process. The plots reported in **Figure 2.6** show that the wake movements in the order of $100s$ or larger than $0.5D$ are indeed captured by the open loop model. However, the corrected model with Kalman filter is able to show an improved agreement on the smaller fluctuations. A larger discrepancy starting at $450s$ is probably connected to a movement in the downward direction of the wake. This can be at the moment not captured and likely prevents a better correction here. As suspected in the previous figure, towards the end of the simulation, the wake is displaced in negative y-direction. At this point, both models show a higher discrepancy in the measurement. Observability is lost, as the wake does hardly impinge on the turbine at this point in time. This can be also seen in **Figure 2.5** where the sector wind speeds have almost the same value at $t = 600$ s. Overall, the RMSE on the total rotor inflow velocity is reduced from 0.63 $\mathrm{m\,s^{-1}}$ to 0.35 $\mathrm{m\,s^{-1}}$.

2.4 Conclusion

In this section the closed-loop formulation of the FLORIDyn model presented in [33] was described. Wind speed estimates from a load-based flow observer are implemented into an ensemble Kalman filter to correct the predictions of the model in terms of background flow velocity and position of the wake. Results from the study show that the proposed approach is capable of better following the effects of smaller inflow fluctuations compared to the open loop configuration. The additional information about the inflow provided by the observer improves the performance of the standard FLORIDyn framework in full wake conditions, opening up interesting opportunities for wind farm control applications. Further studies are needed to evaluate the potential applicability of the model in different environmental conditions, operative settings and more complex operative setups, considering the typical yaw-misaligned conditions used in wakesteering wind farm control.

Chapter 3

Mesoscale and wind farm scale wind field observation

In this section, a description of the satellite measurement principle is provided, discussing strengths and limitations of this technology in detail. Among the main drawbacks of SAR-based wind speed estimation is the need to extrapolate wind speed distributions—originally inferred at the sea surface—up to hub height. This extrapolation process introduces several levels of uncertainty and often results in inaccurate estimates when conventional approaches are used. A methodology based on the use of operational wind speed data from turbines is introduced in this thesis to recalibrate the extrapolated wind speeds. The ultimate goal of the study is to present a straightforward and cost-effective procedure that relies solely on operational turbine data and satellite imagery—freely available from public datasets—for use in monitoring, potentially the repowering of existing wind farms, and site assessment activities.

3.1 SAR wind fields

As it was reported in **Section 1.3**, satellite images from SAR (Synthetic aperture Radar) and Scatterometers provide useful information for offshore wind energy applications. The roughness, in the form of capillary and short-gravity waves, is induced by the sea surface wind stress and it is therefore reflected and detectable according to the Bragg reflection law by Satellite Sensors. The Radar Backscatter is correlated to wind velocities acquisition at 10 a.m.s.l (above mean sea level) using empirical Geophysical Model Functions (GMFs), that are calibrated against in situ measurements (eg. anemometric buoies). The formulation of a generic GMFs is reported in **Equation 3.1**:

$$\sigma_0 = U\,\gamma(\theta)A(\theta)\,[1 + B(\theta, U)\cos\varphi + C(\theta, U)\cos(2\varphi)] \tag{3.1}$$

where σ_0 is the recorded backscattered signal per unit area, also known as the normalized radar cross section (NRCS), U is the wind speed at a height of 10 m, θ is the local incident angle, and φ is the wind direction with respect to the radar look direction. The coefficients A, B, C and γ are functions of wind speed and the local incidence angle. As already mentioned, the wind retrieval process from SAR images requires the inversion of the GMF to calculate near-surface wind. Additionally, SAR sensors use a single viewing angle for each acquisition, and the resulting images do not inherently contain information about wind direction [64]. For real-time wind retrieval, a-priori knowledge of wind direction is required to avoid ambiguities. This directional information is typically obtained from numerical weather prediction models such as ECMWF (European Centre for Medium-range Weather Forecasts) or NO GAPS (Navy Operational Global Atmospheric Prediction System), WRF (Weather Research and Forecasting), ERA5 reanalyis data or in situ-measurements (ie meteorological mast or SCADA) but the results are only valid near the sensor on site as wind direction cannot be assumed constant for a region. The radiometric sensors used for wind energy applications operate in the range of the C-band (12-7.5 GHz), and smaller wave-lengths in the X band range (7.5-3.75 GHz). The GMFs were developed for the C-Band and have a nominal accuracy of +-$2ms^{-1}$. The latest and more accurate version for sensors operating in this band is the $CMOD.5N$. CMOD GMS are based on the hypothesis of neutral atmospheric stability. These functions are usually valid for a wind speed range around 2 ms^{-1}-30 ms^{-1}. SAR surface winds are obtained by inverting the backscatter with geophysical model functions. Sentinel 1-2 A-B which have been deployed for most of the studies available in the literature and also the investigated analysis of this thesis operate in C-band. GMFs originally were designed for scatterometers but were successively also deployed for SAR acquisitions. Differences from the SAR backscatter may occur due to different resolutions and the lack of inter-calibration between these two technologies. The most recent implementation is the $CMOD.5N$ [75]. As already mentioned, the hypothesis of neutral atmospheric stability in the GMFs for the C-Band and the need for extrapolating the wind speed to hub heights (around 100 m to have a significant value for wind energy) leads also to an error in the estimation: the empirical model functions rely on the assumption that wind speed increases logarithmically with height above the sea surface. This is normally true if the atmospheric boundary layer is neutrally stratified. Stable stratification would typically lead to an underestimation and unstable stratification to an overestimation of the 10 m wind speed. Deviations from the logarithmic wind profile are mostly found in near-shore areas where the atmospheric boundary layer may be influenced by the land. GMFs can thus be expected to perform better over the open ocean than in near-shore areas. Furthermore, these functions (GMFs) were designed empirically using the European Centre for Medium-Range Weather Forecasts (ECMWF) numerical model as a reference, which may not be accurate in coastal areas since in situ data were used only for validation and a posteriori bias correction. Improving the accuracy of SAR wind speed retrievals via refined GMFs is essential, particularly in wind energy applications, where the wind power density is proportional to the cube of wind speed and thus highly sensitive to estimation errors. As mentioned in **Section 1.3**, the nominal spatial resolution of SAR images is high (c.a 5-10 m for sensors operating in C-band) , but SAR acquisitions need to be spatially averaged to pixel sizes of around 500-100 m to reduce the effect of speckle noise, and inclinations of the sea surface due to long-period waves [64]. To quantify the degree of speckle-noise reduction, the Equivalent Number of Looks

($ENLs$) can be calculated using the following equation [54]:

$$ENLs = \mu + 2\sigma^2 \tag{3.2}$$

where μ is the mean and σ is the standard deviation of the intensity. Furthermore, a wide range of phenomena influences the sea surface and hence the radar backscatter. In general, the rough surfaces reflect most of the transmitted power to the antenna. Meanwhile, the smooth surfaces typically reflect little or no radiation to the antenna, making the areas appear dark in radar images for flat surfaces. The surface inclined toward the radar will have stronger backscatter (double bounce) than slopes away from the radar. An example of double bouncing could happen with existing ships in SAR scenes; therefore, the backscattered signal will be strong. **Figure 3.1** shows different possible scattering mechanisms in acquiring a SAR scene.

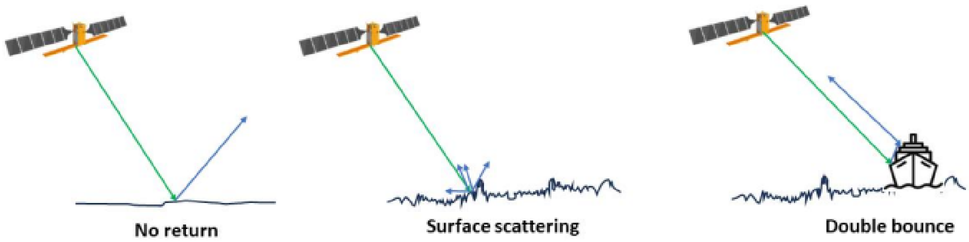

Figure 3.1. Different scattering mechanisms [61].

Therefore, the bright scattering from hard targets (eg., a wind turbine itself) increases the intensity of the backscattered signal over the sea, determining a fictitious increase in the wind speed, while surfactants, oil and algae blooms dampen the radar backscatter resulting in winds that are too low. SAR data in very shallow water are also affected by oceanic effects not related to surface windspeeds or sea surface effects: the bathimetry , for instance, might influence the small waves at the sea surface and therefore the radar-backscatter. The effect of oceanic processes related to currents, fronts, eddies, swell, and internal waves are partially revealed by anomalous Doppler shifts in the received signal, also known as Doppler Centroid Anomaly, which coupled with GMF may improve the SAR wind retrieval. To avoid contamination from strong radar reflections of turbine structures, wind speeds from SAR images are evaluated at a safe distance from the wind farms—ranging from 200 meters to several kilometers, depending on the case study [62]. Specific algorithms, called CFAR (Constante False Alarm Rate) can be also applied to the backscattered image to mitigate the effects related to hard target reflections [63]. **Figure 3.2** illustrates the SAR imaging geometry where the platform moves in an azimuthal direction.

The slant range refers to the perpendicular distance to the radar's flight pattern. The swath width gives the ground-range extent of the radar scene, which depends on the duration of the turn-on of the radars. Imaging radar has two resolutions: the slant range resolution δ_r and the azimuthal resolution δ_a. δ_r is represented as a function of the length duration of the pulse, and modern SAR systems modulate

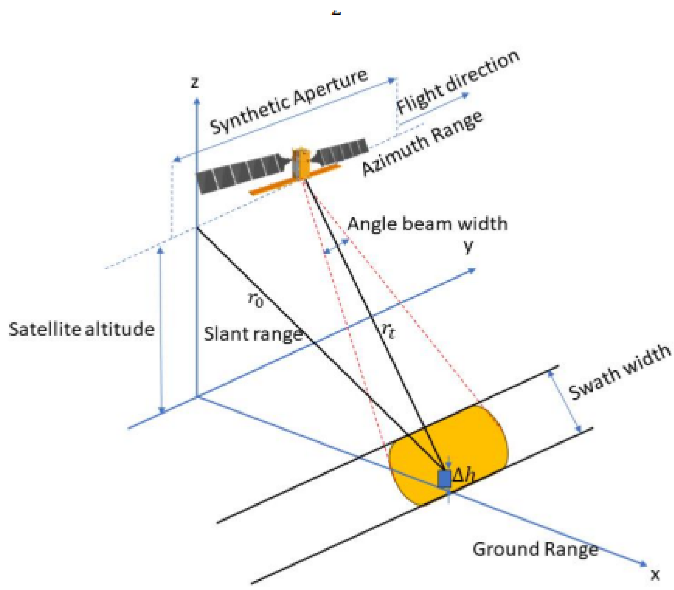

Figure 3.2. Schematic SAR acquisition geometry [61].

their radar frequency over the bandwidth B, and it is inversely proportional to the B of the transmitted pulse.

$$\delta_r = \frac{c_0}{2B} \tag{3.3}$$

where c_0 is the light speed. The azimuthal resolution δ_a is independent of δ_r and depends on the path of the synthetic aperture., and it is proportional to the physical length of the antenna l. Surprisingly, the relation shows that small l means finer resolution, but there is a limitation from the hardware and imaging radar perspective of l.

SAR Sentinel 1 from the Copernicus program operates in different acquisition modes as reported in **Figure 3.3** :

- Strip Map Mode (SM) with a swath width of 80 km;
- Interferometric Wide (IW) swath with a swath width of 250 km
- Extra-Wide (EW) swath width of 410 km and wave (WV) with 20 km swath width.

The IW swath acquisition mode is the most commonly used for retrieving acquisitions over land and sea [64]. An important characteristic of the acquisition model is also the polarization of the emitted and received signal [56]. Polarization refers to the direction of travel of an electromagnetic wave vector's tip: vertical (up and down), horizontal (left to right), or circular (rotating in a constant plane left or right). The direction of polarization is defined by the orientation of the wave's electric field, which is always 90°, or perpendicular, to its magnetic field. A radar antenna can be designed to send and receive electromagnetic waves with a well-defined polarization. By varying the polarization of the transmitted signal and receiving several different polarized images from the same series of pulses, SAR systems

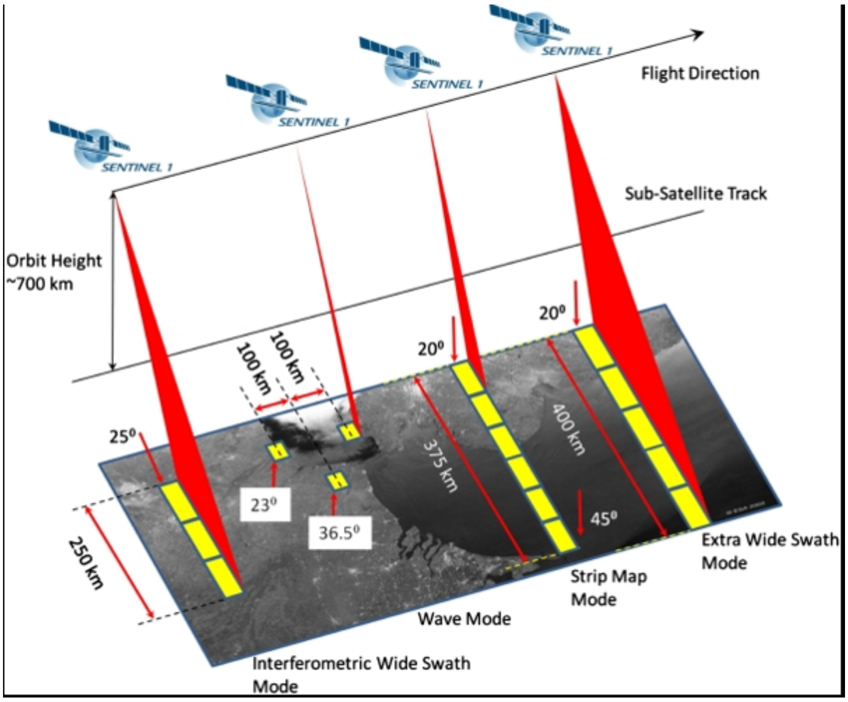

Figure 3.3. Sentinel-1 acquisition modes [31].

can gather detailed information on the polarimetric properties of the observed surface, which can reveal the structure, orientation and environmental conditions of the surface elements. Multiple polarizations and wavelength combinations provide different and complementary surface information. Imaging radars can have different polarization configurations. A single-polarization system, or "single-pol," transmits and receives a single polarization, typically in the same direction, resulting in a horizontal-horizontal (HH) or vertical-vertical (VV) imagery, where the first designation refers to the transmit direction and the second to the received one. A dual-polarization system, or "dual-pol," might transmit in one polarization but receive in two, resulting in either HH and HV or VH and VV imagery. Dual polarization provides additional detail about surface features through the different and complementary echoes. VV polarized data are more sensible to sea roughness induced by wind and waves [49]. However in some cases, because of the unavailability of this polarization format also HH images can be used. In the latter case, a polarization ratio to transform the NRCS of HH to VV with a factor that depends on the data, frequency band, and incidence angle, can be used to compensate for the underestimation of the wind speed in CMODs [43].SAR data can be distributed in different formats. Originally they were available as raw data (Level 1). The user had to calibrate the SAR data with (updated) calibration coefficients provided with the SAR product or separately. The calibration error should not exceed 0.5 dB, leading to an uncertainty on wind speed of roughly 0.5 ms^{-1}. As the standard deviation from the validation results is found to be much larger, around two to four times the calibration uncertainty, there is scope for improvement in SAR wind retrieval. SAR images are not projected to a geographical coordinate system and the user has to do this. The correction for incidence angle across the swath also has to be made by the user. Already processed DATA are directly at the user's disposal from the Copernicus database, which are also called Level 2. These processed products consist of geolocated geophysical products derived from Level-1. Level-2 Ocean (OCN) are used for wind, wave and currents applications More details about the available databases are reported from the Copernicus archive [31]. As it was

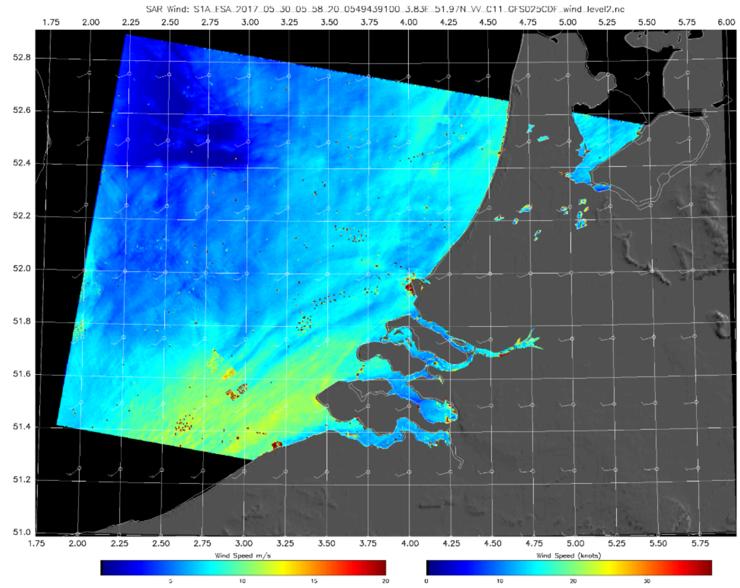

Figure 3.4. Visualization of a SAR Sentinel-1 derived wind speed map [82].

already mentioned in **Section 1.3**, the sampling rate is limited to each passage of the satellite to the same location (around 6 days between each passage for SAR data [64]) and therefore inter-calibration among different satellite sensors would be required in order to reduce the time lapse between consecutive acquisitions. A procedure for recalibrating the parameters of the GMFs of different sensors was proposed in [10]. SAR retrieved winds have been validated by comparing them to observations from meteorological masts, ships, buoys, scatterometer or atmospheric model results. In general, the validation results show a bias less than 0.5 ms^{-1} and standard deviation from 1.2 to 2.0 $ms-1$ [64]. The accuracy of collocation, the uncertainty on the in-situ observations and atmospheric model results, and also the time-averaging method have to be considered. The main challenge in co-locating SAR-derived wind speeds with in-situ ocean buoy measurements lies in the mismatch between their spatial and temporal resolutions. SAR provides high spatial resolution snapshots of the wind field over large areas, acquired in just a few seconds, but with low temporal frequency. In contrast, on-site measurements from ocean buoys are typically recorded at fixed points with high temporal resolution, often as 10-minute averaged wind speeds.

To address this disparity, Taylor's hypothesis of frozen turbulence is commonly applied. This approach assumes that wind structures are advected by the mean wind without significant evolution over time, allowing the spatial footprint of SAR to be translated into a time-equivalent reference. However, it is critical to ensure that both spatial and temporal scales are compatible for the co-location to be meaningful [64].

Currently, there is no standardized procedure in the literature for such co-location. One approach adopted in [11], [2] involves defining a box-shaped footprint upstream of the measurement mast or buoy, aligned with the wind direction obtained from the vane. The size of this footprint is then derived by applying Taylor's hypothesis to match the SAR snapshot to the buoy's temporal averaging window, enabling more consistent comparisons between the two datasets.

The main applications of SAR images for wind energy are related to:

- Site assessment: Weibull distribution and wind rose statistics can be computed from multiple (1 year) acquisitions in a potential site. However given the limited spatial and temporal resolution, at current state satellite data are not bankable compared to the measurements of other sensors and could only be used to identify a potential site for the pre site of a met mast or the deployment of floating LiDARs in an area of interest [64], [3]. In addition, the low sampling rates and fixed overpass times of SAR limit its ability to capture diurnal wind cycle effects, especially when acquisitions are available from a single satellite.

- Analyzing horizontal wind speed gradients induced by the coast [4],[34] for site assessment from satellite images, which have a better resolution than commonly used atmospheric models;

- Evaluation of wind climate models (ie. WRF) [2], [10], which usually have a coarser resolution than satellites [3];

- Impact of wind farms (wind resources) and wind farm monitoring: the drop in velocity downstream a wind farm correlated to the propagation of the cluster Wake can be observed from satellite images [41], [53], [66], [62];

- Observation of mesoscale wind phenomena exploiting the spatial coverage, in the order of hundreds of kilometers, from satellites [72], [71];

As highlighted earlier, a major limitation of SAR-inferred wind speeds, apart from satellite low sampling rates, is that they are referenced to a measurement height of 10 m a.s.l Since hub heights of wind turbines usually exceed hundred of meters, it is necessary to extrapolate the wind profile to heights of interest for wind energy applications. The extrapolation of satellite winds is a non trivial task, given the effects of different atmospheric conditions on the wind speed profile, especially when local measurements are not available [9], [55]. Different approaches have been explored in the literature for "lifting" satellite wind maps.Formulations based on the Monin-Obukhov similarity theory (MOST) [74], implemented for the atmospheric stability correction of the vertical wind profile, were proposed in [8], using dataset computed from the atmospheric model WRF. However, the MOST is valid for describing turbulent fluxes within the surface layer. While MOST-like formulations can be still successfully employed to correct the wind profile within the lower 200 meters of the ABL in unstable and neutral cases [9], they show more limitations in stable conditions. Alternative data-driven methodologies were proposed for the instantaneous extrapolation of satellite maps. In [55] a machine learning algorithm, was implemented using meteorological parameters extracted from a high-resolution numerical model and trained with lidar-derived vertical wind profiles. The algorithm was able to extrapolate sea surface wind speeds at various altitudes up to 200 m with good results when tested against lidar measurements. The proposed methodology however, requires a significant amount of co-located lidar SAR observations to be implemented over a site (more than 1000 collocated data points were used in [55]), which might not be available at every site, taking into account the low sampling rate of satellites and the limited number of samples especially for the most recent satellite missions, alongside the use of additional external LiDAR wind profiler devices. A different approach relies on the long therm stability correction presented in [48], which is based on a probabilistic adaptation of the MOST-based wind profile. The long-term stability correction derived from this methodology can exhibit positive or negative values depending on the considered height, as it combines both stable and unstable terms. The adaptation of MOST can effectively be applied up to turbine operating heights since the long-term stability correction falls within the range where MOST is valid. The long term corrective factor was computed using the stability information from WRF and the ERA5 relative to the whole time interval of the observations. Extrapolated mean SAR wind speed showed similar results to the atmospheric model extrapolated velocities, with the advantage of providing a higher level of spatial detail and being based on real observations [9]. The drawback of this long-therm methodology however is that individual samples of the wind speed are not preserved, disguising the potential influence of particular mesoscale effects that modify the average wind profile.

3.2 Methodology: improving the accuracy of SAR-based wind speed estimates using SCADA data

3.2.1 Extrapolating Satellite winds to hub-height

In this part of the thesis, the extrapolation problem is investigated by introducing a new methodology: SAR-derived wind speeds are combined with SCADA data from an offshore wind farm. In fact, the idea behind this work is that SCADA data from operating wind turbines provide in situ measurements that can be leveraged to improve SAR observations and to increase the accuracy of the extrapolation at hub height. The combination of satellite images with operative SCADA might be employed for activities related to the preliminary site assessment of areas in the surrounding of existing wind farms. The spatial coverage of SAR re-tuned wind maps might provide more accurate information on the distribution of wind resources, for example, related to horizontal wind speed gradients induced by coastal orography, or to the propagation of cluster wakes. Such information can be extremely valuable to reduce risks in the repowering of existing plants or the planning of new offshore sites. The combination of satellite images with SCADA data might also represent an economically valuable alternative for the end-user wind farm operators since it is based on already available recorded operative information of the plant, and satellite images which for some space programs, such as Copernicus, are available from open source databases, without the requirement of additional external devices.

3.2.2 Case study: Westermost Rough Wind farm

The offshore wind farm Westermost Rough, located near the East coast of England, was investigated for this study. It is a medium-sized plant placed between 8 and 14 km from the shore. It consists of 35 turbines with a nominal power of 6 Megawatt, a cut-in wind speed of approximately 5 ms^{-1} and cut-off of approximately 25 ms^{-1} . Their hub height is 102 m, while the rotor diameter D is 154 m [5]. **Figure 3.5** shows the layout of the wind farm. Turbines are placed in a regular disposition with internal spacings of 950 m (6.2 D) and 1140 m (7.4 D). There is a gap in the regular grid between rows C and D.

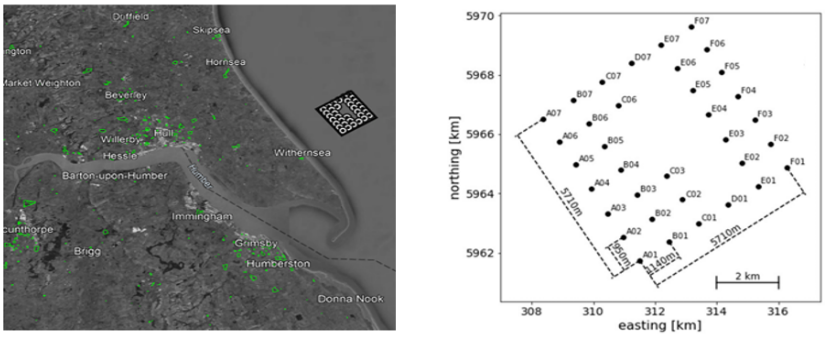

(a) (b)

Figure 3.5. (a) Location of the Westermost Rough wind farm (b) Wind farm layout. [5]

3.2.3 Dataset: SCADA and SAR wind maps

A data set consisting of 10-min SCADA measurements (nacelle wind speed, electrical power, rotor speed, yaw position and pitch angle) from all turbines [60], and 378 SAR images from Sentinel 1A-B referring to the years 2016-2017, acquired in IW mode was used for the study. Wind speed maps from satellite data were obtained from the GMF CMOD.5N and are characterized by a resolution of 100 m per pixel after the application of the multi-looking process. The wind direction input to the GMFs was taken from the ERA5 global reanalysis data at 10 m height. The speed range of the SAR wind maps is between 2-23 ms^{-1}.

3.2.4 Data-Driven recalibration of SAR-extrapolated wind speeds using SCADA data

The proposed methodology for improving hub-height satellite-derived wind fields with operative turbine data involves two main steps: first, the SAR wind speeds are lifted to the 102 m reference hub height according to **Equation 3.4**, and then a recalibration procedure is introduced to correct the derived SAR wind speeds by comparing them with spatiotemporal co-located nacelle velocities. The time syncronization between the two datasets is obtained selecting operative turbine data corresponding to the satellite overpassess. The spatial colocation between the datasets is performed extracting SAR wind speeds applying a moving average to the satellite wind map in front of the external rows of the turbines, as explained in detail in the following pages.The extrapolation of SAR wind speeds is performed using the MOST-like formulations introduced in [74],[8]. The wind speed at a generic vertical height (z), corrected with a stability term assumes the form [74]:

$$u(z) = \frac{u_*}{k}\left[\ln\left(\frac{z}{z_0}\right) - \Psi\right] \tag{3.4}$$

Where Ψ represents the MOST correction term. It is a function of the vertical coordinate z and the Monin-Obukhov length parameter L that characterizes stability effects (buoyancy versus shear turbulence) in the turbulent layer of the atmosphere near the surface. It is defined as:

$$L = -\frac{Tu_*^3}{\kappa g \overline{w'\theta_v'}} \tag{3.5}$$

where T is the air temperature, u_* is the friction velocity, $\kappa \approx 0.4$ is the von Kármán constant, g the Earth's gravitational acceleration, $\overline{w'\theta_v'}$ the kinetic virtual heat flux, where w' is the vertical component of the wind speed, and θ_v' is the virtual potential temperature. The Obukhov length L is calculated from ERA5 reanalysis parameters referred to the time interval of the analyzed dataset (2016-2017), following the steps reported in [1]. The mean temperature and heat fluxes in **Equation 3.5** are replaced by the ERA5 parameters air temperature at 2 m and surface sensible heat flux, respectively. Additionally, friction velocity values from ERA5 are also utilized [1]. Given the coarser resolution of the ERA5 grid ($\approx 30\,\text{km} \times 30\,\text{km}$) for atmospheric variables compared to the investigated area around the wind farm from the satellite images, as a first approximation, a single value of L at the point in the center of the wind farm is selected. For stable atmospheric conditions, ($0 < L < 1000$) [79], [8] Ψ can be expressed as [74], [8]:

$$\Psi = -4.7\frac{z}{L} \tag{3.6}$$

for unstable conditions ($-1000 < L < 0$) [74], [8]:

$$\Psi = \frac{3}{2}\left[\ln\left(\frac{1+x+x^2}{3}\right) - \sqrt{3}\tan^{-1}\left(\frac{2x+1}{\sqrt{3}}\right) + \frac{\pi}{\sqrt{3}}\right] \tag{3.7}$$

with:

$$x = \left(1 - \frac{12z}{L}\right)^2 \tag{3.8}$$

At first, both SCADA data and satellite images are classified based on atmospheric stability according to the Obukhov similarity theory, as computed from ERA5 reanalysis data, and binned based on the wind direction in different sectors. In a preliminary phase of the study, 12 sectors of 30 degrees of amplitude each were considered. The bin width was selected to have a sufficient number of images for bin, which -due to the lower sampling rate of the satellite- is more limited compared to the number of available SCADA measurements. This subdivision was made at first in order to analyze wind speed distributions for different wind directions from SCADA data and SAR-derived wind speeds in different atmospheric conditions and evaluate how the two different velocities compare. As mentioned in the **Section 3.1**, the available datasets need to be spatially and temporally co-located to compare SAR and SCADA wind speeds. SAR images provide a snapshot over an extended area of wind field distributions, while SCADA data are spatially localized acquisitions at higher temporal resolution. Satellite-inferred wind speeds are also affected by different external sources of errors determining the intensity of the backscatter, such as hard targets like ships or turbines. Wind retrievals within the wind farm itself can be contaminated by reflections from the wind turbines. Therefore, it is not recommended to use those values quantitatively, though the raw satellite image can still contain qualitative information of the flow patterns within the wind farm [5].

Only satellite-derived wind speeds outside the wind farm area are considered and compared with SCADA data from the outermost rows of turbines. The presence of turbines also affects the intensity of the reflected signal in the surroundings of the plant. Therefore, transects used for extracting wind speed must be placed at a certain distance from the perimeter rows of turbines to avoid signal contamination [62]. Additionally, the SCADA data utilized refer exclusively to freestream turbines.

Before implementing the co-location procedure, a sensitivity analysis was performed by extracting wind speeds along external linear transects parallel to the upstream rows of turbines (**Figure 3.6**). The distance from the wind farm was progressively increased, starting from 200 m away from the perimeter. As shown in the figure, fluctuations in the inferred wind speeds gradually decrease with increasing distance from the plant, while the average global trend along the transects is preserved. This observation supports the reasonable assumption that turbine reflections are responsible for these fluctuations.

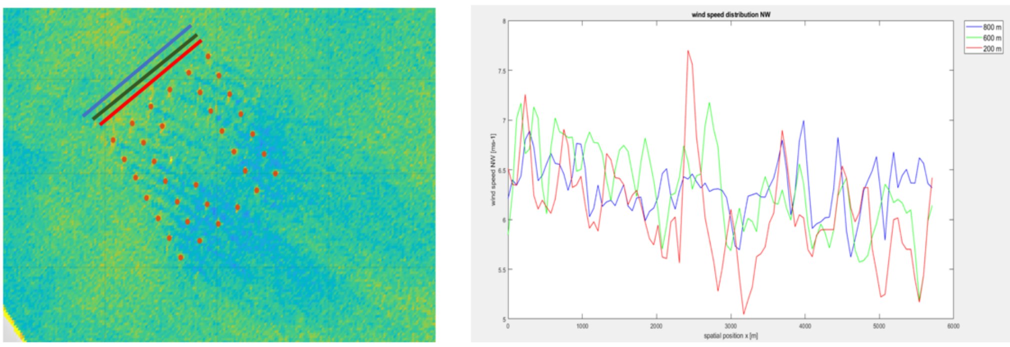

(a) (b)

Figure 3.6. (a) Progressive increase in the distance of the transects used for wind speed extraction from the outer rows of the Westermost Rough wind farm.(b) Corresponding wind speed trends along the extracted transects.

Following this analysis, satellite wind speeds were extracted from transects placed at 800 m from the wind farm perimeter, applying a moving average filter in the shape of a rectangular box (**Figure 3.7**). This distance and filtering approach were chosen to minimize the influence of turbine reflections and other external factors affecting SAR acquisitions while preserving spatial co-location with SCADA measurements as much as possible. In this study, wind turbines are therefore treated as a cluster of anemometric buoys providing in-situ wind speed measurements. After applying

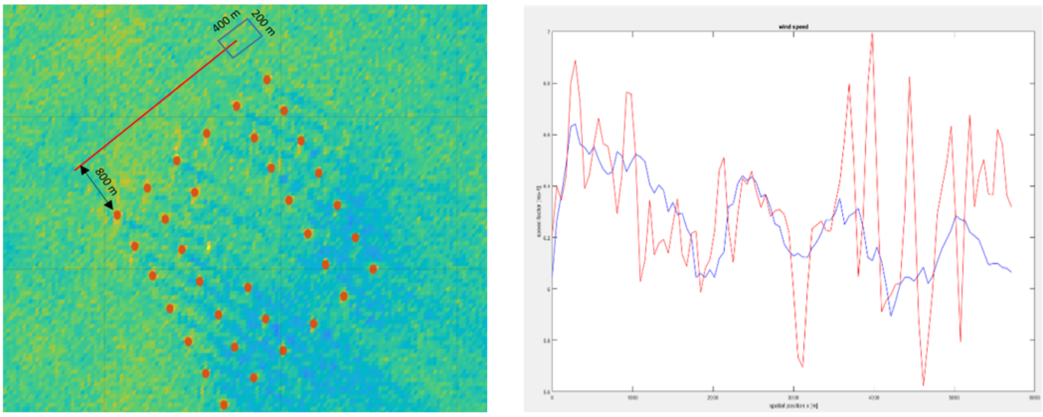

(a) (b)

Figure 3.7. (a) Definition of the moving average for extracting wind speeds from satellite images.(b) Comparison of the wind speed trends along the transect (red line) with the corresponding velocities filtered using the moving average (blu line).

the moving average filter, the "co-located" SAR and SCADA wind speeds can be directly compared, enabling the implementation of a recalibration step. **Figure 3.8** reports as an example, a comparison of co-located SAR and SCADA wind speeds at hub height, referred to a wind direction bin for individual turbines in a row before recalibration, under stable and unstable atmospheric conditions. Overall, the root mean square error (RMSE) and correlation between datasets are comparable to values reported in the literature for most wind directions, with better agreement generally observed under stable conditions. However, comparisons in the literature have mostly been conducted using meteorological masts or anemometric buoys, rather than SCADA data [9], [55]. In addition, the number of samples available for this directional bin size is smaller than in previous studies comparing SCADA data with extrapolated SAR wind speeds [2].

Residuals between the co-located nacelle anemometer and SAR-extrapolated velocities are normalized by the corresponding SAR-extrapolated velocity.

$$\frac{U_{SCADA} - U_{SAR}}{U_{SAR}} \tag{3.9}$$

An analysis of the trends in the distribution of these residuals under varying wind directions and atmospheric stability conditions has been conducted.

In this recalibration procedure, only the external row of turbines fully exposed to freestream conditions at a given wind direction are considered. Freestream conditions are defined as illustrated in **Figure 3.9**, where the wind rose is divided into four quadrants. When the wind originates from a direction within a specific quadrant, the corresponding outer row of turbines and the SAR wind speeds extracted from transects located 800 m upstream are considered to be in freestream conditions. For example, if the wind comes from the North-East quadrant, row F **Figure 3.5** and the associated transect wind speeds are treated as freestream. In cases where the wind direction is exactly 0°, 90°, 180°, or 270°, two perimeter rows are simultaneously considered to be in freestream.

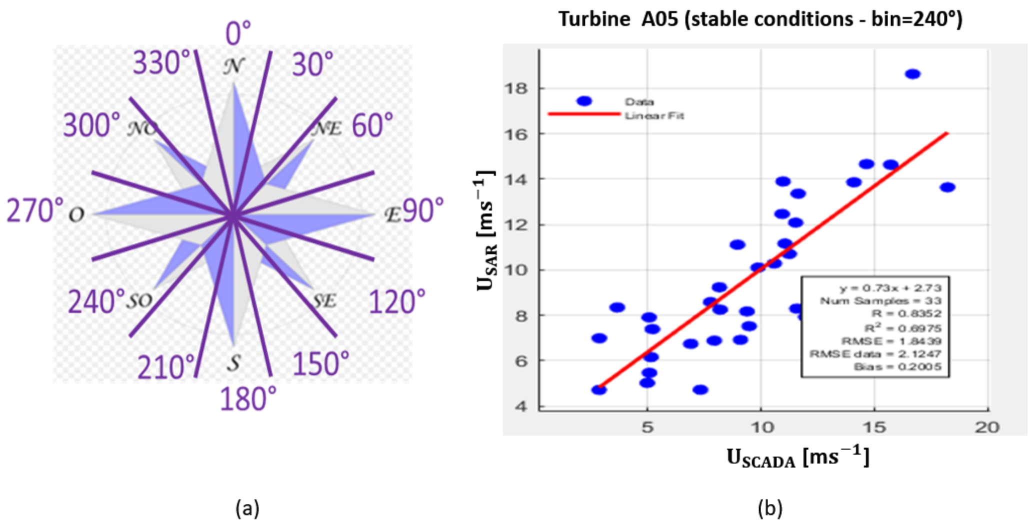

Figure 3.8. (a) Definition of the wind directional bins, each spanning 30 degrees. (b) Comparison between anemometric SCADA wind speeds for turbine A05 (**Figure 3.5**) and the corresponding extrapolated SAR wind speeds, extracted using a moving average applied along a segment located 800 m from the perimeter of the wind farm.

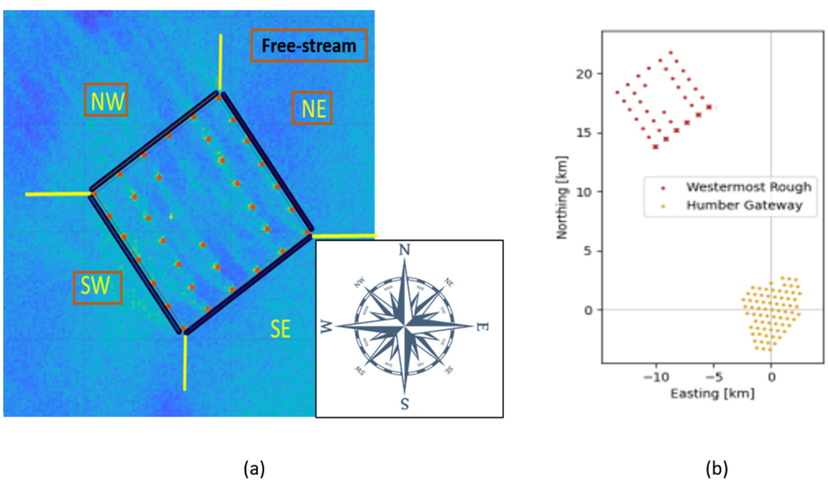

Figure 3.9. (a) Definition of freestream quadrants. (b) Location of the Humber Gateway wind farm near Westermost Rough.

Since the cluster wake of the nearby Humber Gateway wind farm (**Figure 3.9b**) affects Westermost Rough under south-easterly wind conditions, turbines in row A01-F01, which are not in freestream under these conditions, are excluded from the dataset.

This analysis focuses on recalibrating the extrapolations based on the formulations in **Equation 3.4**, which are valid under freestream conditions. For south-easterly winds, however, the wind profile is distorted by the wake deficit generated by the Humber Gateway cluster, thereby violating the underlying assumptions of the model. **Figure 3.10** shows the distribution of residuals as a function of wind direction. **Figure 3.11** shows the residuals between co-located SCADA and "extrapolated"

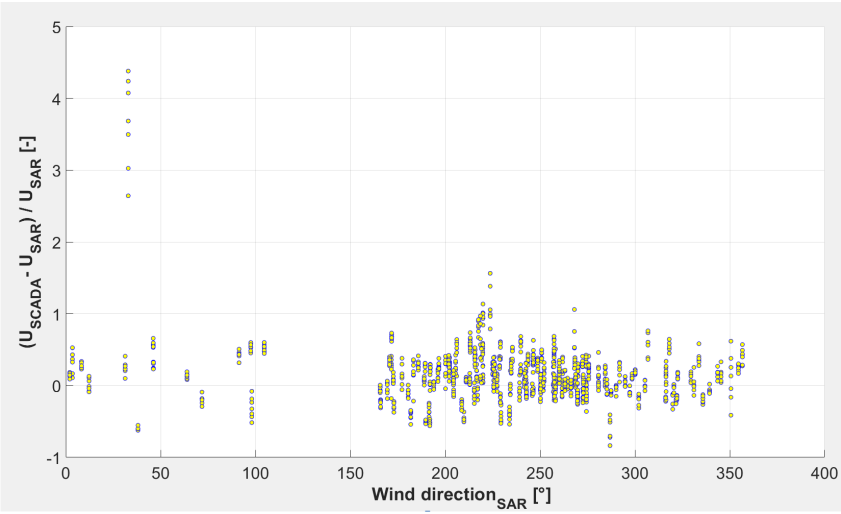

Figure 3.10. Distribution of the residuals between co-located extrapolated SAR and SCADA anemometric wind speeds for all turbines operating in freestream conditions, as a function of wind direction

SAR wind speeds as a function of the Obukhov length in stable and unstable atmospheric conditions.

Overall, independently from the wind direction, the distribution in **Figure 3.11** shows a growing trend from negative to positive values of the residuals for stable conditions, heading towards an asymptotic value between 0.3 - 0.4 [-] for neutral conditions, corresponding to increasing values of L (L increasing towards 1000). On the other hand, for the unstable case, the residuals show an opposite behavior going from high positive values of the normalized residuals decreasing progressively for negative values of L. A curve-fitting approach, reported in **Figure 3.12**, is used to model the residuals as a function of atmospheric stability in order to recalibrate the satellite-extrapolated wind. The procedure is applied separately to the unstable and stable distributions resulting in the two curves reported in the **Figure 3.11**. As a first step of the implemented procedure, the stable and unstable clusters of residuals are divided into a subset of data for the training (70 % of the complete stable and unstable dataset, made of 985 and 793 co-located SAR-SCADA samples respectively in total) and testing (30 %). A cross-validation methodology is applied to the training dataset, which is further divided in 5 subsets of data, to identify the coefficients of the best-fitting curve for the distributions. As a result of the calculation, a power

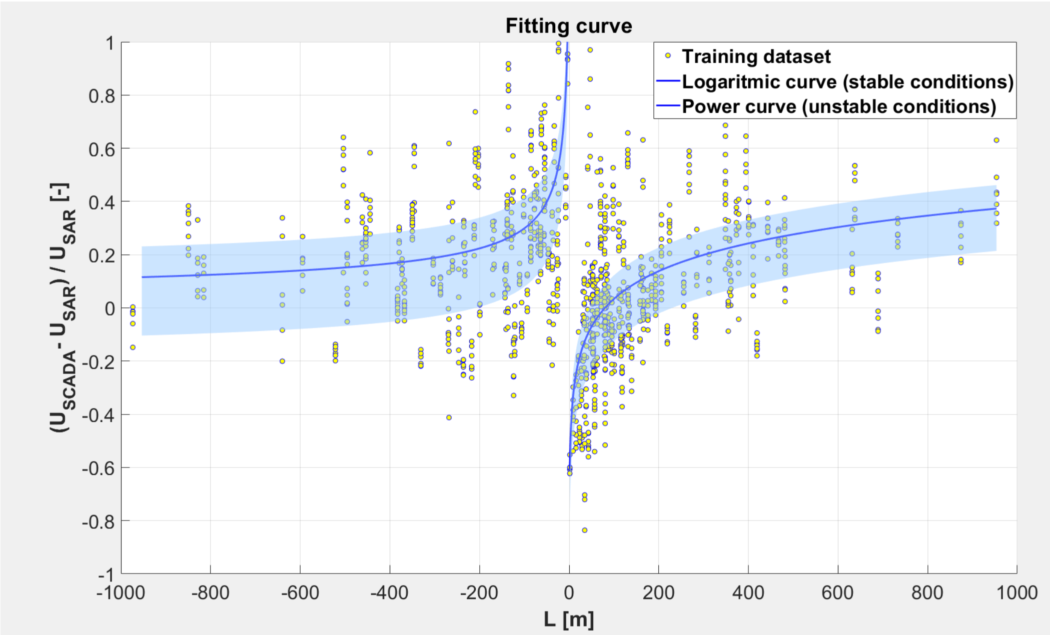

Figure 3.11. Distribution of the normalized residuals between extrapolated SAR and co-located SCADA wind speeds for different values of the Obukhov length. The figure also shows, in blue, the fitted curve used to model the distribution ($fit^{norm}(L)$), along with its associated uncertainties, computed using the interquartile range.

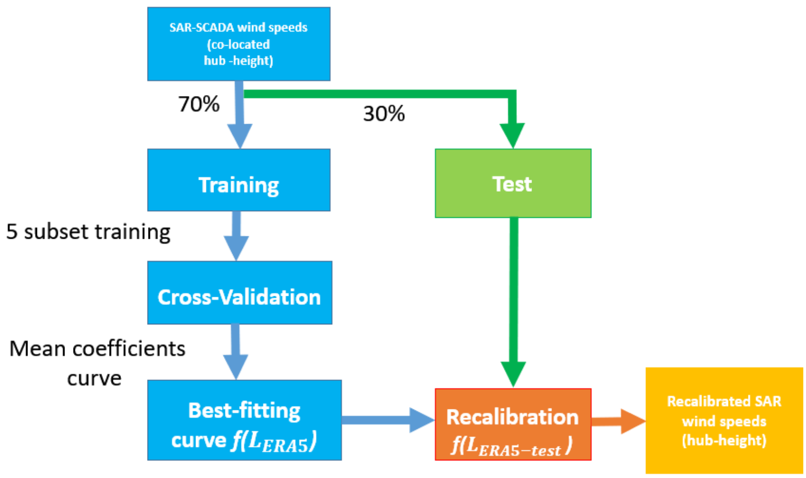

Figure 3.12. Schematic flowchart of the methodology adopted for recalibrating SAR-extrapolated wind speeds using co-located SCADA anemometric data.

and a logarithmic curve are used to fit the distribution of wind speed residuals (**Equation 3.9**) for unstable ($-1000 < L < 0$) and stable ($0 < L < 1000$) conditions, respectively. These fits, reported in **Figure 3.11**, express the residuals as a function of atmospheric stability, enabling the recalibration of the satellite-extrapolated wind speeds. As shown in **Figure 3.11**, the trends of the residuals show a high scatter, particularly under unstable and stable conditions within the ranges ($-200 < L < 0$) and $L > 200$ respectively, while the tails of the distributions tend to stabilize towards positive residuals for neutral atmospheric conditions. This behaviour is likely partly related to the higher number of samples for available for ($-200 < L < 200$), but it may also reflect the influence of atmospheric stability on the extrapolated wind profile. In particular, the MOS corrective term Ψ tends to reduce its magnitude for larger absolute values of L, which correspond to near-neutral or neutral conditions where the effect of the stability term becomes negligible. It is important to recall that SAR-derived wind speeds are an indirect estimate based on the intensity of the backscattered signal, which is influenced by various factors [64]. These include hard targets, surface roughness induced by eddies, atmospheric conditions, long-term ocean waves, and bathymetric features. In addition, potential interactions between the wind farm and the atmospheric flow—such as the induction zone, gravity waves, the development and recovery of the marine atmospheric boundary layer (MABL), and horizontal coastal wind speed gradients—may also affect the received radar signal.

All these external influences may contribute to the scattered distribution of the residuals observed in the comparison between SAR and SCADA wind speeds. Therefore, to evaluate the consistency of the residual model, the same best-fitting procedure was applied to wind speeds extracted from transects located at increasing distances from the wind farm, specifically at 1000 m and 1200 m, using the moving average method shown in **Figure 3.7**. As it can be seen from **Figure 3.13** the shape of the fitting curves is overall not affected by increasing distances from the wind farm confirming the relation between the values of L and the distribution of the residuals. Furthermore, the uncertainty of the curves is overlapping and small discrepancies observable in the curve shapes are completely within the uncertainty ranges of the trends inferred for different clearances.

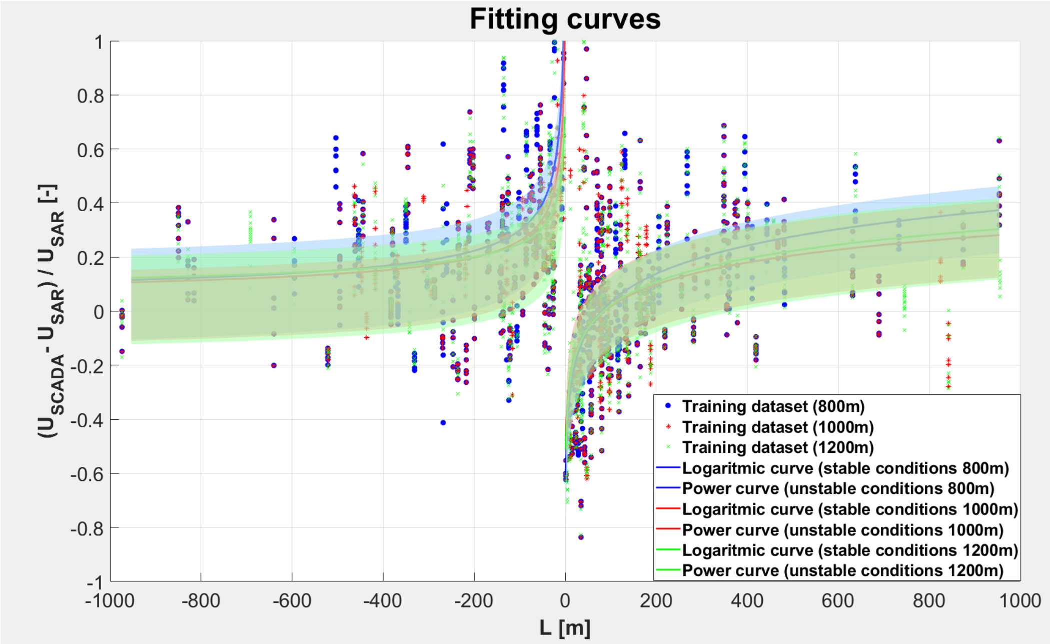

Figure 3.13. Wind speed residual fitting curves as a function of the Obukhov length L, evaluated for transects positioned at progressively greater distances from the wind farm, using the moving average method shown in **Figure 3.7**.

3.3 Results

The application of the nonlinear fit to recalibrate the SAR data is evaluated over an independent subset of the available measurements for stable and unstable conditions, corresponding to c.a the 30% of the full datasets, which was not used to derive the fitting (**Figure 3.12**).

Figure 3.14 and **Figure 3.15** compare the SAR and SCADA co-located wind speeds before and after the recalibration process, showing an improved agreement for both the stable and unstable case in terms of reduced RMSE, bias and mean absolute error (MAE). Only a minimal decrease in the correlation (R) for the unstable case (**Figure 3.15**) is observable after the correction, which is still over 90% and compensated by an overall improvement of the other metrics. It is also observable how the slope of the linear fit of the residuals after the correction is closer to 1.

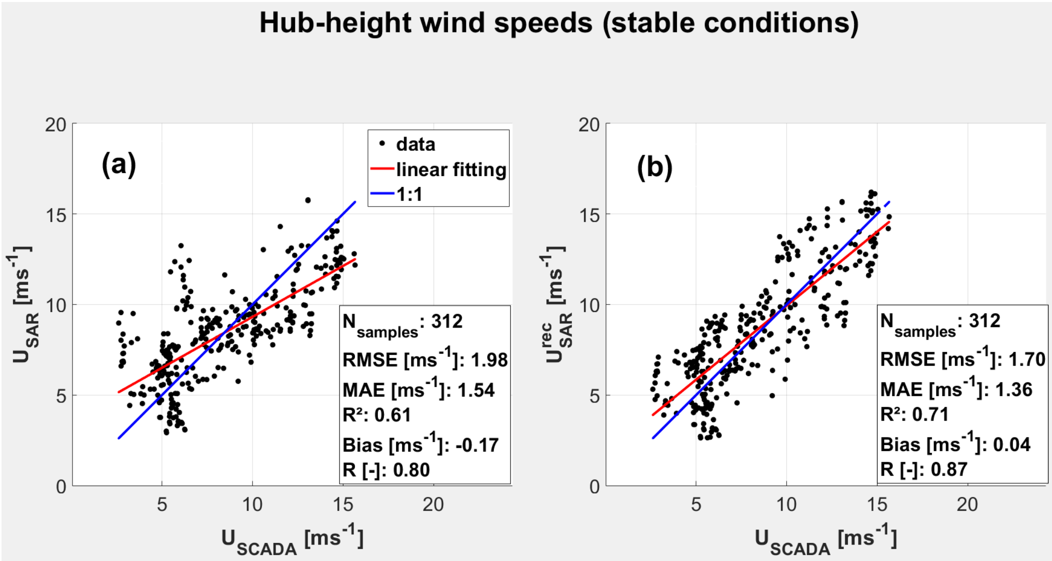

Figure 3.14. Comparison between the scatter plots of SCADA and co-located SAR wind speeds under stable atmospheric conditions, before (a) and after recalibration ($U_{\mathrm{SAR}}^{\mathrm{rec}} = U_{\mathrm{SAR}} + \mathrm{fit}^{\mathrm{norm}}(L) \times U_{\mathrm{SAR}}$) (b). The figures also shows the RMSE, the Mean absolute error (MAE) and the correlation coefficients (R) between the two datasets. The quality of the linear fit is evaluated using the coefficient of determination (R^2).

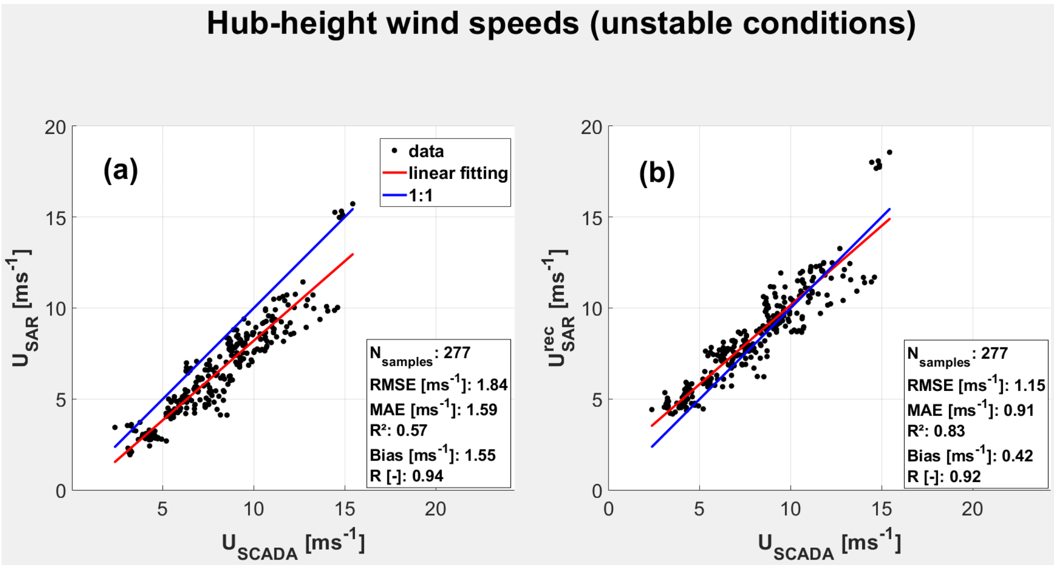

Figure 3.15. Comparison between the scatter plots of SCADA and co-located SAR wind speeds under unstable atmospheric conditions, before (a) and after recalibration ($U_{\mathrm{SAR}}^{\mathrm{rec}} = U_{\mathrm{SAR}} + \mathrm{fit}^{\mathrm{norm}}(L) \times U_{\mathrm{SAR}}$) (b). The figures also shows the RMSE, the Mean absolute error (MAE) and the correlation coefficients (R) between the two datasets. The quality of the linear fit is evaluated using the coefficient of determination (R^2).

3.4 Conclusion

In this part of the thesis, a new methodology for extrapolating instantaneous SAR wind maps to hub-height has been introduced based solely on the use of operative nacelle data.The implemented best-fitting of the residuals between SAR and SCADA wind speeds for the recalibration of the extrapolated data set was tested on an independent subset of the data not used for the recalibration. The obtained results show an improved extrapolation compared to basic MOST algorithms, opening new opportunities for the application of this procedure.

Wind speeds extrapolated to hub height and recalibrated with SCADA data can potentially be used to map available wind resources around existing operating wind farms, enabling more detailed analyses of horizontal wind speed distributions influenced by coastal effects. Such information is potentally valuable for repowering existing plants or planning new offshore wind farms near established ones. The presented methodology offers an alternative to using LiDAR measurements, meteorological masts, or long-term stability corrections for satellite wind extrapolation, relying instead on data from sensors already installed on operational wind turbines. This approach leverages turbines as in situ measurement points, potentially reducing the need for additional on-site devices. From the analysis of the data and atmospheric parameters computed from ERA5, a pattern has been identified in the distribution of residuals between co-located SAR and extrapolated SCADA wind speeds as a function of the Obukhov length L (**Figure 3.11**). Further studies are necessary to better understand the underlying causes of this trend. A comprehensive investigation into the effects of other atmospheric parameters (e.g., potential temperature gradient or Bulk Richardson number [64]) and wind direction would enable a more detailed analysis of possible influences stemming from the combination of coastal orography and the marine atmospheric boundary layer (MABL) recovery [34], potentially revealing additional patterns in the data distribution.

A larger number of samples is also required to obtain a more accurate characterization of the fitting trends: for high absolute values of L, the atmospheric boundary layer (ABL) tends toward neutral conditions, corresponding to two distinct asymptotes for positive and negative L. However, it remains unclear whether this difference is statistically significant or simply a consequence of the limited data availability, as the observed mismatch falls within the uncertainty range of the fitted curves.

An extended analysis involving co-located datasets from other sites is recommended to assess whether these findings are specific to the local climatology and morphological features or if they represent more generalizable trends. More sophisticated approaches, such as machine learning techniques [55] or the prediction of wind observers [24], [20], might also be used in the future to improve the accuracy of the recalibration process. A detailed comparison with the SCADA inferred wind speed can also help to better understand and quantify the effect related to the uncertainties of the extrapolation and the SAR measurement itself. For this study, images from Sentinel 1 A-B operating in IW mode were used. The nominal resolution of this sensor, operating in C-band, for this acquisition mode spans around 10-5 m per pixel spacing. Other satellites operating in X-band such as Terra-SAR X [53] or the ones belonging the Strix [11], [41] constellation might provide acquisitions at a higher resolution around 3 m per pixel. The application of the recalibration procedure to the extrapolated wind speed derived from these higher resolution images, is expected to provide overall more accurate hub-height wind maps.

Chapter 4

General conclusions and outlook of future work

This PhD thesis investigates the use of SCADA operational turbine data for the observation of wind field distributions at different spatial and temporal scales, both around individual turbines and across entire wind farms. By analyzing the turbines responses, single machines and whole plants are effectively transformed into extended wind sensors, capable of reconstructing the flow conditions that drive the observed operational trends—without potentially requiring the additional costs typically associated with external measurement devices, such as LiDARs. The possible applications of the proposed methodologies cover different areas of the wind energy sector, including short-term forecasting, site assessment, and wind farm control and monitoring.

On "turbine size" scales, the key innovation of this research activity is the use of wind speed measurements from a wind observer [24], based solely on operative wind turbine data, to augment the prediction of an engineering wake model [33]. The data-driven "closed loop" reformulation of the model was tested in a layout of two turbines and its performance were evaluated in terms of displacement of the wake centerline and the predicted background wind speeds at the rotor of the weaked-turbine. A comparison of the results with the trends derived from a high-fidelity simulation, considered as a reference ground truth, showed an improved agreement in the predictions of the corrected model compared to the open loop baseline version. This study highlighted the potential application of the information contained in the SCADA operative data to reconstruct the propagation of the flow in intra-turbine interactions. Using the wind observer model developed by [24], the wind turbine is effectively turned into an anemometer, which from the recorded operative data is able to provide a measurement of the wind speed over the rotor, without potentially requiring external additional devices.

It also shows how operational data can support the development of cost-effective data-driven models for potential deployment in wind farm control and monitoring, aimed at reducing loads and enhancing power output.

At the mesoscale- "wind farm size" level, this thesis presents the first study that leverages operational turbine data to correct extrapolated SAR wind speeds. Satellite wind maps provide snapshots of the wind fields developing over large offshore areas and are commonly used for pre-site assessment activities [64] or for investigating mesoscale phenomena such as coastal gradients and cluster wakes [66]. However, satellite acquisitions are typically available at an elevation of about 10 m above sea level (m.a.s.l.); consequently, the wind speeds derived from SAR data must be extrapolated to hub height to obtain information relevant for wind energy applications. To address this challenge, a novel methodology has been developed and applied to an existing offshore wind farm. The method corrects hub-height extrapolations of SAR-derived wind speeds using only nacelle-based measurements from the turbines. Its performance was assessed against an independent dataset of co-located SCADA and SAR wind speeds, showing improved accuracy compared to conventional wind profile corrections based on the Monin–Obukhov Similarity Theory (MOST). In this framework, the entire wind farm effectively acts as a distributed sensor network, providing in situ measurements that enable the correction of SAR-derived winds.

Further studies will be required to provide a more consistent validation of the findings reported in this thesis and improve the proposed approaches. On the wind turbine scale, the new closed-loop model proposed in [33], augmented with observer data, was tested on a layout of two aligned wind turbines. Although the results show an improvement in the prediction of wake properties for the analyzed scenario, further steps are required to assess the feasibility of implementing the proposed model for wind farm control applications in realistic conditions. In particular, a detailed evaluation of the benefits in terms of energy yield and fatigue load reduction, which represent critical aspects for control applications, should be carried out.

Moreover, the applicability of the model should be tested under different environmental conditions (e.g., different turbulence intensity and wind speed corresponding to different turbine operating regimes) and in more complex layouts, also considering yaw-misaligned configurations typically used in wake steering control. An assessment of the computational cost of implementing the EnKF with SEWS measurements is also necessary, starting from this simple setups, such the one analyzed, and extending to larger wind farms, while accounting for the increasing number of turbines and the associated time required for tuning the filter.

As noted, the model has so far been tested in a simulation environment. A field evaluation of the closed-loop FLODIRDyn reformulation should therefore be performed to assess its performance in real-case scenarios and to compare it with alternative control algorithms (e.g., LiDAR-assisted control) [64]. Such an analysis should also consider the quality of SCADA data, which can be incomplete (e.g., due to disconnections of the turbines from the grid) or affected by noise. Finally, another critical aspect to address is the loss of observability that may occur due to wake steering or wake meandering, as shown in the analyzed case. The occurrence of such effects, their impact on overall model performance, and possible mitigation strategies should be investigated in future work.

On a mesoscale level instead, a completely new approach based on a curve-fitting of the residuals among co-located SAR-SCADA data was introduced to recalibrate the satellite winds. Therefore, this methodology represents a preliminary step towards the developing ofa straightforward extrapolation approach for wind farm operators, that rely solely on turbine operational data, whether nacelle wind speeds or rotor-equivalent wind speeds (REWS) estimated from turbine power curves and

SAR imagery—such as those freely provided by space missions like Copernicus—for site assessment activities. More advanced techniques, incorporating machine learning techniques or wind observer models, could be introduced in the future to enhance recalibration accuracy and to improve understanding of the underlying causes behind the observed trends in the dataset under varying atmospheric conditions.

The wind observer model developed by [24] provides an estimation of the shear over the rotor area and can serve as a wake detection tool. In the context of satellite data recalibration, observer-derived shear profiles could be used to infer atmospheric stability conditions at the time of satellite acquisition. Additionally, given its capability as a wake detector, the observer model might offer unique insights into the wake deficit profiles induced by cluster wakes. This supplementary information would be highly beneficial for improving the extrapolation of satellite wind speeds.

Furthermore, as previously mentioned, the recalibration procedure based on SCADA data was tested only at a single wind farm. More extensive validation across different sites and using a larger dataset is required to assess whether the observed trends in the velocity residuals between SAR and SCADA data can be generalized or if each site exhibits a specific distribution. A comparison with alternative site measurements, such as those provided by LiDARs or met masts, if available, would provide an independent source to evaluate the reliability of the proposed recalibration methodology.

Appendix A

Engineering wake models

A.1 Engineering wake models: state of art

This section presents a state-of-the-art review of engineering wake models commonly used to describe wake propagation, with a particular emphasis on the FLORIDyn framework, which has been investigated as part of this PhD research in **Section 2.2**. The Parametric steady-state models are the ones describing the mean behavior of the wind field with parametrized analytical expressions rather than differential equations. These "engineering " wake models can be divided into two main categories:

1. empirical models,
2. analytical models

Empirical models have been used to mainly estimate the variation of the wake-centre velocity deficit with the streamwise distance from the turbine rotor [65]. Their formulations are obtained basically by fitting numerical or experimental data.

On the other hand, analytical models are derived based on flow-governing equations and, therefore, have a superior ability to capture the physics of the flow propagation, even though, their predictions can be improved using operational data of the turbines, following a "data-driven" approach, as it will be described later in the following chapter. One of the earliest analytical parametric wake models was introduced by Jensen [45]. The model is derived by applying mass conservation to a control volume downstream of the turbine, and by using the Betz theory to relate the wind speed just behind the rotor to the turbine thrust coefficient C_T. The wake velocity deficit is assumed to have a uniform, top-hat profile, and the wake expands linearly with downstream distance (**FigureA.1**). The normalized velocity deficit based on this model is given by:

$$\frac{\Delta\bar{u}}{\bar{u}_\infty} = 1 - \sqrt{1 - C_T}\left(1 + 2k_t\frac{x}{D}\right)^{-2} \tag{A.1}$$

where $\bar{u}_\infty$ is the mean incoming wind speed, $\Delta\bar{u} = \bar{u}_\infty - \bar{u}$ is the mean velocity deficit, k_t is the wake expansion rate, x is the downstream distance from the rotor, and D is the rotor diameter.

However, due to the top-hat assumption, this model tends to underestimate the velocity deficit at the wake center and overestimate it at the edges. Additionally, it

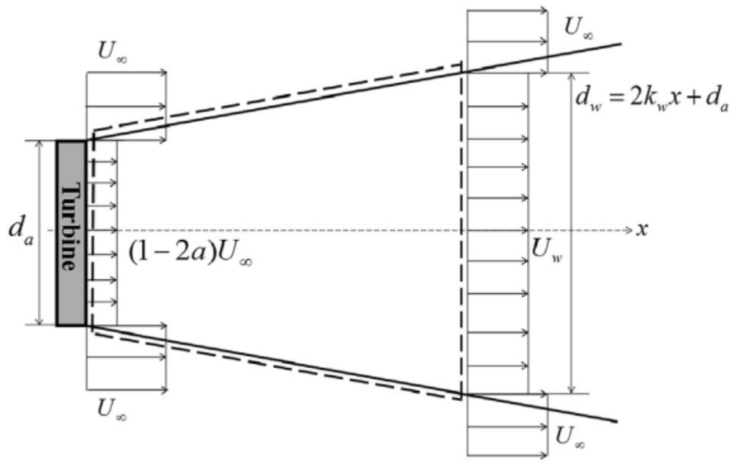

Figure A.1. Jensen's single wake model [45].

makes the power prediction of downstream turbines overly sensitive to their lateral positioning [65].

To address these limitations, [12] proposed a Gaussian wake model, which better represents the velocity deficit profiles observed in wind tunnel measurements and large-eddy simulations (LES). In this formulation, the normalized velocity deficit is expressed as:

$$\frac{\Delta \bar{u}}{\bar{u}_\infty} = C(x) \exp\left(-\frac{r^2}{2\sigma^2}\right) \tag{A.2}$$

where r is the radial distance from the wake center and σ is the standard deviation of the Gaussian distribution, corresponding to the wake width. The wake width is modeled as growing linearly with downstream distance:

$$\frac{\sigma}{D} = k\frac{x}{D} + \epsilon \tag{A.3}$$

where k is the wake growth rate and $\epsilon = 0.2\sqrt{\beta}$ is the initial normalized wake width, with β representing the shape parameter of the inflow boundary layer. The model satisfies mass and momentum conservation in an integral form:

$$T = \frac{\pi D^2}{8}\rho C_T \bar{u}_\infty^2 = \rho \int \bar{u}(\bar{u}_\infty - \bar{u})\, dA \tag{A.4}$$

where T is the turbine thrust force and ρ is the air density.

The original formulation assumed isotropic wake expansion. However, ground proximity and atmospheric stratification affect vertical and lateral wake development differently. Therefore, a generalized version model has been introduced, distinguishing the lateral and vertical wake widths:

$$\frac{\sigma_y}{D} = k_y \frac{x}{D} + \epsilon \tag{A.5}$$
$$\frac{\sigma_z}{D} = k_z \frac{x}{D} + \epsilon \tag{A.6}$$

where σ_y and σ_z are the lateral and vertical standard deviations, respectively, and k_y, k_z are the corresponding wake growth rates.

The growth rates k, k_y, k_z are key parameters of the model and depend on the turbulence intensity (TI) of the incoming flow. For example, based on wind tunnel data in [13], a typical value of k is 0.022 under moderate turbulence conditions.

A different steady-state model was developed by combining the Jensen model with a wake deflection formulation accounting for turbine yaw, known as the FLORIS (FLOwRedirection and Induction in Steady-state) model [39].

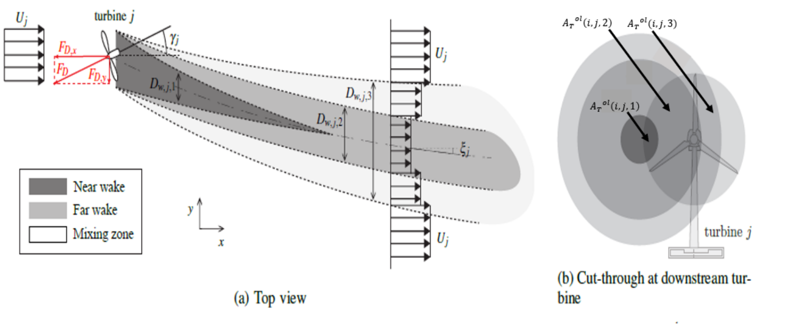

Figure A.2. (a) The zones of the parametric wake model FLORIS. (b) Definition of the wake areas overlapping with a downstream turbine [37].

FigureA.2 reports the description of the wake within the FLORIS model. The model divides the wake into three distinct zones: the near-wake ($q = 1$), far-wake ($q = 2$), and mixing-wake ($q = 3$). Similar to the Jensen's model, each wake zone expands proportionally with downstream distance x. The wind velocity in the wake is considered uniform in the lateral direction, but each region is characterized by its own expansion factor (see Figure). The diameter of the wake generated by turbine j in zone q is given by:

$$D_{w,j,q}(x) = \max\left(D_T(j) + 2k_e m_{e,q} x, 0\right), \tag{A.7}$$

where $D_T(j)$ is the rotor diameter of turbine j ($j \in T$),with $T = (1, 2, .., N)$ referring to the set of N turbines in a generic wind farm , and k_e, $m_{e,q}$ are empirical expansion coefficients for each wake region.

In this model, the velocity deficit in the three wake zones decays quadratically with the distance from the rotor, rather than being directly related to the wake expansion. For a single wake case, the velocity profile in the wake behind the turbine j is expressed as:

$$U_{w,j}(x, r) = U_T(j)\left[1 - 2a_T(j)c_j(x, r)\right], \tag{A.8}$$

where x and r represent the axial and radial distances from the wake centerline, respectively. Here, $U_T(j)$ denotes the free-stream wind speed in front of turbine j, and $a_T(j)$ is its axial induction factor. The decay function $c_j(x,r)$ is defined piecewise as follows:

$$c_j(x,r) = \begin{cases} c_{j,1}(x) & \text{if } r \leq D_{w,j,1}(x)/2 \\ c_{j,2}(x) & \text{if } D_{w,j,1}(x)/2 < r \leq D_{w,j,2}(x)/2 \\ c_{j,3}(x) & \text{if } D_{w,j,2}(x)/2 < r \leq D_{w,j,3}(x)/2 \\ 0 & \text{otherwise} \end{cases} \tag{A.9}$$

with the local wake decay coefficient for each zone given by:

$$c_{j,q}(x) = \left(\frac{D_T(j)}{D_T(j) + 2k_e m_{U,q}(\gamma_T(j)x} \right)^2, \tag{A.10}$$

the wake decay rates were adjusted for the rotor yaw angle ($\gamma_T(j)$) empirically by deriving the following relationship between $m_{U,q}$ and $\gamma_T(j)$:

$$m_{U,q}(\gamma_j) = \frac{M_{U,q}}{\cos(\alpha_U + \beta_U \gamma_j)}. \tag{A.11}$$

where $M_{U,q}$ are zone-specific baseline recovery parameters for $q = 1, 2, 3$, and β_U, α_U are empirical tuning parameters determining the sensitivity of recovery to yaw misalignment.

The model described in **Equation A.8** estimates the velocity deficits in the wake with respect to a given free-stream inflow speed.

As pointed out in [37], it is generally not possible to assume that the free-stream inflow velocity into the wind plant is known. However, it is possible to estimate the effective wind speeds at the front-row turbines using turbine power output and yaw angle measurements. This estimated value can be assumed as the *effective inflow speed.*

Subsequently, the wind speeds at downstream turbines are estimated by accounting for the cumulative effect of upstream wakes. This is done by weighting the wake contributions according to their overlap with the downstream rotor areas, using the root-sum-square method proposed in [47].

Therefore, at each turbine location, the effective wind speed experienced by the rotor is estimated differently for freestream turbines ($\mathcal{F} \subset \mathcal{T}$) and for those affected by wake interactions ($\mathcal{D} \subset \mathcal{T}$), where $\mathcal{F}$ and $\mathcal{D}$ denote the subsets of freestream and waked turbines, respectively.

For turbines operating in freestream conditions, the effective wind speed is inferred from the power production $P_T(j)$ equation:

$$U_T(j) = \left(\frac{2P_T(j)}{\rho A_T(j) C_P(a_T(j), \gamma_T(j))} \right)^{1/3}, \quad \forall j \in \mathcal{F}, \tag{A.12}$$

where ρ is the air density, $A_T(j)$ is the rotor swept area, C_P is the power coefficient, $a_T(j)$ is the axial induction factor, and $\gamma_T(j)$ is the yaw misalignment angle of turbine j. Further details on the derivation of the relationship between the power coefficient C_P, the axial induction factor $a_T(j)$, and the yaw angle $\gamma_T(j)$ can be found in [37], [39]. For downstream turbines affected by wake interactions, *effective inflow speed* is estimated using a root-sum-square approach to account for the combined influence of multiple upstream wakes:

$$U_T(j) = U_T(\tilde{i}(j)) \cdot X(j) \quad \forall j \in \mathcal{D}, \tag{A.13}$$

where $U_T(\tilde{i}(j))$ denotes the inflow effective wind speed at the rotor of turbine $\tilde{i}(j)$—a turbine belonging to the set of freestream machines ($i \in \mathcal{F}$), identified as described in [37]—whose wake impinges on turbine j (**Figure A.2**). The term $X(j)$ represents a wake interaction factor accounting for the cumulative effects of wakes originating from all upstream turbines.

$$X(j) = 1 - 2\sqrt{\sum_{i\in\mathcal{T}\,:\,x_i<x_j} \left[a_T(i) \sum_{q=1}^{3} c_{i,q}(x_j - x_i) \cdot \min\left(\frac{A^{\mathrm{ol}}(i,j,q)}{A_T(j)}, 1 \right) \right]^2}, \tag{A.14}$$

where $A^{\mathrm{ol}}(i,j,q)$ represents the overlap area between the wake zone q of turbine i and the rotor of turbine j (with area $A_T(j)$), and x_i and x_j are the positions of the turbines along the wind direction. $c_{i,q}$ represents the decay function relative to the wake zone q of turbine i .The overlapping areas are computed from the wake centerline and wake diameter estimations—derived using basic geometry as explained in [37].

The model describes the compressive wake deflection (always referring to the wake generated by the generic turbine j) as follows:

$$y_{w,j}(x) = y_{w,\mathrm{yaw},j}(x) + y_{w,\mathrm{rot},j}(x) \tag{A.15}$$

the first term describes the contribution of the turbine rotor yaw to the deflection of the wake. In this scenario, the change in the angular setting of the rotor introduces a later component into the thrust force that the rotor exerts on the flow F_D. As a result the wind flow is deflected in the opposite direction of the yaw rotation. Because the thrust force induces the wake deflection, the yaw deflection is a function of the thrust coefficient of the turbine $C_T(j) = 2F_D(j)/(\rho A_T(j)U_T(j)^2)$. The second term accounts for a small lateral wake deflection that has been observed in experiments even when the turbines are not yawed. This deflection results from the combined effects of vertical shear in the atmospheric boundary layer and wake rotation. When the rotor rotates clockwise, the lower part of the boundary layer—characterized by slower wind speeds—is deflected upward and to the right, while the faster flow in the upper part is deflected downward and to the left. As a result, the overall wake is shifted to the right. A more detailed description regarding the implementation of wake deflection in FLORIS can be found in [37], [39]. The parameters of the model for wake deflection, expansion, and decay are calibrated using turbine power data. A game-theoretic approach has been employed to optimize the yaw settings of turbines within a wind farm based on this simplified model, and the results have been validated through high-fidelity SOWFA simulations [57], [37], [39].

These low-cost and computationally efficient wake models have enabled the development of model-based, data-driven control algorithms. Such algorithms have demonstrated the potential to enhance the total power output of the wind farm in both high-fidelity simulations and field experiments. Different modifications and updates of the baseline zone FLORIS model have been proposed in the literature. An exhaustive bibliography covering the current advancements and various reformulations of the model can be found in [14].

However, the model provides a steady-state representation of the wake and does not capture the dynamic evolution of the downstream flow field. In reality, the flow does not instantaneously adjust to changes in turbine control settings; instead, the effects propagate downstream with a delay, depending on the spatially and temporally varying velocity field in the wake.

This limitation becomes particularly critical for control applications in large-scale wind farms and in scenarios where fast dynamics must be captured, such as those involving rapid control updates or short-term forecasting.

Further studies focused on the development of low-computational-cost dynamic parametric wake models, aimed at more accurately capturing wake behavior over shorter timescales and during changes in turbine or environmental states. Different low- to medium-fidelity dynamic models have been proposed for this purpose. The most prominent among these is the *Dynamic Wake Meandering* (DWM) model, in which the wake centerline fluctuations are described by modeling the wake as a passive tracer displaced by large-scale eddies [52]. Since its introduction, several versions of the DWM model have been developed, with recent extensions incorporating atmospheric stability effects and structural load coupling in the FAST.Farm implementation [46]. Validation against LiDAR measurements has shown good agreement, particularly in terms of predicted wake center positions. Additional studies have also refined wake advection and expansion rates [65].

Another dynamic model is an extension of the aforementioned steady-state FLORIS wake model [38]. In the first formulation of this dynamic variant, each of the three wake zones is further split into left and right regions, and an additional freestream zone is included, resulting in a total of seven distinct zones—each with individual expansion factors (**Figure A.3**).

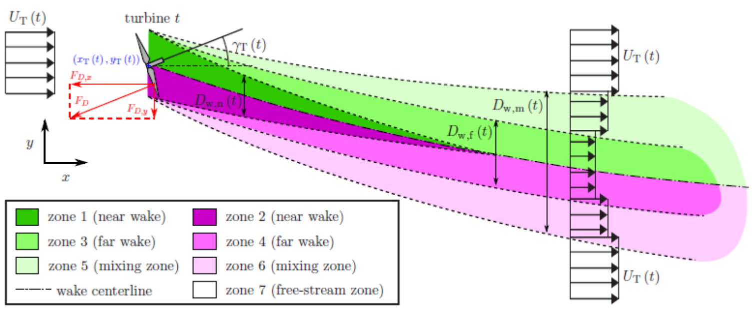

Figure A.3. The different wake zones in the zone FLORDyn model [38]

The dynamics of the wake are captured via the propagation of OPs, which represent air masses moving downstream in a Lagrangian framework. These OPs originate at the turbine rotor planes and carry in their motion, key operating information such as the yaw misalignment γ_T, the axial induction factor a_T, and the hub-height freestream velocity U_T (**Figure A.4**). These quantities determine wake characteristics in terms of shape, velocity deficit, and deflection. Therefore, changes in these variables "travel" downstream with the OPs at discrete time steps, providing a simplified yet dynamic representation of wake behavior.

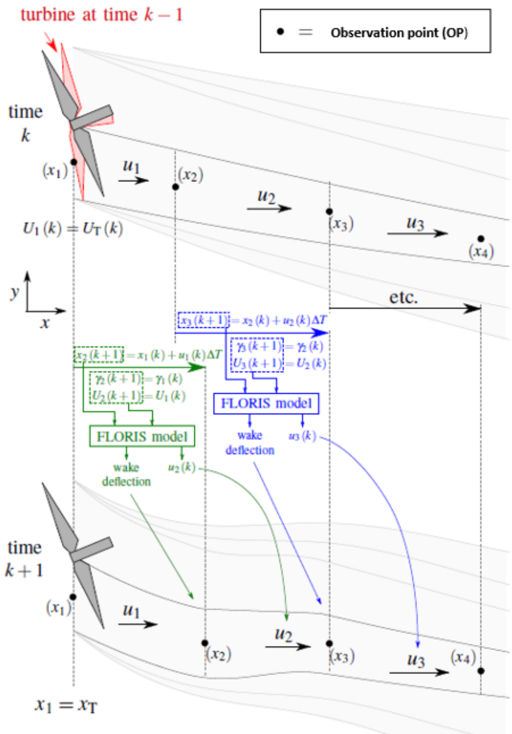

Figure A.4. State update mechanism in the FLORIDyn model [38].

This approach, following the wake zone framework of FLORIS, captures the delay in the propagation of wake-induced effects on downstream turbines. For example, a change in yaw misalignment or induction factor at an upstream turbine affects the downstream flow only after a certain number of time steps, modeling the physical delay with which the wake evolves and influences other turbines. This mechanism allows FLORIDyn to model delayed wake propagation, addressing one of the main limitations of steady-state models.

For a given wind direction , freestream velocities $U_T(j, k)$ at front turbines ($\forall j \in \mathcal{F}$) —those not affected by upstream wakes— provide the input source to the FLORIDyn model. These velocities can be estimated at a given time instant k from measurements of power, induction, and yaw at these turbines, by inverting the steady-state power equation as it was done in **Equation A.12**:

$$U_T(j, k) = \left(\frac{2P_T(j, k)}{\rho A_T(j, k) C_P(a_T(j, k), \gamma_T(j, k))} \right)^{1/3}, \quad \forall j \in \mathcal{F}, \tag{A.16}$$

the terms are the same as in **Equation A.12**, the only difference is the additional time variable k.

For turbines in freestream, the rotor effective wind speed is assumed to be equal to the freestream velocity.

$$u_T(j,k) = U_T(j,k) \quad \forall j \in \mathcal{F}, \tag{A.17}$$

By tuning yaw and induction settings at the front turbines, the model allows modification of the wake impact on downstream turbines. These dynamics are particularly important in control strategies for wind plants with large spatial extent or those requiring response over short time windows.

Defining N_p as the number of OPs representing a given wake zone z of a generic turbine t, the dynamic of the wake is expressed according to the following state-space representation of the OPs propagation:

$$\begin{aligned}
\begin{bmatrix} x_{t,z,1,k+1} \\ \vdots \\ x_{t,z,N_P,k+1} \end{bmatrix} &= \underbrace{\begin{bmatrix} 0 & 1 & \cdots & 0 \\ \vdots & \ddots & \ddots & \vdots \\ 0 & 0 & \cdots & 1 \\ 0 & 0 & \cdots & 0 \end{bmatrix}}_{A} \begin{bmatrix} x_{t,z,1,k} \\ \vdots \\ x_{t,z,N_P,k} \end{bmatrix} \\
&+ \underbrace{\begin{bmatrix} 1 \\ 0 \\ \vdots \\ 0 \end{bmatrix}}_{B} x_T(t) + \Delta T A \begin{bmatrix} u_{t,z,1,k} \\ \vdots \\ u_{t,z,N_P,k} \end{bmatrix}, \quad \forall t \in \mathcal{T},\ z \in \{1, \dots, 7\}
\end{aligned} \tag{A.18}$$

where $x_{t,z,p,k}$ and $u_{t,z,p,k}$ are respectively the downwind position and the effective velocity of the OP p in a wake zone z of a generic turbine t at a timestep k. A is the state transition matrix that propagates the variable downstream and has a semi-diagonal form, while B is the input matrix that injects turbine-level values into the OP array, At each time step k, the axial distances between the OPs are updated according to the **Equation A.20**, assuming that the velocity between two OPs is constant over the downwind direction. ΔT represents the time interval between two discrete time steps k and $k+1$. With this formulation, the "measured" quantities are effectively passed downstream within a given wake zone. As a result, the delay in the propagation of the wake effects induced by changes in these variables at the rotor is modeled in a discretized time framework. For example, the effects on the wake of a change in yaw are observed after one timestep at the OP in position x_2,after two-time steps at the OP in position x_3, and so on. The same delayed behavior applies to changes in the rotor axial induction and the free-stream velocity. The free-stream velocity, axial induction factor, and yaw angle at OP p in zone z of turbine t at time step k are denoted respectively as $U_{t,z,p,k}$, $a_{t,z,p,k}$, and $\gamma_{t,z,p,k}$. The yaw and axial induction values are propagated in this way only through zones 1 to 6, since by definition, the free-stream flow is not affected by the axial inductions and yaw angles of turbines. Using a similar vector notation as above, the update laws are expressed as:

$$\begin{bmatrix} U_{t,z,1,k+1} \\ U_{t,z,2,k+1} \\ \vdots \\ U_{t,z,N_p,k+1} \end{bmatrix} = A \begin{bmatrix} U_{t,z,1,k} \\ U_{t,z,2,k} \\ \vdots \\ U_{t,z,N_p,k} \end{bmatrix} + BU_T(t,k), \quad \forall t \in \mathcal{T},\ z \in \{1,\ldots,7\}, \tag{A.19}$$

$$\begin{bmatrix} \gamma_{t,z,1,k+1} \\ \gamma_{t,z,2,k+1} \\ \vdots \\ \gamma_{t,z,N_p,k+1} \end{bmatrix} = A \begin{bmatrix} \gamma_{t,z,1,k} \\ \gamma_{t,z,2,k} \\ \vdots \\ \gamma_{t,z,N_p,k} \end{bmatrix} + B\gamma_T(t,k), \quad \forall t \in \mathcal{T},\ z \in \{1,\ldots,6\}, \tag{A.20}$$

and similarly for the axial induction, with the state matrix A and B as in **Equation A.19** and **Equation A.20**.

From the effectively delayed yaw angle $\gamma_{t,z,p}$ and axial induction $a_{t,z,p}$ at an OP p in wake zone z of turbine t, the deflection and expansion of that wake zone can be determined. Specifically, the crosswind position of the center of the total wake at OP p, denoted as $y_{C,t,z,p}$, is calculated as:

$$y_{C,t,z,p} = y_T(t) + y_{\mathrm{w,rotation}}(x_{t,z,p}) + y_{\mathrm{w,yaw}}(x_{t,z,p},\ \gamma_{t,z,p},\ a_{t,z,p},\ D_T(t)) \tag{A.21}$$

In this initial formulation of the model, the OPs are assumed to move with the effective wind speed they represent. At each time step k, the effective velocity of an OP is computed by subtracting from the free-stream velocity a reduction factor. This reduction factor depends on the "delayed" turbine control inputs—such as yaw angle and axial induction—as well as the OP's downwind distance from the turbine, and thus on the specific wake zone in which the OP is located.

Following the Jensen model [45], the velocity deficit in the far wake is assumed to decay quadratically with the expansion of the wake, as for the steady state FLORIS zone model, but considering 7 distinct regions instead of 3. In contrast, within the near-wake region, a velocity correction factor based on an arctangent function is applied [38].

The normalized velocity deficit at an OP $p \in \{1,\ldots,N_p\}$, located within wake zone z of a single turbine t, is given by:

$$r_{t,z,p} = 2a_{t,z,p}\left[\frac{1}{2} + \tan^{-1}\left(\frac{2x_{t,z,p}}{D_T(t)}\right)\right]\left[\frac{D_T(t)}{D_T(t) + 2k_e m_{U,z}(\gamma_{t,z,p})x_{t,z,p}}\right]^2, \tag{A.22}$$

where $D_T(t)$ is the rotor diameter of the turbine t, k_e is a wake expansion parameter, $m_{U,z}(\gamma_{t,z,p})$ is the zone-specific velocity recovery coefficient defined as in **Equation A.11**. The effective wind speed at the OP p in the wake of a single turbine t, is then obtained from:

$$u_{t,z,p} = U_{t,z,p}(1 - r_{t,z,p}), \tag{A.23}$$

where $U_{t,z,p}$ is the freestream velocity at the hub height of turbine t in wake zone z. The coefficients $m_{U,z}$ characterize how rapidly the wake velocity recovers to the ambient freestream velocity, depending on the distance from the turbine and the specific wake zone, as previously explained.

When the wakes of multiple turbines overlap at a given OP, the associated velocity reduction factors from each contributing turbine are combined using an interpolation scheme, as illustrated in **Figure A.5**. Specifically, the reduction factors from the two OPs nearest in the upwind and downwind directions within the wake zone $\tilde{z}$ of another turbine $\tilde{t}$ are interpolated [38].

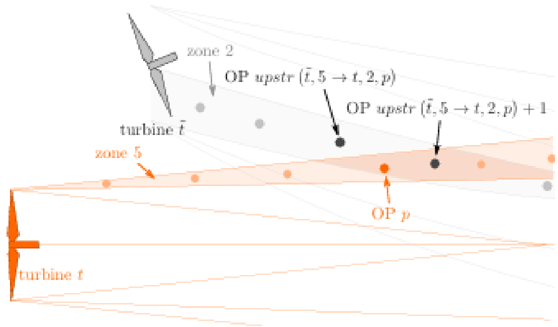

Figure A.5. Upstream and downstream OP in an overlapping wake [38]

.

The resulting interpolated reduction factor at the OP p, located in wake zone z of turbine t, due to wake zone $\tilde{z}$ of turbine $\tilde{t}$, is denoted as $r(\tilde{t}, \tilde{z} \to t, z, p)$.

The final reduction in free-stream velocity at the OP location is then obtained by combining the interpolated reduction factors from all overlapping wakes to compute the effective wind speed at that OP, as given by:

$$u_{t,z,p} = U_{t,z,p} \prod_{(\tilde{t},\tilde{z}) \in \mathcal{O}_{t,z,p}} \left(1 - r(\tilde{t}, \tilde{z} \to t, z, p)\right) \tag{A.24}$$

Then, the effective wind speeds at the downstream turbines are estimated by combining the effects of the wakes on the free-stream velocities.

First, an interpolation function is used to map the set of delayed free-stream velocities U from each wake zone $\tilde{z}$ of upstream turbines $\tilde{t}$ to the rotor plane of the downstream turbine t. Since OPs with index $p = 1$ are always located at the rotor plane, the interpolated velocity $U(\tilde{t}, \tilde{z} \to t)$ is computed as:

$$U(\tilde{t}, \tilde{z} \to t) = \texttt{fint}(U; \tilde{t}, \tilde{z} \to t, 1, 1), \tag{A.25}$$

where `fint` is the same interpolation function applied between OPs.

To compute the resulting effective free-stream velocity for each downstream turbine $t \in \mathcal{D}$, the delayed free-stream velocities of the upstream wake zones are weighted by their overlap areas with the turbine rotor t. The area of overlap between wake zone $\tilde{z}$ of turbine $\tilde{t}$ and the rotor of turbine t is denoted by $A^{\mathrm{ol}}(\tilde{t}, \tilde{z} \to t)$. The portion of the rotor not affected by any wake, with area $A^{\mathrm{noOl}}(t)$, is assumed to experience the delayed free-stream velocity from zone 7 of the upstream turbine closest in the crosswind direction to turbine t.

$$\begin{aligned} U_T(t) = &\sum_{\tilde{t}\in\mathcal{P}:x_T(\tilde{t})<x_T(t)} \sum_{\tilde{z}=1}^{6} \left[\frac{A^{\mathrm{ol}}(\tilde{t},\tilde{z}\to t)}{A_T(t)} \cdot U(\tilde{t},\tilde{z}\to t) \right] \\ &+ \frac{A^{\mathrm{noOl}}(t)}{A_T(t)} \cdot U(\mathrm{closest}(t), 7 \to t), \quad \forall t \in \mathcal{D} \end{aligned} \tag{A.26}$$

Using interpolation and root-sum-square weighting by overlap area, the effective reduction factor at turbine t, denoted $r_T(t)$, is computed as:

$$r_T(t) = \sqrt{\sum_{\tilde{t}\in\mathcal{P}:x_T(\tilde{t})<x_T(t)} \left[\sum_{\tilde{z}=1}^{6} \frac{A^{\mathrm{ol}}(\tilde{t},\tilde{z}\to t)}{A_T(t)} \cdot r(\tilde{t},\tilde{z}\to t) \right]^2}, \tag{A.27}$$

where the reduction factor for each wake zone is defined by:

$$r(\tilde{t},\tilde{z}\to t) = \mathtt{fint}(r;\tilde{t},\tilde{z}\to t,1,1). \tag{A.28}$$

Finally, the effective velocity at turbine t is given by:

$$u_T(t) = U_T(t)\left[1 - r_T(t)\right], \quad \forall t \in \mathcal{D}, \tag{A.29}$$

where $U_T(t)$ is the nominal free-stream velocity at the rotor of turbine t, and $u_T(t)$ is the corrected wind speed accounting for upstream wake interactions. These effective velocities $u_T(t)$ are then used to compute the power output of downstream turbines via the power equation:

$$P_T(t,k) = \frac{1}{2}\rho A_T(t) C_P(a_T(t,k),\gamma_T(t,k)) u_T^3(t,k), \quad \forall t \in D \tag{A.30}$$

To summarize, the FLORIDyn model extends a parametric wake model originally developed for steady-state conditions by introducing flow and advection dynamics. This extension enables the dynamic evolution of wake effects while retaining the computational efficiency of a steady-state wake formulation.

Nevertheless, the original version of the model presents several limitations. Due to its two-dimensional flow representation, it is unable to capture shear and veer effects that are significant in realistic atmospheric conditions. The model also assumes a single prevailing wind direction and does not incorporate turbulence [38], which limits its applicability in more complex or stochastic flow environments. Furthermore, because the OPs move with the local effective wind speed, overlapping wake regions may occur, potentially leading to inaccuracies in the wake representation.

Different reformulations of the original FLORIDyn zone model have been proposed to address its limitations, particularly regarding its two-dimensional formulation and lack of turbulence modeling. Among these, [17] introduced a *Gaussian FLORIS version* inspired by the Gaussian model of [13], re-designing the FLORIDyn layout into a form that incorporates heterogeneous and changing flow conditions, wind shear, and added turbulence levels. The Gaussian FLORIS model describes the wake in a three-dimensional framework with a Gaussian-shaped wind speed recovery. The calculation of wake-added turbulence is made according to the model proposed

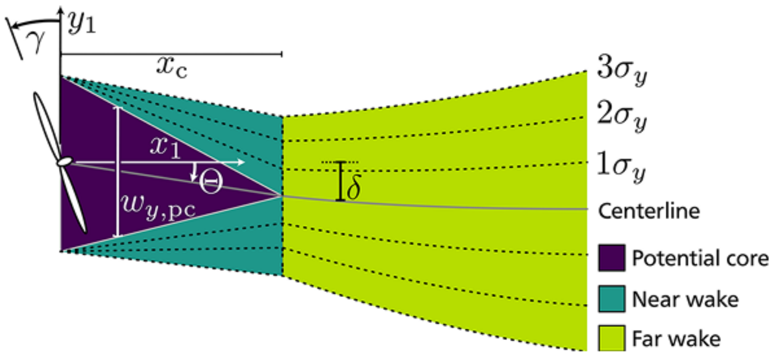

Figure A.6. The revised Gaussian FLORIDyn framework [17].

by [32].The wake is divided into three areas: the potential core, the near-wake area and the far-wake area (**Figure A.6**).

A reduction factor $r = \Delta u/u_{\text{free}}$ characterizes the wake, where Δu is the wind speed deficit and u_{free} is the undisturbed wind speed. The potential core is the region immediately behind the rotor plane. Within the potential core, r is constant. In the near- and far-field the wake deficit is characterized by a Gaussian shape and decays with the downstream distance following σ_y and σ_z in the respective crosswind directions. The potential core width is described by $w_{y,\text{pc}}$ and $w_{z,\text{pc}}$, which continuously decrease for the length of the potential core x_c. Lastly, the deflection δ represents the position of the wake centerline. These variables depend on the turbine states represented by the trusth coefficient C_T, the yaw angle γ, the ambient turbulence intensity I_0 and a set of 10 parameters related to the Gaussian model which regulate wake properties such as the recovery rate, the expansion rate and the influence of yaw angles.

This framework presents two different coordinate systems, the global and the wake reference one. In the wake coordinate system K_1 with (x_1, y_1, z_1), where x_1 describes the downwind direction,y_1 the horizontal crosswind direction and z_1 the vertical crosswind direction. The origin of this coordinate frame is at the rotor center. The other coordinate system is the world coordinate system K_0 with coordinates (x_0, y_0, z_0), whose coordinates are the longitudinal (x_0), latitudinal (y_0) and vertical (z_0) global ones. OPs are initialized on the rotor plane and propagate downstream. In order to provide a regular representation of the crosswind wake area for any number of OPs, an algorithm based on the sunflower distribution was used [80]. The algorithm returns a relative crosswind coordinate $\nu_y, \nu_z \in [-0.5, 0.5]$ for a given number of OPs at each time step. The position of an OP in the wake coordinate system, assuming here for semplicity, only an horizontal deflection of the wake, is given by:

$$y_{1,\text{OP}} = \nu_y \cdot (6\sigma_y + w_{y,\text{pc}}) + \delta \tag{A.31}$$

$$z_{1,\text{OP}} = \nu_z \cdot (6\sigma_z + w_{z,\text{pc}}) \tag{A.32}$$

Where σ_y represents $\sigma_{y,\text{nw}}$ for $0 < x_1 \leq x_c$, and $\sigma_{y,\text{fw}}$ for $x_1 > x_c$. The same definition applies to σ_z. OPs with the same relative coordinate follow each other and form what is called a chain. The number of chains is equal to the number of OPs created at each time.

OPs are created at the rotor plane and they interact with foreign (other turbines) wakes, therefore they can be used to estimate the effective wind speed for the power generation at downstream turbines. The area represented by each OP is determined by generating a Voronoi pattern as explained in [17]. The area of the resulting polygons is normalized by the rotor area and used as weight. All weights are stored in a weight vector $\mathbf{w}$ used in power calculation. During the simulation, the reduction factor of foreign wakes $r_{f,OP}$ on the OPs is calculated as for original FLORIDyn formulation **Equation A.24**. Also in this version, the OPs locate the closest up- and downstream OPs from the foreign wake and interpolate their reduction factor at its location (**Figure A.5**).

The reduction factors computed for each OP ($\forall i \in \{1, \ldots, n_{OP}\}$) are stored in a vector $\mathbf{r}_f = [\mathbf{r}_{f,1}, \ldots, \mathbf{r}_{f,n_{\mathrm{OP}}}]$ and used to evaluate the effective wind speed at a downstream rotor as follows:

$$u_{\mathrm{eff}} = \mathbf{w}^{\top}(\mathbf{r}_f \circ \mathbf{u}), \tag{A.33}$$

where $\circ$ denotes element-wise multiplication and $\mathbf{u}$ represents a vector of the free wind speeds at the locations of the OPs. An OP considers itself influenced by a foreign wake if the closest foreign OP is less than $\frac{1}{4}D$ away. This threshold is settled arbitrary to reduce the number of OPs for the interaction interpolation.

In this version of the model, the OPs are assumed to propagate at the speed of the free-stream wind rather than the effective wind speed in accordance with Taylor's frozen turbulence hypothesis. Therefore , the model framework doesn't require a description of overlapping wake areas since neighboring OPs travel at the same speed and follow the same state changes. Furthermore, as a consequence of the hypothesis that OPs are traveling at freestream speed, it is not necessary to evaluate the influence of foreign wakes on the single OP at every time step: only for OPs at the rotor plane of downstream turbines the effective wind speed, resulting from wake interactions, is computed according to **Equation A.33**, in order to estimate the power production. These model assumptions significantly decrease the computational cost of the simulation. As it was mentioned before, the Gaussian FLORIDyn model describes also the effect of wind directional changes on the wakes.The assumption of the model is that a variation in the wind direction only affects the wake orientation and that the wake structure and downstream evolution (as defined by the underlying FLORIDyn model) can be considered independent from the free-stream behavior: therefore the two different coordinate systems, the world coordinate system K_0 and the wake coordinate system K_1 can be used to describe the two effects independently. The changing free-flow conditions are described in K_0, whereas the wake properties are described in K_1. An OP links these two coordinate systems (**Figure A.7**). The underlying FLORIS model is described in K_1, where the origin is located in the center of the rotor plane. The downwind distance is denoted as x_1, y_1 describes the horizontal crosswind distance and z_1 describes the vertical one. K_0 does not have a special orientation apart from $z_0 = 0$ being the ground level and the z_0 axis pointing upwards. x_0 describes the west–east axis, and y_0 describes the south–north axis. To transform a location vector r_1, described in K_1 of a turbine with the rotor-center location t_0, into r_0 the rotational matrix R_{01} is used:

$$\mathbf{r}_0 = \begin{bmatrix} x_0 \\ y_0 \\ z_0 \end{bmatrix} = t_0 + \mathrm{R}_{01}(\varphi)\left(\begin{bmatrix} x_{0,T} \\ y_{0,T} \\ z_{0,T} \end{bmatrix} + \begin{bmatrix} \cos\varphi & -\sin\varphi & 0 \\ \sin\varphi & \cos\varphi & 0 \\ 0 & 0 & 1 \end{bmatrix}\begin{bmatrix} x_1 \\ y_1 \\ z_1 \end{bmatrix}\right) \tag{A.34}$$

This equation assumes a uniform wind direction φ at every location. Two location vectors are associated to each OP, $r_{0,OP}$ and $r_{1,OP}$, one for each coordinate system. The OP's position update and its reduction factor are computed in K_1. K_0 is used to calculate the wake interaction and to determine the wind speed, the wind direction, and the ambient turbulence intensity. At the OP's creation, $r_{1,OP}$ is determined by **Equation A.31** and **Equation A.32** for the crosswind coordinates; the downwind coordinate is set to 0. Its world location, $r_{0,OP}$, is then determined by **Equation A.34** with the wind direction $\varphi_{0,T}$ at the turbine location. To update the location of an OP from time step k to time step $k+1$, the propagation step is calculated first in K_1:

$$x_{1,\mathrm{OP}}(k+1) = x_{1,\mathrm{OP}}(k) + u_{\mathrm{OP}}\,\Delta t \tag{A.35}$$

where Δt is the time step duration and u_{OP} is the magnitude of the wind vector $u_{0,\mathrm{OP}}$ at the OP's location $r_{0,OP}$.Considering u_{OP} only to have non-zero components in the x_0 and y_0 direction. With $x_{1,\mathrm{OP}}(k+1)$, the new crosswind locations $y_{1,\mathrm{OP}}(k+1)$ and $z_{1,\mathrm{OP}}(k+1)$ can be calculated with the **Equation A.31** and **Equation A.32**, respectively. This way, the position of the OP is updated from $r_{1,\mathrm{OP}}(k)$ to $r_{1,\mathrm{OP}}(k+1)$ at $k+1$. $r_{0,\mathrm{OP}}(k+1)$ is evaluated translating the $r_{1,\mathrm{OP}}(k+1)$ into the global reference system K_0:

$$\mathbf{r}_{0,\mathrm{OP}}(k+1) = \mathbf{r}_{0,\mathrm{OP}}(k) + \mathbf{R}_{01}(\varphi_{0,\mathrm{OP}})(\mathbf{r}_{1,\mathrm{OP}}(k+1) - \mathbf{r}_{1,\mathrm{OP}}(k)) \tag{A.36}$$

where $\varphi_{0,\mathrm{OP}}$ is the individual wind direction at $\mathbf{r}_{0,\mathrm{OP}}(k)$. In this framework, each OP propagates on its own $\varphi_{0,\mathrm{OP}}$, and non-uniform wind directions can be simulated.

Figure A.7 shows the update of the OP step in the wake and world coordinate system. When the wind direction is constant (**Figure A.7, panels (a) and (b)**), the OP calculates its step in the wake coordinate system (dotted arrow) and updates its location vectors.

When wind direction changes (**Figure A.7, panels (c) and (d)**)r_0 and r_1 are not influenced by the changed wind direction: their magnitude and orientation remain the same in their respective coordinate systems; however, their orientation towards each other changes. In order to drive the FLORIDyn model, the wind field needs to be able to simulate heterogeneous, changing environmental conditions. The basic assumption is that measurements of the wind field variables are available at certain locations (e.g.s. satellite data, lidar measurements, met masts). The value of a measurement for the location of an OP is then interpolated between the measurements available. To reduce the computational effort of interpolation at every time step, a nearest neighbor interpolation (NNI) is adopted To get a sufficient resolution of the measurements to employ a NNI, the sparse measurements m are mapped to a dense mesurement grid points $\mathbf{m}_g$:

$$\mathbf{m}_g = M\mathbf{m}, \tag{A.37}$$

where the matrix M describes the mapping as explained in [17].

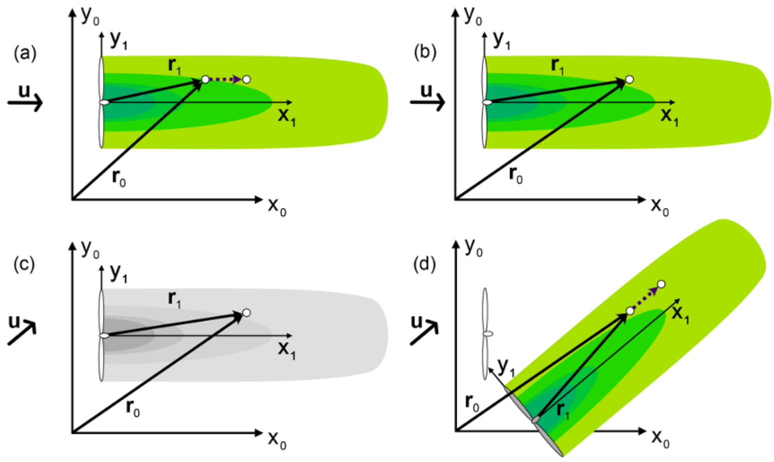

Figure A.7. (a), (b) Position update for a constant wind direction. (c), (d) Position updates for wind direction changes. The wake K_1 coordinate system is rotated to match the new downstream wind direction. This results in an apparent the apparent change in origin of the wake in the world coordinate system K_0, [17]

This FLORIDyn implementation is capable of simulating wakes under heterogeneous and time-varying flow conditions. The model was tested in various wind farm layouts and compared against high-fidelity SOWFA simulations [57]. The results show that the Gaussian FLORIDyn framework accurately predicts the timing of when the wake reaches the downstream turbines. However, since OPs do not propagate at the effective wind speed in this version of FLORIDyn, they arrive at the downstream turbine more abruptly, leading to discrepancies in both the wake magnitude and temporal evolution of its effects on turbine performance. Furthermore, while the Gaussian FLORIDyn model can keep the computational cost low, the simulation time grows exponentially and becomes unfeasible in model based control approaches for a wind farm with a large number of turbines. In order to tackle these issues, the framework of the model has been re-elaborated. Instead of generating multiple OPs to cover the entire wake, only one chain of points along the wake center-line is used to model the wake propagation [16]. The definition of a local wake K_1 and word reference system K_0 to describe the propagation of the wake and effect of changes in wind direction of the background field separately is still retained in the new reformulation.

For each turbine, a new OP is created every time step, while the oldest one is disregarded. Each OP carries three sets of states: the location of the OP, denoted as x_{OP}, the turbine state x_T and the wind field state x_{WF} , defined in a vectorial form as in [16]. The turbine state x_T represents all the turbine settings affecting the wake shape and magnitude, such as the yaw angle or the axial induction. The wind field state x_{WF} contains all the states necessary to propagate the wake and to calculate it. In this formulation, the free wind speed and the wind direction represent essential quantities for the wake description, but x_{WF} can also include the ambient turbulence intensity for instance. The downwind propagation step of the wake is always calculated in the wake coordinate system K_1, as described in

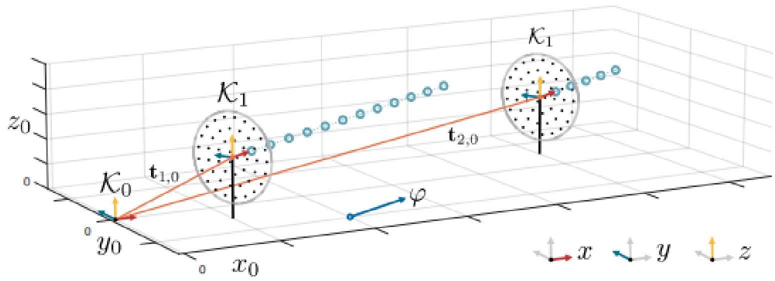

Figure A.8. Visualization of the FLORIDyn framework proposed in [16] with a single chain of OPs to describe the wake centerline. The global coordinate system K_0 and the two local systems K_1, corresponding to a two-turbine layout, are also shown in the figure. The turbine position vectors are denoted by $t_{1,0}$ and $t_{2,0}$, and the wind direction is indicated by the angle φ.

Equation A.35, and then translated into the world coordinate system K_0 as in **Equation A.36**. The key difference in this reformulation lies in reducing the wake description to a chain of OPs, which represents the evolution of the centerline.

In the original Gaussian framework the wake properties were estimated at a given location of the OPs or the turbines, via the nearest neighbor interpolation, given the high density of the OPs representing the wake. After the reduction in the number of points to a single chain and the consequent sparse description of the wake, this assumption doesn't lead anymore to sufficiently accurate results. A different extrapolation method has therefore been adopted:

for each turbine T_i, belonging to a group or a subgroup of turbines T ($T_i \in T$) in the plant, the two OPs (OP_1 and OP_2) in front and behind the closest point on the centerline of T_i to a generic location, defined as l_0 in K_0, are linearly interpolated, in such a way that the distance to l_0 is minimal (**Figure A.9**):

$$\mathbf{w} = \frac{\left(\mathbf{x}_{\mathrm{OP2,0}} - \mathbf{x}_{\mathrm{OP1,0}}\right)^\top \left(\mathbf{l}_0 - \mathbf{x}_{\mathrm{OP1,0}}\right)}{\left(\mathbf{x}_{\mathrm{OP2,0}} - \mathbf{x}_{\mathrm{OP1,0}}\right)^\top \left(\mathbf{x}_{\mathrm{OP2,0}} - \mathbf{x}_{\mathrm{OP1,0}}\right)} \tag{A.38}$$

which returns the weight $w \in [0, 1]$. The K_0 location of an OP^* is then given by:

$$\mathbf{x}_{\mathrm{OP^*,0}} = \mathbf{x}_{\mathrm{OP1,0}} + w\left(\mathbf{x}_{\mathrm{OP2,0}} - \mathbf{x}_{\mathrm{OP1,0}}\right) = (1 - w)\,\mathbf{x}_{\mathrm{OP1,0}} + w\,\mathbf{x}_{\mathrm{OP2,0}} \tag{A.39}$$

The other states $x^*_{OP,1}$, x^*_T and x^*_{WF} are also interpolated with the weight w following the same scheme as **Equation A.39**. Turbine states x^*_T, and wind field states x^*_{WF} derived from every turbine $T_i \in T$, in a spatial region near I_0, are therefore associated with the corresponding OP^*.

Successively, the position of l_0 in the wake system K_1 of the turbine T_i is defined by applying the inverted rotational matrix: $\mathbf{R_{01}^{-1}} = \mathbf{R}_{\mathbf{01}}^\top = \mathbf{R_{10}}$ to the distance vector $l_0 - x^*_{OP}$ (pointing from OP^* to l_0).

This vector is then added to the K_1 position of OP^*:

$$\boldsymbol{\ell}_{T_i,1} = \mathbf{x}_{\mathrm{OP^*,1}} + \mathbf{R}_{10}\left(\mathbf{l}_0 - \mathbf{x}_{\mathrm{OP^*,0}}\right) \tag{A.40}$$

As a result, $\boldsymbol{\ell}_{T_i,1}$ can be calculated for all turbines $T_i \in T$. The vector $\boldsymbol{\ell}_{T_i,1}$ stems from the origin of a third reference system K^*_1, the turbine coordinate system of T_i based on the states of OP^*.

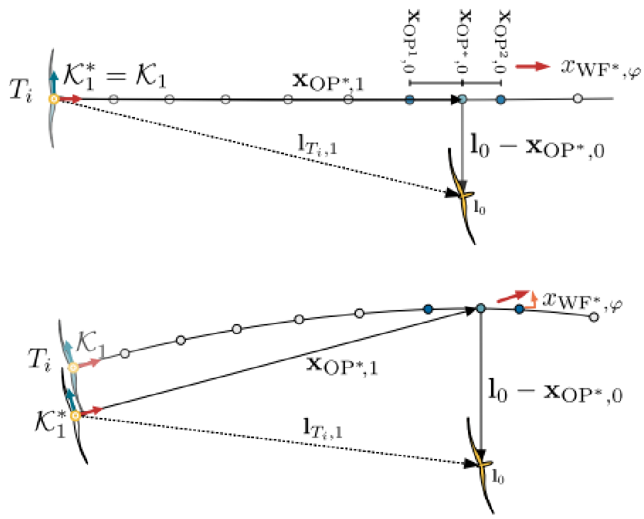

Figure A.9. Interpolation of the OP* and derivation of the position of I_0 [16].

As shown in (**Figure A.9**), in constant wind directions, the coordinate systems K_1 and K_1^* coincide. However, when the wind field states associated with OP$_1$ and OP$_2$ change due to a variation in the background free-stream wind direction, the reference origins of K_1 and K_1^* may temporarily differ in the global reference system K_0.

To describe the local wind field near a specific point of interest l_0, a new coordinate system K_2 is introduced. This system shares the same structure as K_1: the wind direction is aligned with the x_2 axis, y_2 is the crosswind direction, and z_2 points upward. For convenience, the origin of K_2 is defined such that its position in K_0 is $l_2 = [0, 0, l_{0,z}]^\top$, ensuring that $z_2 = 0$ corresponds to ground level, if elevation is neglected.

The definition of K_2 introduces the concept of the Temporary Wind Farm (TWF). The TWF represents a simplified, stationary, and local approximation of the wake and wind field conditions near l_0, constructed using the OP^* states associated with turbines $T_i \in T$, where T is a subset of the wind farm. The virtual positions of turbines in the TWF may differ from their actual real-world location, as perceived by the local OP^*.

The virtual positions of the turbines in K_2 are computed by inverting their position vectors from K_1:

$$t_{T_i,2} = l_2 - R_{21}(0) \cdot l_{T_i,1} \tag{A.41}$$

Since K_1 and K_2 share the same wind direction, the rotation matrix $R_{21}(0)$ reduces to the identity matrix.

While the turbine states are defined by their corresponding OP*, the wind field states in the TWF are not fully specified—only the wind direction is fixed. In practice, the wind field around l_0 is approximated by interpolating the wind states from the two nearest OP*, weighted by distance.

This construction results in a localized and homogeneous representation of the wind field, allowing the use of any steady-state wake model to evaluate the wake effects of T at l_2, effectively approximating their impact at l_0 [16].

The TWF enhances the modularity of the FLORIDyn framework. Unlike earlier implementations, where OP distributions were tightly coupled to the wake model (e.g., Gaussian or FLORIS zone models), the TWF allows decoupling of the OP propagation from the model structure. This enables the switching between different parametric wake models (e.g., Jensen, Gaussian-Porté-Agel, FLORIS zone) without modifying the underlying data structure.

Additionally, including multiple turbines in a TWF allows capturing of secondary wake steering effects, enabling robust evaluation of wake models in dynamic and heterogeneous atmospheric conditions.

An additional advantage of the Temporary Wind Farm (TWF) approach is its scalability in terms of computational load. By appropriately choosing the set T of turbines to include in the TWF, the number of interactions that must be evaluated can be limited. For instance, turbines that are far in the upwind or crosswind direction relative to l_0 and have negligible effects can also be excluded from T when evaluating the influence at a location l_0.

This selection criterion enables the decomposition of a large wind farm into multiple smaller, localized TWFs, each of which can be evaluated independently and in parallel, leading to a significant reduction in computational cost and, therefore, making dynamic real-time wind farm control with a large number of turbines more viable.

In addition, the framework simplifies the state architecture of the simulation by modeling turbines as sensors and actuators. Turbines provide local measurements and control inputs that feed into the generation and update of Operating Points (OPs). In turn, OPs serve as dynamic estimates of the intra-wind-farm flow field. Flow estimators can process turbine measurements and convert them into wind field metrics, which are then stored within the OP states. This modular design enhances the flexibility of FLORIDyn and supports integration with data-driven or estimation-based methods for flow reconstruction.

Alternative formulations of the FLORIDyn model, which describe only the dynamic of the wake centerline and use an engineering wake model to characterize the cross-wind profile of the wake, are available in the literature. The version used in this work of thesis is described in **Section 2.1**.

A.1.1 Kalman Filter-Based enhancement of wake models using SCADA data

This section provides an overview about the implementation of the Kalman filter [36] algorithm and its derivations to correct the predictions of dynaic wake models.

The focus of this paragraph will be in particular on the FLORIDyn model, whose application was also investigated during the PhD activity in a closed-loop reformulation of the version with two set of OPs modeling ambient and wake wind flow regimes. The state-space discretized description of the flow dynamics equations, which are the bulk of the FLORIDyn model formulation itself, are suitable for the implementation of a Kalman filter correction algorithm or its more complex reformulations. The first implementation of the closed-loop framework involved the original state-space representation of the FLORIDyn zone model [38], which was integrated with a Kalman filter using turbine measurements (electrical power output and control settings). In this formulation, the predicted velocity field from the wake model is corrected by adjusting the freestream velocities at various OPs.

More precisely, the relationship between the effective freestream velocities at the turbines and those at the OPs is defined by a time-varying mapping:

$$\vec{U}_{T,D}(k) = C_U(k)\vec{U}(k) \tag{A.42}$$

where $C_U(k)$ is a sparse, time-dependent matrix, $\vec{U}_{T,D}(k)$ is a vector stacking the effective freestream speeds at all downstream turbines $t \in D$ at time step k, and $\vec{U}(k)$ stacks the freestream velocities at each OP of the wind plant. The dynamic evolution of the wake velocities at each OP can be described in state-space form by the update **Equation A.19** :

$$\vec{U}(k+1) = A\vec{U}(k) + B_D\vec{U}_{T,D}(k) + B_F\vec{U}_{T,F}(k) + \vec{w}(k) \tag{A.43}$$

where A, B_D, and B_F are system matrices (typically assembled in block-diagonal form), and $\vec{w}(k)$ is a process noise vector capturing the effects of turbulence and model inaccuracies. Inputs $\vec{U}_{T,D}(k)$ and $\vec{U}_{T,F}(k)$ represent the effective freestream velocities at downstream and front turbines, respectively.

By substituting **Equation A.42** into **Equation A.43**, the system can be rewritten as:

$$\vec{U}(k+1) = \tilde{A}(k)\vec{U}(k) + B_F\vec{U}_{T,F}(k) + \vec{w}(k) \tag{A.44}$$

with $\tilde{A}(k) = A + B_D C_U(k)$.

To link model predictions to available measurements, the effective turbine velocities reconstructed from data (power, yaw angle, and axial induction factor) are expressed as:

$$\vec{u}_{T,D}(k) = C_u(k)\vec{U}(k) + \vec{v}(k) \tag{A.45}$$

Here, $C_u(k)$ is a time-varying output matrix, and $\vec{v}(k)$ denotes measurement noise. Effective velocities at turbines are estimated by inverting the turbine power equation (**Equation A.30**).

These estimates form the vector $\vec{u}_{T,D}(k)$, which serves as input to a conventional Kalman filter performing one-step-ahead predictions using the state equation **Equation A.44** and output equation **Equation A.45**.

The corrected state update becomes:

$$\vec{U}(k+1) = \tilde{A}(k)\vec{U}(k) + B_F\vec{U}_{T,F}(k) + K(k)\left[\vec{u}_{T,D}(k) - \hat{\vec{u}}_{T,D}(k)\right] \tag{A.46}$$

where $K(k)$ is the Kalman gain, and $\hat{\vec{u}}_{T,D}(k)$ is the model prediction of turbine-effective velocities.

The Kalman gain is updated at each step as:

$$K(k) = \tilde{A}(k)P(k|k-1)C_u(k)^T \left[R + C_u(k)P(k|k-1)C_u(k)^T\right]^{-1} \tag{A.47}$$

The error covariance update follows:

$$P(k+1|k) = \tilde{A}(k)P(k|k-1)\tilde{A}(k)^T + Q - K(k)\left[\tilde{A}(k)P(k|k-1)C_u(k)^T\right]^T \tag{A.48}$$

Here, Q and R are the process and measurement noise covariance matrices, respectively. Assuming uncorrelated noise sources, Q is parameterized as a block matrix with submatrix $\bar{Q}$:

$$\bar{Q} = \begin{bmatrix} q_0 & q_1 & \cdots & q_{N_P} \\ q_1 & q_0 & \cdots & q_{N_P-1} \\ \vdots & \vdots & \ddots & \vdots \\ q_{N_P} & q_{N_P-1} & \cdots & q_0 \end{bmatrix} \tag{A.49}$$

The scalars $q_0, q_1, \ldots$ represent the covariance and cross-covariance of turbulence among neighboring OPs, assuming homogeneous turbulence where spatial correlations depend on distance. In this formulation, the matrix Q is a tuning parameter.

The Kalman-augmented FLORIDyn model was validated against high-fidelity SOWFA simulations [57] using a simplified wind farm layout. The comparison revealed two primary advantages [38]:

1. A significantly improved match between the model-predicted and the measured power output of the turbines.
2. The ability of the Kalman filter to effectively correct deviations caused by inaccurate initial estimates of the system state, by continuously assimilating measurement data.

These results highlights the value of using all turbines as sensors in a closed-loop estimation framework. In contrast, the open-loop configuration relies solely on measurements from the front turbines to estimate the freestream velocity, which then serves as input to the model. Due to the inherently slow dynamics of wake propagation, this approach suffers from a prolonged transient phase, especially when the initial guess of the flow field is inaccurate—leading to substantial errors in the predicted response of downstream turbines.

The closed-loop configuration addresses this issue by continuously integrating measurements from downstream turbines to update the system state in real-time. As a result, it enhances both the accuracy and responsiveness of the model, particularly in scenarios where the initial flow field estimate is uncertain and wake effects evolve slowly over time.

However in general, a variation in power output might be caused by some other factor than a change in flow speed, such as the displacement of the wake or a change in wind direction [27], [18]. Therefore assuming the reason for the fluctuations in the predicted power response of the downstream machines being only related to a variation in the wind speed, as done in **Equation A.46**, could bring to a nonphysical representation of the real flow field. This issue has been addressed in other implementations of the closed-loop framework, taking into account different measurements in the correction scheme of the model [27], [18], [33]. In [18] two different Kalman based algorithms were developed, one correcting the wind speed estimate and the other one wind direction changes. Alternative estimation methods have been successively introduced in the literature, moving from the standard Kalman filter algorithm, to the Ensemble Kalman Filter (EnKF)[36].

[18] implemented an EnKF to correct the prediction of the Gaussian FLORIDyn framework [16] described in **Appendix A.1**. Compared to the closed-loop reformulation of the original zone FLORIDyn formulation, the wind direction estimates are included in the filter, to take into account other factors that might affect the power output of the farm, and an estimation of the system's uncertainties is made, rather than assuming a priory knowledge of it. The model equations describing the state propagation [16] can be rewritten in matrix form as follows:

$$\begin{aligned}\begin{bmatrix} x_L(k+1) \\ x_T(k+1) \\ x_{WF}(k+1) \end{bmatrix} &= \begin{bmatrix} A_{L,L} & 0 & A_{L,WF}(x_{WF}(k)) \\ 0 & A_{T,T} & 0 \\ 0 & 0 & A_{WF,WF} \end{bmatrix} \begin{bmatrix} x_L(k) \\ x_T(k) \\ x_{WF}(k) \end{bmatrix} \\ &+ \begin{bmatrix} \delta(x_L(k), x_T(k), x_{WF}(k)) \\ 0 \\ 0 \end{bmatrix} + \begin{bmatrix} B_L & 0 & 0 \\ 0 & B_T & 0 \\ 0 & 0 & B_{WF} \end{bmatrix} \begin{bmatrix} l_T(k) \\ x_{T,0}(k) \\ x_{WF,0}(k) \end{bmatrix}\end{aligned} \tag{A.50}$$

where, as already described in **Appendix A.1**, x_L refers to all OP location states, while x_T and x_{WF} refer to all stored turbine states and the stored wind field states, respectively. The OP states are described by these three states since each air particle carries in its motion the information about the control state of the turbines and background wind fields inherited at the time of its creation at the rotor plane. Subsequently, they can be clustered in one matrix.

The matrices $A_{L,L}$, $A_{T,T}$ and $A_{WF,WF}$ have a similar lower-diagonal block structure, ensuring that one state is propagated to the next row for each turbine and its OPs. The propagation of the OPs following the main wind direction and wind speed is described by the matrix $A_{L,WF}(x_{WF}(k))$. The nonlinear term $\delta(x_L(k), x_T(k), x_{WF}(k))$ characterizes the centerline deflection.The matrix $A_{L,L}$ is given by:

$$A_{L,L} = \begin{bmatrix} A_{L,L,T1} & 0 & \cdots & 0 \\ 0 & A_{L,L,T2} & \cdots & 0 \\ \vdots & \vdots & \ddots & \vdots \\ 0 & 0 & \cdots & A_{L,L,T_{n_T}} \end{bmatrix} \tag{A.51}$$

with:

$$A_{L,L,Ti} = \begin{bmatrix} 0 & 0 & \cdots & 0 \\ A_{L,L,OP1} & 0 & \cdots & 0 \\ 0 & A_{L,L,OP2} & \ddots & \vdots \\ \vdots & \ddots & \ddots & 0 \\ 0 & \cdots & 0 & A_{L,L,OP_{n_{OP,T}}} \\ 0 & \cdots & \cdots & 0 \end{bmatrix} \tag{A.52}$$

and

$$A_{L,L,OP_i} = I_{n_L} \tag{A.53}$$

where I_{n_L} is the identity matrix of size $n_L \times n_L$, and n_L describes the number of location states per OP. The number of turbines is denoted by n_T, and $n_{OP,T}$ represents the number of OPs per turbine.

The matrices $A_{T,T}$ and $A_{WF,WF}$ are similar in structure, they only differ in the size of their smallest components. Specifically, the matrices $A_{T,T,OP}$ and $A_{WF,WF,OP}$ differ in size because the number of stored turbine states and wind field states is different.

The matrix $A_{L,WF}(x_{WF}(k))$ is described by the same structure than $A_{L,L}$; only the smallest component differs:

$$A_{L,WF,OP} = \begin{bmatrix} \Delta t \cos(\varphi_{OP}) & 0 \\ \Delta t \sin(\varphi_{OP}) & 0 \\ 0 & 0 \end{bmatrix} \tag{A.54}$$

where Δt is the time step of the simulation and φ_{OP} is the wind direction at the location of the OP. The number of wind field states is given by n_{WF}. The input matrix B_L feeding inputs into the first OPs of each turbine is defined as:

$$B_L = \begin{bmatrix} B_{L,T_1} & 0 & \cdots & 0 \\ 0 & B_{L,T_2} & \cdots & 0 \\ \vdots & \vdots & \ddots & \vdots \\ 0 & 0 & \cdots & B_{L,T_{n_T}} \end{bmatrix} \tag{A.55}$$

with:

$$B_{L,T_i} = \begin{bmatrix} I_3 & 0 \\ 0 & 0 \end{bmatrix} \tag{A.56}$$

. The other two input matrices B_T and B_{WF} are defined analogously. However, B_{T,T_i} and B_{WF,T_i} consist only of an identity matrix in the first rows, unlike B_{L,T_i} which is accompanied by zero blocks:

$$B_{WF,T_i} = \begin{bmatrix} I_{n_{WF}} \\ 0 \end{bmatrix} \tag{A.57}$$

As already mentioned, turbines are treated as sensors in this framework. Wind direction is assumed to be measured via wind vanes installed on the turbines, and power output is used to estimate the background free-stream wind speed [16]. This allows the algorithm to rely only on already available data from each turbine.

The estimated power output is then calculated using the effective wind speed $\hat{u}_{\text{eff}}$ and the power coefficient C_P as in **Equation A.30**.

The effective wind speed $\hat{u}_{\text{eff}}$ is computed from the free-stream estimate $\hat{u}_{\text{free}}$ and the wake reductions from all upstream turbines as in **Equation A.33**:

The power coefficient is calculated using the actuator disk theory [29]. For a condition of axial flow and no yaw, it can be expressed as:

$$C_P = 4a(1-a)^2 \tag{A.58}$$

Setting the induction factor to the Betz limit:

$$a = \frac{1}{3} \tag{A.59}$$

The wind speed reduction is based on the Gaussian wake model [12] and implemented as described before in **Equation A.2**. **Equation A.33** uses the free wind speed at the turbine locations, which is based on the OP state x_{WF} to estimate the effective wind speed at the rotor. Originally, as it was described in **Appendix A.1**, only the states of the closest upstream and downstream OP have been used to interpolate the free wind speed at the turbine location. However, defining a vector $\hat{u}_{\text{free}}$ as an intermediate output of the system at every turbine location, would result in a very sparse output matrix. As an example, the form of the matrix for a layout of two turbines where the first one is uninfluenced and the second one is in the wake of the first is reported:

$$\hat{u}_{\text{free}} = C(k) \cdot x_{\text{WF},u} \tag{A.60}$$

with

$$C(k) = \begin{bmatrix} 1 & 0 & \cdots & 0 & & & & & \\ 0 & \cdots & 0 & w_1 & w_2 & 0 & \cdots & 0 \end{bmatrix} \tag{A.61}$$

where $C(k)$ is the time-varying output matrix of the state-space system and w_1,w_2 are the non-zero interpolation weights. In this interpolation scheme, the free wind speed at the second turbine is estimated from two OPs in the wake of the first turbine, based on the weights w_1 and w_2.This formulation creates a very sparse C matrix which would be problematic for the application of the EnKF: As the estimator works by employing multiple versions of the model, all evolving slightly differently over time, the wind speed states of different ensemble members diverge and so do the locations of the OPs. Since the formulation of C is so sparse, different OPs and therefore different states would contribute to the wind speed estimate in each member of the ensemble. However, the estimator framework is built around the premise to estimate and correct the same state across all the elements of the ensemble, which is no longer the case with this sparse output matrix. Therefore, the formulation of C has been modified in order to include more non-zero entries.

Furthermore, it has to be ensured that the same states are identified across all the elements of the ensemble. To solve this task,a spatio-temporal averaging approach by weighting every OP according to its downwind and crosswind distance to the location of interest and based on the time passed since its creation has been introduced. At the location of interest, the weighted average of all OPs' states returns the free wind speed estimate. Weights are computed using a Gaussian function:

$$w(d_{\text{dw}}, d_{\text{cw}}, t_{\text{OP}}) = \exp\left(-\left[\frac{d_{\text{dw}}^2}{2\sigma_{w,\text{dw}}^2} + \frac{d_{\text{cw}}^2}{2\sigma_{w,\text{cw}}^2}\right]\right) \cdot \exp\left(-\frac{(t - t_{\text{OP}})^2}{2\sigma_{w,t}^2}\right) \tag{A.62}$$

where d_{dw} and d_{cw} are the downwind and crosswind distance to the location of interest, $t_{\text{OP}}$is the time at which the OP was created and t is the current time.This weighting allows to consider a broader range of OPs as shown in **Figure A.10**.

It also introduces three new tuning constants σ_{cw}, σ_{dw} and $\sigma_{w,t}$ which control the downwind, crosswind, and temporal width of the Gaussian weighting function,

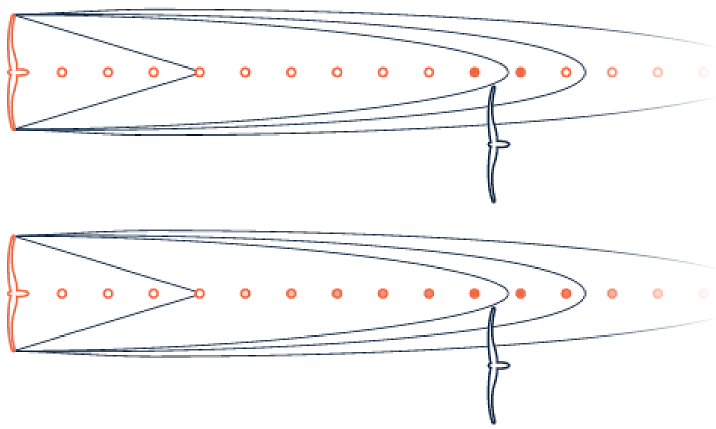

Figure A.10. The original interaction scheme between OPs and downstream turbines as presented in [38] and [17], along with the weighted case introduced in [18].

respectively. With this reformulation of the weights, each advancement step, the C matrix is therefore re-computed and its entries become larger for close and younger OPs, and they become smaller for older, further away OPs. The propagation distance of the OPs is also reformulated according to the new interpolation scheme which is represented by $A_{L,WF}(x_{WF}(k))$ in **Equation A.50**. This change overcomes the issue of one OP overtaking the other and preserves the low-frequency changes in the wind field. In order to take into account for these changes in the **Equation A.50**, the matrix $A_{L,WF}(x_{WF})$ has been modified introducing a weighting matrix WWF, as well as weighting its input:

$$\tilde{A}_{L,WF}(k, \mathbf{x}_L, \mathbf{x}_{WF}) = A_{L,WF}\left(W_{WF}(k, \mathbf{x}_L)\, \mathbf{x}_{WF}\right) W_{WF}(k, \mathbf{x}_L) \tag{A.63}$$

Therefore, the state **Equation A.50** is reformulated as follows:

$$\begin{aligned}
\underbrace{\begin{bmatrix} \mathbf{x}_L(k+1) \\ \mathbf{x}_T(k+1) \\ \hat{\mathbf{x}}_{WF}(k+1) \end{bmatrix}}_{\mathbf{x}(k+1)} &= \underbrace{\begin{bmatrix} A_{L,L} & 0 & \tilde{A}_{L,WF}(k, \mathbf{x}_L, \hat{\mathbf{x}}_{WF}) \\ 0 & A_{T,T} & 0 \\ 0 & 0 & A_{WF,WF} \end{bmatrix}}_{A_1} \underbrace{\begin{bmatrix} \mathbf{x}_L(k) \\ \mathbf{x}_T(k) \\ \hat{\mathbf{x}}_{WF}(k) \end{bmatrix}}_{\mathbf{x}(k)} \\
&+ \underbrace{\begin{bmatrix} \mathbf{d}(\mathbf{x}_L(k), \mathbf{x}_T(k), \hat{\mathbf{x}}_{WF}(k)) \\ 0 \\ 0 \end{bmatrix}}_{A_2} + \underbrace{\begin{bmatrix} B_L & 0 & 0 \\ 0 & B_T & 0 \\ 0 & 0 & B_{WF} \end{bmatrix}}_{B} \underbrace{\begin{bmatrix} \mathbf{l}_T(k) \\ \mathbf{x}_{T,0}(k) \\ \hat{\mathbf{x}}_{WF,0}(k) \end{bmatrix}}_{\mathbf{u}} \\
&+ \underbrace{\begin{bmatrix} 0 \\ 0 \\ \mu_{WF} \end{bmatrix}}_{\mu}
\end{aligned} \tag{A.64}$$

The noise combines a contribution for wind speed $\mu_u \sim \mathcal{N}(0, Q_u)$, and one for the wind direction $\mu_\varphi \sim \mathcal{N}(0, Q_\varphi)$, which are assumed to be Gaussian noise according to the underlined assumptions of the EnKf. All the members of the ensemble are propagated in time using **Equation A.64**

adding an independent term onto each state, and in this case, the noise matrices Q_u, Q_φ take a diagonal form. The reformulated state expressed by **Equation A.64**, is defined as the forecasting state of all the ensemble members e_i, $\hat{x}^f_{WF,e_i}$.

Since $\hat{\mathbf{x}}_{WF}$ is perturbed individually for all ensemble members, and the values of $\hat{\mathbf{x}}_{WF}$ are coupled to $\mathbf{x}_L$, also the OPs position changes differently for all components of the ensemble. Depending on how far the ensembles have diverged from one another, the $\hat{\mathbf{x}}_{WF}$ states are at different locations of each ensemble member e_i. The EnKF framework, however, assumes the states to describe the same location. This is an inherent characteristic for all simulations which include, or consist of, Lagrangian markers, particles traveling based on their own state To solve this issue the authors apply the weighting equation to the mean position of the OPs $\bar{x}_L$ across all ensemble members **Equation A.62** to find the representative state of the ensemble at $\bar{x}_L$. This can be seen as a coordinate transformation from the states of the ensemble to the mean state of the ensemble. The corrected state would then need to be projected back onto the ensemble states; however, being the inversion of the weighting matrix numerically difficult, it is assumed to be equal to an identity matrix. This assumption is supported by the fact that the weighting matrix has a diagonally dominant structure for the OPs which index in the wind field area. This approximation cannot hold for more diverging wind directions and for regions where no state correction is possible. If measurements are available, the forecast state $\hat{x}^f_{WF,e_i}$ of the ensemble state e_i is corrected using the difference in predicted outputs and measured outputs with **Equation A.65**. The result is the analysis state a $\hat{x}^a_{WF,e_i}$, which can be expressed for the general formulation of the analysis step as follows:

$$\hat{x}^a_{WF,e_i} = \hat{x}^f_{WF,e_i} + K \cdot \left[d_{e_i} - g\left(x_{L,e_i}, x_T, \hat{x}^f_{WF,e_i}\right)\right] \tag{A.65}$$

where K is the Kalman gain matrix, $g\left(x_{L,e_i}, x_T, \hat{x}^f_{WF,e_i}\right)$ describes the nonlinear output function which converts the ensemble field state to the predicted measurements and d_{e_i} is a set of polluted system measurements.x_T is assumed to be equal across all ensemble states. If no measurements are available, **Equation A.66** is used to determine the analysis state instead of **Equation A.65**.

$$\hat{x}^a_{WF,e_i} = \hat{x}^f_{WF,e_i} \tag{A.66}$$

The authors assume that wind direction and wind speed are uncorrelated and can, therefore, be corrected independently using two separate filters. This assumption is motivated by the observation that wind speed and direction exhibit different correlation patterns over varying spatial scales. As a result, the calculation of the Kalman gain matrix is divided into two distinct components: K_u, used to correct wind speed, and K_j, used to correct wind direction.

For the correction of the wind speed, the power generated is used as a nonlinear output of a function that converts the wind speed into power generated. For the wind direction, a direct measurement at the turbine location is assumed. Therefore, the output function also varies and the two gains are computed in a different manner.

The Kalman gain matrix K_u using of a non-linear output function. First, the averaged state error matrix $E_{\hat{x}^f_{WF,u}}$ is calculated:

$$E_{\hat{x}^f_{WF,u}} = \frac{1}{\sqrt{n_e}} \left[\left(\hat{x}^f_{WF,e_1} - \bar{x}^f_{WF,u} \right), \left(\hat{x}^f_{WF,e_2} - \bar{x}^f_{WF,u} \right), \ldots, \left(\hat{x}^f_{WF,ene} - \bar{x}^f_{WF,u} \right) \right] \tag{A.67}$$

where $\hat{x}^f_{WF,e_i}$ describes the wind speed estimate of the $i-th$ ensemble and $\bar{x}^f_{WF,u}$ describes the average across all ne ensemble members. The same is calculated for the output of the ensembles:

$$\hat{E}^P = \frac{1}{\sqrt{n_e - 1}} \left[\left(\hat{P}_{e_1} - \bar{P} \right), \left(\hat{P}_{e_2} - \bar{P} \right), \ldots, \left(\hat{P}_{e_{ne}} - \bar{P} \right) \right] \tag{A.68}$$

where $\hat{P}_{e_i}$ denotes the estimation of power generated by the $i - th$ ensemble component, which is directly dependent on f $\hat{x}^f_{WF,u}$as shown in equations **Equation A.30**, **Equation A.24**. The state output error correlation covariance matrix, **Equation A.69**, and the output error covariance matrix, **Equation A.70** are computed as:

$$\mathcal{C}_{\hat{x}^f_{WF,u},\hat{P}} = E_{\hat{x}^f_{WF,u}} E^\top_{\hat{P}} \tag{A.69}$$

$$\mathcal{C}_{\hat{P},\hat{P}} = E_{\hat{P}} E^\top_{\hat{P}} \tag{A.70}$$

As mentioned before, power measurements P are assumed to be affected by a white noise disturbance:

$$P^{e_i} = P + e_{i,P}, \quad e_{i,P} \sim \mathcal{N}(0, R_P) \tag{A.71}$$

where $e_{i,P}$ is an artificial error with a Gaussian distribution, an average of 0 and the covariance matrix R_P. The matrix R_P is a parameter that needs to be set based on prior knowledge and tuning. If no random perturbations are added to the measurements, the variance of the analyzed ensembles becomes too low and the ensemble components don't diverge enough [18]. The wind speed is then corrected as follows:

$$K_u = \mathcal{C}_{\hat{x}^f_{WF,u},\hat{P}} \left[\mathcal{C}_{\hat{P},\hat{P}} + R_P \right]^{-1} \tag{A.72}$$

$$\hat{x}^a_{WF,u,e_i} = \hat{x}^f_{WF,u,e_i} + K_u \left(P^{e_i} - \hat{P}^{e_i} \left(\hat{x}^f_{WF,u,e_i} \right) \right) \tag{A.73}$$

The formulation of the EnkF for correcting the wind direction is different. A measurement of the wind direction is assumed to be available at the turbine locations. The state error $E_{\hat{x}^f_{WF,\varphi}}$ is calculated equivalently to **Equation A.69**. Contrary to the wind speed estimation, it is then used to calculate the state error covariance matrix:

$$\mathcal{C}_{\hat{x}^f_{WF,\varphi},\hat{x}^f_{WF,\varphi}} = E_{\hat{x}^f_{WF,\varphi}} E^\top_{\hat{x}^f_{WF,\varphi}} \tag{A.74}$$

To obtain the relation between the states and the output, the output matrix $\mathcal{C}_{\varphi,e_i}$ is needed. It is given by the rows of the weighting matrix $W_{WF}(k, x_L)$ which combine $x^f_{WF,\varphi}$ to a wind direction estimate at the OP at the rotor plane as in

Equation A.63. Due to the fact that OPs occupy slightly different locations in each ensemble member $\mathcal{C}_{\varphi,e_i}$ is slightly different for each ensemble members. The assumption $C_{j,e_1} \approx C_{j,e_2} \approx \cdots \approx C_{j,e_{n_e}}$ is made. An individual $K_{\varphi,ei}$ is made for each ensemble component, based on the different $C_{\varphi,ei}$ matrices. The wind direction measurements φ are polluted with an error $e_{i,j} \sim \mathcal{N}(0, R_j)$ which is equal to the power measurements in **Equation A.73**. As with R_P, R_φ is a parameter that needs to be set. The resulting analysis step is described by:

$$K_{\varphi,e_i} = \mathcal{C}_{\hat{x}_{WF,\varphi},\hat{x}_{WF,\varphi}} C_\varphi^\top \left(C_\varphi \mathcal{C}_{\hat{x}_{WF,\varphi},\hat{x}_{WF,\varphi}} C_\varphi^\top + R_\varphi \right)^{-1} \tag{A.75}$$

$$\hat{x}^a_{WF,\varphi,e_i} = \hat{x}^f_{WF,\varphi,e_i} + K_{\varphi,e_i} \left(\varphi_{e_i} - C_\varphi \hat{x}^f_{WF,\varphi,e_i} \right) \tag{A.76}$$

From the equations the difference in the calculation of the Kalman gain for the two filters is noticeable: **Equation A.75** uses the state-error-covariance matrix and a linear output matrix, while **Equation A.72** uses the output-error-covariance matrix and the output-to-state-error-covariance matrix. As a result, the final equation of the analysis state related to the wind speed, **EquationA.76** corrects based on a linear relation of the output to the estimated state, while **EquationA.73** compares outputs with a nonlinear relation to the estimated state. Further details about the Kalman Filter formulation and applications can be found in the reference article. The model was tested in a 3 x 3 wind farm case with heterogeneous and changing flow conditions taking as reference a high-fidelity SOWFA simulation [57]. The results show that the framework was able to follow the changes in the flow field.

A different implementation of the Ensemble Kalman Filter was proposed in [27] and designed for the FLORIDyn version characterized by two different sets of OPs to describe the background and the wake flow regimes [26]. The purpose of the work was to develop a closed-loop Wake model that is able to estimate the contribution to the wind field fluctuations related to different spatio-temporal scales affecting the power production and loadings of the wind turbines [27]. The small-fast components of the flow are referred to in [27], as the ones caused by the turbulent nature of the wind field, and are responsible for the meandering of wakes. These fluctuations are difficult to predict since they develop on intra-turbine scales as the flow travels from an upstream to a downstream machine where no measurements are usually available. On the other hand, long-scale slow fluctuations are related to flow structures of bigger size or variations in the ambient background wind speed, such as a wind direction change front that propagates throughout a wind farm. When these large-slow flow components are bigger than intra-turbine spacings they can affect different machines in the plant. Therefore they can be more easily estimated with a certain accuracy through the analysis of the wind turbine operative data. As it is argued in [27], both slower and faster flow scales have to be taken into account for wind farm control and monitoring applications. For example, the slow change of wind direction over a farm modifies the propagation of the wakes inside and outside the plant, while the faster scale fluctuations control the oscillations of power that might prevent the accurate tracking of a power signal and contribute to the loads of wind turbines. The aim of the study was therefore to lay the foundation for the development of a multi-scale EnKF framework able to improve the prediction of the inflow dynamics on a broad range of spatio-temporal wind fluctuation lengths affecting turbine performance.

In [27] the focus was on improving the predictions of the model for the turbulent fluctuations of the background ambient wind speed U_a and the meandering of the wake y_w, x_w at the downstream turbines, therefore the state vectors implemented in the ensemble for the filter are made of these three quantities. The equations and model formulation are the same as those reported in **Section 2.2.1**, with the difference that in this case the measured quantity is the power output of the waked turbine.

Appendix B

SAR data for wind energy: state of art

This appendix reports a comprehensive overview of the current state-of-the-art applications of Synthetic Aperture Radar (SAR) imagery in the wind energy sector, which include site assesment studies and wind farm clustr wake analysis.

For site assessment analysis, given the spatial coverage of SAR/scatterometer acquisitions it is possible to perform an evaluation of the available wind resources at a specific site or region. Several studies [3], [64], [11] already proved that dataset of satellite images over time at the same location can be deployed for performing statistical analysis, in order to infer the parameters of the wind speed Weibull distribution and the wind rose of the site. The mean wind speed can be defined as the arithmetic mean wind speed from SAR images as [3]:

$$U = \frac{1}{F}\sum_{n=1}^{N} u_n \tag{B.1}$$

Where F is the number of available acquisitions and u_n is the generic acquisition from the images . Clustering the acquisitions by month F_m it is possible to make a weighted arithmetic mean wind speed at a site location taking into account the seasonal variability effect.

$$U_{\mathrm{sc}} = \sum_{m}^{N}\left(\frac{F_m}{F}U_m\right) \tag{B.2}$$

Where:

$$U_m = \frac{1}{F_m}\sum_{n=1}^{N} u_{n,m} \tag{B.3}$$

Is the mean wind speed for the acquisitions $u_{n,m}$ of month m. Biases between SAR-retrieved wind speeds and in-situ observations are often inconsistent across different radar sensors. This inconsistency arises because each satellite introduces spatial variability due to differences in spatial coverage and acquisition geometry over the study area. Moreover, when wind speed samples are combined from multiple SAR missions, such biases may become more pronounced. Several factors may contribute to these discrepancies, including the use of different GMFs for wind retrieval and inconsistencies in the calibration of the NRCS. Variations in sensor-specific parameters, incidence angle ranges, and polarization further complicate direct comparisons between datasets from different platforms. The intercalibration of SAR observations, not only increases the sampling rate, as previously mentioned, but it also improves the overall quality of a dataset including retrieval from sensors with different specifics: it has been shown from a bias reduction in the range of to -0.2 to 0.0 ms^{-1}, while at the same time improving the root-mean-squared error from 1.67 to 1.46 ms^{-1} [10], [3]. Another limitation is related to the fixed overpass times of satellites. Acquisitions from a single satellite are unable to capture diurnal wind variations, and the limited number of samples may further restrict site-specific analyses [64, 11]. In this context, intercalibration between multiple datasets can also help to mitigate these issues.

Another limitation of are also related to the fixed time passing of the satellites. Acquisitions from a single satellite not able to capture diurnal cycling variations of the wind and the limited number of samples that might be available for certain sites [64], [11] . Therefore intra-calibration might be also useful to overcome this issue. According to [64] around 70 samples are sufficient to estimate mean wind speed and the Weibull scale parameter but around 2,000 samples are needed to estimate energy density and the Weibull shape parameter at the 10% confidence level (significance 95%). The result makes it clear that the accuracy of SAR-based wind resource statistics is adequate for pre-feasibility studies. In other words, the SAR-based wind resource map may be used as a guide to site an offshore meteorological mast in a wind farm project. If high-quality offshore observations are available, the local wind gradients at 10 m above sea level may be evaluated from SAR wind resource maps. In fact [34] analyzed the effect of atmospheric stability on wind speed gradients and wind speed recovery for the German Bight area using Sentinel 1-A data over an area of 170 km. Spatial transects perpendicular to the coast, were subdivided into 2 km bins, which leads to boxes of 2 km x 13 km each. The wind speed is therefore spatially averaged over each 26 km^2. Three types of horizontal wind speed gradients (different types of normalization and scaling of the wind speed):

1. the absolute wind speed $u(x)_{10}$ horizontal wind speed derived from SAR at 10 m

2. the wind speed increase $\delta u(x)_{10}/u_{\text{land}}$ (SAR is not able to provide wind information over land, estimates of land can only be approximations based on measurements over areas covered by the sea that are very close to the land boundary);

3. the normalized wind speed increase $Ru(x)_{10} = \delta u(x)_{10}/u_{\text{land}}$

The analysis of the results proved that atmospheric stability and seasonal variability of the atmospheric stratification influence the structure of the horizontal wind speed gradients: wind speed increases with growing distance from the coast in situations where the wind is blowing from land to sea. The adjustment distance (at which the wind speed has reached the 95% of its final value offshore.) is shorter in unstable conditions where strong mixing and turbulence force the winds to quickly adjust to an equilibrium and stable state. The interesting finding from the analysis carried with satellite images was that the transition zone land-marine internal boundary layer (IBL) could reach an extension up to 100 km offshore in stable conditions (shorter distance are associated with unstable conditions).

Coastal-induced wind speed gradients from Sentinel-1 images were also evaluated against colocated acquisitions from different LiDAR profilers. A good agreement was found in the trends of both the measured wind speeds from SAR and Lidars with RMSE in the order of from 1.3-1.4 ms^{-1} [4].

Several studies have investigated the use of satellite data to analyze the environmental impact of offshore wind farms (OWFs), particularly in terms of cluster wake effects. As already mentioned in the introduction, the wake produced by a wind farm has significant implications—not only for the operational productivity and environmental footprint of the existing plants, but also for assessing nearby areas for future development.

Due to their extensive spatial coverage, satellite images—especially those acquired via Synthetic Aperture Radar (SAR)—allow for the qualitative observation of the spatial extent of velocity deficits caused by wind farm wakes. These wake structures can persist over several tens of kilometers downstream, particularly under neutral or stable atmospheric boundary layer conditions [66], [62] and [53]. Despite the lack of standardized procedures in the literature for such analysis, a common methodology involves extracting wind speeds along transects placed both upstream and downstream of the OWF using SAR data.

To avoid contamination from strong radar reflections of turbine structures, transects are typically positioned at a safe distance from the wind farms—ranging from 200 meters to several kilometers, depending on the case study, as alredy reported in **Section 3.1**. SAR images are filtered for anomalous values (e.g., using a 2 dB threshold or CFAR algorithms to remove oil slicks or specular reflections [63], [64]). Since SAR images do not directly provide wind direction, this must be inferred from external sources such as meteorological models or in-situ data. Based on the known wind direction, transects are aligned accordingly and wind speeds are extracted .

Transects can be constructed as linear sequences of individual pixel values (e.g., 500–100 m resolution), or as box-averaged bins of variable sizes depending on SAR processing and case-specific needs (typically from 200 m up to 2.6 km). For each wind direction sector, the wake effect is evaluated either as a normalized velocity deficit (between corresponding upstream and downstream points) or as a simple wind speed difference at corresponding latitudes.

A notable case study is presented in [66], which investigated wake interactions among multiple wind farms in the North Sea, with a particular focus on the impact on the Global Tech 1 wind farm. Transects were positioned up to 9 km upstream of Global Tech 1, and SAR-derived wind speeds were compared against in-situ measurements, including LIDAR data and SCADA-based turbine power output.

The results demonstrated strong agreement between SCADA power trends and SAR-extracted wind speeds, both under full wake conditions and in more complex partial wake scenarios. These satellite-based observations revealed that wakes can extend over 50 km under stable atmospheric conditions, and even up to 55 km in weakly unstable stratification.

In the analyzed cases, average wake-induced wind speed deficits reached 2.3 ms^{-1} (25%) at 24 km downstream and 2.2 ms^{-1} (21%) at 55 km downstream of the upstream farms. Such sensory fusion (SAR + SCADA + LIDAR) has proven to be a robust approach for wake analysis: LIDAR offers accurate but spatially limited data (10–20 km), while SAR provides broad coverage (170×80 km) though limited to qualitative snapshots. In this study, SAR-derived wind speeds required a 1–2 ms^{-1} correction before meaningful comparison with power output.

The SAR wind data were processed at 10 m above sea level with a spatial resolution of 1×1 km. Wind speed values ranged from 0 to 25 ms^{-1} with an RMSE below 2.0 ms^{-1}, and wind direction RMSE below 30°. Errors stemmed from various sources, including neutral boundary layer assumptions in the GMF, noise, hard targets, and the use of already-processed Sentinel-1 data. A SAR analysis tailored to site-specific conditions could reduce these uncertainties.

Another critical factor in evaluating cluster wake effects is the coastal morphology near offshore installations. Horizontal wind speed gradients induced by land-sea transitions can mimic or mask wake effects. For this reason, [62] proposed estimating the true wake deficit by subtracting wind speed changes observed in pre-construction satellite images from those observed post-construction. This method allows to decouple the background gradients from turbine-induced effects.

In their approach, satellite images were grouped into three broad wind direction sectors of 90 degrees: easterly (45°–135°), southerly (135°–225°), and westerly (225°–315°), to maximize sample counts. Average wind speed values were calculated at each transect point for both pre-and post-construction datasets, using ENVISAT (2002–2012) for pre-commissioning and Sentinel-1A/1B for post-commissioning data. Eight wind farm sites across the North Sea were analyzed.

The results showed that pre-commissioning upstream/downstream wind speeds could differ by up to 4% due to coastal gradients alone—sometimes larger than the wake deficit itself. After correcting for these gradients, wake effects were detected in 22 of 24 cases. The post-commissioning downstream wind speeds showed a 2–10% reduction after background correction.

Importantly, the magnitude of wake deficits varied substantially (1–10%) depending on the site and wind direction. Although results were computed at 10 m altitude, larger deficits are expected at hub height. The average corrected wake deficits were found to be proportional to the installed capacity of the OWF—larger farms generated more pronounced downstream velocity deficits.

Some unexpected results have been found by [62] and are reported in this chapter to highlight some possible limitations of the Satellite technology: wind speeds extracted on the upstream side of each wind farm should, in principle, show similar wind speed values before and after OWF commissioning. However, in most investigated cases, differences larger than 0.5 m/s are found. The actual wind speed may be different for the periods analyzed in the study (e.g., before and after the OWF commissioning). According to the authors, these discrepancies might be related to several causes which can be summarized as follows:

- **Atmospheric stability assumptions:** The GMF CMOD5.N assumes neutral atmospheric conditions, which do not always correspond to the actual conditions. This mismatch can lead to incorrect wind speed estimations. In northern European sea areas, seasonal instability (autumn/winter) may lead to underestimation, while springtime stable conditions may cause overestimation.

- **Diurnal and seasonal sampling bias:** Atmospheric stability affects the diurnal wind cycle. Since SAR acquisitions occur at fixed times daily, the resulting wind speed estimates may be biased.
- **Imbalanced sampling:** The number of observations before and after commissioning varies across sites, possibly skewing the comparison of wind speeds.
- **Direction binning issues:** Wind directions are binned into 90° sectors globally before analysis. This can displace the maximum velocity deficit, which may not align with the assumed downwind direction (e.g., E, W, N), reducing accuracy in some cases.
- **Early SAR data calibration:** Envisat SAR data from 2002–2012 suffer from calibration issues, potentially affecting wind deficit estimates.

Different definitions have been introduced in the literature to quantify wind speed gradients in the vicinity of wind farms. In [2], the gradient effect is defined as the difference in wind speed between the northernmost and southernmost turbines in the upstream row. Wind speeds are inferred from SCADA power output data and extrapolated to 10 meters height in order to compare them with values derived from SAR (Synthetic Aperture Radar) transects and the WRF model.

The comparison showed that SCADA and SAR data agree within 0.1%, while WRF predicts a wind speed gradient approximately 1% larger than that obtained from SCADA data.

The authors also analyzed wake effects by comparing SAR acquisitions taken before and after the commissioning of the wind farm, considering both short and long fetch scenarios. Their findings revealed a distinct wake signature at the long fetch, which was also detectable in SAR imagery.

The deviations between wind speed measurements derived from SAR and SCADA data are found to range between 0.3 and 0.6 ms^{-1}. These discrepancies may be attributed to several factors:

- Differences in measurement location: SCADA wind speeds are recorded at the turbine nacelles, while SAR-derived wind speeds are typically observed downstream of the wind farm;
- Temporal mismatches and differences in sample size: SAR acquisitions are snapshots in time, whereas SCADA data provide continuous measurements with high temporal resolution;
- Vertical positioning of measurements: SCADA data are representative of turbine hub height, whereas SAR retrievals refer to wind speeds over the sea surface. Since the most pronounced wake effects occur at hub height, stronger deficits are expected in SCADA observations compared to SAR.

The potential of SAR data for wind energy applications has already been assessed in several studies [3], [11], [64], [4],[34] . However, relatively few studies have focused on validating SAR-derived winds against *in situ* measurements. These validation efforts have generally concluded that non-negligible biases remain. Here, the term also includes remote sensing instruments such as profiling lidars.

As previously noted, SAR surface winds are retrieved by inverting backscatter data using GMFs, originally developed for scatterometers. However, SAR sensors differ in spatial resolution and may not be inter-calibrated with scatterometers, leading to additional biases. Furthermore,as already mentioned, GMFs may not fully capture the complex relationship between sea state and wind speed. For example, CMOD5, commonly applied for C-band SAR sensors (e.g., Sentinel-1), assumes neutral atmospheric stability, potentially leading to biased estimates under stable or unstable conditions.

Improving the accuracy of SAR wind speed retrievals via refined GMFs is essential, particularly in wind energy applications, where the wind power density is proportional to the cube of wind speed and thus highly sensitive to estimation errors. Given their wide spatial coverage, SAR acquisitions can also capture coherent atmospheric structures with spatial scales ranging from 0.5 to 5 km [72], [71] which modulate the sea surface roughness. These structures are indicative of different atmospheric boundary layer (ABL) stratification regimes and manifest as distinct textural patterns in SAR imagery. The 3-state MABL stratification classification is as follows: [72], [71] demonstrated that SAR-observed ocean surface textures are strongly linked to different atmospheric stratification regimes. To quantify this relationship, they developed a classification procedure based on the analysis of the Bulk Richardson number (R_i), a widely used parameter to characterize atmospheric stability [64]. Using this approach, the marine atmospheric boundary layer (MABL) was classified into three stratification regimes:

- **UBL (Unstable Boundary Layer)**: $R_i < -0.010$
- **NNBL (Near Neutral Boundary Layer)**: $-0.010 \leq R_i \leq 0.011$
- **SBL (Stable Boundary Layer)**: $R_i > 0.011$

The R_i values were initially computed using ERA5 reanalysis data and later validated using in situ measurements from the Coastal Pioneer Array (CPA) buoy, located in the Northwest Atlantic Ocean. Satellite images were visually examined to detect textural signatures associated with 12 separate phenomena. The classification showed that variations in SAR- observed atmospheric boundary layer eddies, or lack of them, correspond to specific R_i unstable regimes. On the other hand, strong vertical wind shear, typically occurring under stable stratification, which is critical for energy production and turbine loads, can be directly identified from SAR images by the absence of energetic eddies. SAR also provides a regional climatology of atmospheric stratification for offshore wind assessment, complementing other observations, and with potential application worldwide.

As previously mentioned, satellite sensors operating in different frequency bands have been employed for offshore wind energy research, with X-band SAR providing a notably higher spatial resolution compared to C-band sensors such as Sentinel-1. X-band imagery offers a more detailed representation of the wind field in and around wind farms, facilitating the analysis of wake propagation [64].

Notable X-band missions include TerraSAR-X, TanDEM-X, and COSMO-SkyMed. Based on TerraSAR-X and in-situ buoy data, the geophysical model function XMOD 2 was developed. Unlike conventional GMFs, XMOD2 is tuned to wind speeds obtained under various atmospheric stability conditions, allowing for the retrieval of *real* winds. Validation against buoy measurements shows that XMOD2-derived winds have a RMSE of 1.5 $\mathrm{m\,s^{-1}}$ and a bias of -0.2 to -0.3 $\mathrm{m\,s^{-1}}$, comparable to results from C-band $GMFs$ [64].

TerraSAR-X data processed with XMOD2 have been applied to investigate the propagation of wakes at the Alpha Ventus wind farm [53].

The most notable finding of the study is that wind direction plays a significant role in wake-merging behavior. The analysis also demonstrated that, due to the high spatial resolution of X-band images, the meandering of cluster wakes can be observed by analyzing wind speed variations along transects positioned at increasing distances downstream of the wind farm. Furthermore, the TS-X observations support the general conclusions of wake model simulations, indicating that higher turbulence intensity in the incoming flow accelerates wake recovery, resulting in shorter wake lengths detectable by satellite imagery

As already mentioned, one of the main limitations of satellite-based wind field retrieval is the relatively low temporal resolution, with only a limited number of scenes available per day. However, this limitation is expected to be mitigated in the near future by the deployment of small Synthetic Aperture Radar (SAR) satellites by private companies. These constellations will dramatically increase the availability of SAR imagery, potentially enabling hourly overpasses of a given location and delivering scenes with unprecedented spatial and temporal resolution. Among the emerging small-satellite systems, the StriX constellation operated by the Japanese company Synspective Inc. is particularly noteworthy. These satellites are equipped with X-band SAR sensors operating at a frequency of 9.65 GHz. $StriX - \beta$, the second satellite of the constellation, flies in a sun-synchronous orbit at an altitude of 560 km and currently provides twice-daily coverage over Europe. Wind fields retrieved from a series of $StriX - \beta$ SAR scenes were compared to wind speed observations from the FINO3 meteorological mast in the North Sea, as well as to wind fields retrieved from Sentinel-1 imagery [11]. The results showed a RMSE of 1.4-1.8 ms^{-1} and negative biases of -0.4 ms^{-1} and -1.0 ms^{-1} for StriX and Sentinel-1, respectively.

StriX observations were also analyzed for mapping offshore wind farm wakes generated by the DanTysk wind farm [41]. Thanks to the very high spatial resolution of $StriX - \beta$, the wakes were clearly visible in the SAR-derived wind fields as alternating streaks of high and low wind speeds downstream of individual turbines. Interestingly, in addition to the typical wake-induced wind speed deficits, certain scenes revealed *wake surpluses*, characterized by higher wind speeds downstream of the wind farm.

A statistical evaluation of the results from StriX satellites against Sentinel-1 results has been performed investigating the relationship between wake deficit and atmospheric stability, upstream wind speed, wind direction, and day of year (seasonal effects). The majority of cases show wind speed deficit as expected, but a surprisingly large fraction of cases both in StriX (34%) and Sentinel-1 (48%) show wind speed surplus. To investigate the origin of the observed wake surplus, mesoscale simulations using the Weather Research and Forecasting (WRF) model were conducted. These simulations confirmed that turbulent kinetic energy (TKE) plays a critical role: under certain conditions, added turbulence from the turbines enhances vertical mixing, bringing higher-momentum air down to near-surface levels. [34] also found that the wind was accelerated for 25 % of SAR scenes investigated for the Alpha Ventus offshore wind farm in the German Bight. Also the results from the study suggested that the values of NRCS were increased due to mechanical turbulence from the wind farm. This leads to an increase in downward momentum and influences the ocean surface. In conclusion, both StriX and Sentinel-1 data show comparable statistics in terms of wake deficit/surplus frequency. The availability of high-resolution, high-frequency SAR data from StriX-type constellations promises to significantly enhance our understanding of wind farm wake, especially when combined with mesoscale modeling that accounts for turbulence and atmospheric stability.

Bibliography

[1] Copernicus Climate Change Service (C3S). *ERA5 hourly data on single levels from 1940 to present*. Climate Data Store (CDS). Accessed: 2025-06-08. 2018. DOI: 10.24381/cds.adbb2d47. URL: https://cds.climate.copernicus.eu/datasets/reanalysis-era5-single-levels?tab=overview.

[2] T. Ahsbahs et al. "Applications of satellite winds for the offshore wind farm site Anholt". In: *Wind Energy Science* 3.2 (2018), pp. 573–588. DOI: 10.5194/wes-3-573-2018. URL: https://wes.copernicus.org/articles/3/573/2018/.

[3] T. Ahsbahs et al. "US East Coast synthetic aperture radar wind atlas for offshore wind energy". In: *Wind Energy Science* 5.3 (2020), pp. 1191–1210. DOI: 10.5194/wes-5-1191-2020. URL: https://wes.copernicus.org/articles/5/1191/2020/.

[4] Tobias Ahsbahs et al. "Validation of Sentinel-1A SAR Coastal Wind Speeds Against Scanning LiDAR". In: *Remote Sensing* 9.6 (2017). ISSN: 2072-4292. DOI: 10.3390/rs9060552. URL: https://www.mdpi.com/2072-4292/9/6/552.

[5] Tobias Ahsbahs et al. "Wind Farm Wakes from SAR and Doppler Radar". In: *Remote Sensing* 12.3 (2020). ISSN: 2072-4292. DOI: 10.3390/rs12030462. URL: https://www.mdpi.com/2072-4292/12/3/462.

[6] Dries Allaerts and Johan Meyers. "Gravity Waves and Wind-Farm Efficiency in Neutral and Stable Conditions". In: *Boundary-Layer Meteorology* 166.2 (2018). Epub 2017 Oct 13, pp. 269–299. DOI: 10.1007/s10546-017-0307-5.

[7] Mojtaba Maali Amiri, Milad Shadman, and Segen F. Estefen. "A review of physical and numerical modeling techniques for horizontal-axis wind turbine wakes". In: *Renewable and Sustainable Energy Reviews* 193 (2024), p. 114279. ISSN: 1364-0321. DOI: https://doi.org/10.1016/j.rser.2024.114279. URL: https://www.sciencedirect.com/science/article/pii/S1364032124000029.

[8] Merete Badger et al. "Bringing satellite winds to hub-height". English. In: *Proceedings of EWEA 2012 - European Wind Energy Conference and Exhibition*. EWEC 2012 - European Wind Energy Conference and amp; Exhibition, EWEC 2012 ; Conference date: 16-04-2012 Through 19-04-2012. European Wind Energy Association (EWEA), 2012. URL: http://events.ewea.org/annual2012/.

[9] Merete Badger et al. "Extrapolating Satellite Winds to Turbine Operating Heights". In: *Journal of Applied Meteorology and Climatology* 55.4 (2016), pp. 975–991. DOI: 10.1175/JAMC-D-15-0197.1. URL: https://journals.ametsoc.org/view/journals/apme/55/4/jamc-d-15-0197.1.xml.

[10] Merete Badger et al. "Inter-calibration of SAR data series for offshore wind resource assessment". English. In: *Remote Sensing of Environment* 232 (2019). ISSN: 0034-4257. DOI: `10.1016/j.rse.2019.111316`.

[11] Merete Badger et al. "Wind Retrieval from Constellations of Small SAR Satellites: Potential for Offshore Wind Resource Assessment". In: *Energies* 16.9 (2023). ISSN: 1996-1073. DOI: `10.3390/en16093819`. URL: `https://www.mdpi.com/1996-1073/16/9/3819`.

[12] Majid Bastankhah and Fernando Porté-Agel. "A new analytical model for wind-turbine wakes". In: *Renewable Energy* 70 (2014). Special issue on aerodynamics of offshore wind energy systems and wakes, pp. 116–123. ISSN: 0960-1481. DOI: `https://doi.org/10.1016/j.renene.2014.01.002`. URL: `https://www.sciencedirect.com/science/article/pii/S0960148114000317`.

[13] Majid Bastankhah and Fernando Porté-Agel. "Experimental and theoretical study of wind turbine wakes in yawed conditions". In: *Journal of Fluid Mechanics* 806 (2016), pp. 506–541. DOI: `10.1017/jfm.2016.595`.

[14] Christopher Bay et al. *FLORIS: A Brief Tutorial.* `https://www.nrel.gov/docs/fy20osti/75661.pdf`. Presented at the 5th Wind Energy Systems Engineering Workshop (WESE 2019), 2-4 October 2019, Pamplona, Spain. 2019.

[15] BayernCollab. *Anemometer and LIDAR – Measurement principle.* 2025. URL: `https://collab.dvb.bayern/spaces/TUMzfp/pages/70096831/Anemometer+and+LIDAR#AnemometerandLIDAR-Measurementprinciple`.

[16] M Becker, D Allaerts, and J W van Wingerden. "FLORIDyn - A dynamic and flexible framework for real-time wind farm control". In: *Journal of Physics: Conference Series* 2265.3 (May 2022), p. 032103. DOI: `10.1088/1742-6596/2265/3/032103`. URL: `https://dx.doi.org/10.1088/1742-6596/2265/3/032103`.

[17] M. Becker et al. "The revised FLORIDyn model: implementation of heterogeneous flow and the Gaussian wake". In: *Wind Energy Science* 7.6 (2022), pp. 2163–2179. DOI: `10.5194/wes-7-2163-2022`. URL: `https://wes.copernicus.org/articles/7/2163/2022/`.

[18] Marcus Becker, Dries Allaerts, and Jan-Willem van Wingerden. "Ensemble-Based Flow Field Estimation Using the Dynamic Wind Farm Model FLORIDyn". In: *Energies* 15.22 (2022). ISSN: 1996-1073. DOI: `10.3390/en15228589`. URL: `https://www.mdpi.com/1996-1073/15/22/8589`.

[19] M. Bertelè et al. "The rotor as a sensor – observing shear and veer from the operational data of a large wind turbine". In: *Wind Energy Science* 9.6 (2024), pp. 1419–1429. DOI: `10.5194/wes-9-1419-2024`. URL: `https://wes.copernicus.org/articles/9/1419/2024/`.

[20] Marta Bertelè et al. "Wind inflow observation from load harmonics". In: *Wind Energy Science* 2.2 (2017), pp. 615–640.

[21] Gunjit Bir. "Multi-Blade Coordinate Transformation and its Application to Wind Turbine Analysis". In: *46th AIAA Aerospace Sciences Meeting and Exhibit*. DOI: 10.2514/6.2008-1300. URL: https://arc.aiaa.org/doi/abs/10.2514/6.2008-1300.

[22] James Bleeg et al. "Wind Farm Blockage and the Consequences of Neglecting Its Impact on Energy Production". In: *Energies* 11.6 (2018). ISSN: 1996-1073. DOI: 10.3390/en11061609. URL: https://www.mdpi.com/1996-1073/11/6/1609.

[23] Pietro Bortolotti et al. *IEA Wind TCP Task 37: Systems Engineering in Wind Energy - WP2.1 Reference Wind Turbines*. Tech. rep. National Renewable Energy Lab. (NREL), 2019.

[24] C.L. Bottasso, S. Cacciola, and J. Schreiber. "Local wind speed estimation, with application to wake impingement detection". In: *Renewable Energy* 116 (2018), pp. 155–168. ISSN: 0960-1481. DOI: https://doi.org/10.1016/j.renene.2017.09.044. URL: https://www.sciencedirect.com/science/article/pii/S0960148117309072.

[25] Emmanuel Simon Pierre Branlard. *Wind Turbine Aerodynamics and Vorticity-Based Methods: Fundamentals and Recent Applications*. English. Vol. 7. Research Topics in Wind Energy. Springer, 2017. ISBN: 978-3-319-55163-0. DOI: 10.1007/978-3-319-55164-7.

[26] R. Braunbehrens, J. Schreiber, and C. L. Bottasso. "Application of an open-loop dynamic wake model with high-frequency SCADA data". In: *Journal of Physics: Conference Series* 2265.2 (May 2022), p. 022031. DOI: 10.1088/1742-6596/2265/2/022031. URL: https://dx.doi.org/10.1088/1742-6596/2265/2/022031.

[27] R. Braunbehrens, S. Tamaro, and C. L. Bottasso. "Towards the multi-scale Kalman filtering of dynamic wake models: observing turbulent fluctuations and wake meandering". In: *Journal of Physics: Conference Series* 2505.1 (May 2023), p. 012044. DOI: 10.1088/1742-6596/2505/1/012044. URL: https://dx.doi.org/10.1088/1742-6596/2505/1/012044.

[28] R. Braunbehrens, A. Vad, and C. L. Bottasso. "The wind farm as a sensor: learning and explaining orographic and plant-induced flow heterogeneities from operational data". In: *Wind Energy Science* 8.5 (2023), pp. 691–723. DOI: 10.5194/wes-8-691-2023. URL: https://wes.copernicus.org/articles/8/691/2023/.

[29] Tony Burton et al. *Wind Energy Handbook*. 2nd ed. Chichester: Wiley, 2011. ISBN: 978-0-470-69975-1.

[30] Dongfang Electric Company. *China Tests World's Largest Offshore Wind Turbine*. https://www.offshore-mag.com/renewable-energy/news/55294623/dongfang-electric-company-china-tests-worlds-largest-offshore-wind-turbine. Accessed: 2025-09-12. 2025.

[31] Copernicus. *Sentinel-1 Mission Overview*. https://sentiwiki.copernicus.eu/web/sentinel-1. Accessed: 2025-06-06. 2024.

[32] A. Crespo and J. Herna´ndez. "Turbulence characteristics in wind-turbine wakes". In: *Journal of Wind Engineering and Industrial Aerodynamics* 61.1 (1996), pp. 71–85. ISSN: 0167-6105. DOI: https://doi.org/10.1016/0167-6105(95)00033-X. URL: https://www.sciencedirect.com/science/article/pii/016761059500033X.

[33] J Di Cave et al. "Closed-loop coupling of a dynamic wake model with a wind inflow estimator". In: *Journal of Physics: Conference Series* 2767.3 (June 2024), p. 032034. DOI: 10.1088/1742-6596/2767/3/032034. URL: https://dx.doi.org/10.1088/1742-6596/2767/3/032034.

[34] Bughsin' Djath, Johannes Schulz-Stellenfleth, and Beatriz Cañadillas. "Study of Coastal Effects Relevant for Offshore Wind Energy Using Spaceborne Synthetic Aperture Radar (SAR)". In: *Remote Sensing* 14.7 (2022). ISSN: 2072-4292. DOI: 10.3390/rs14071688. URL: https://www.mdpi.com/2072-4292/14/7/1688.

[35] DNV. *Energy Transition Outlook 2024*. Accessed: 2025-06-03. 2024. URL: https://www.dnv.com/energy-transition-outlook/.

[36] G. Evensen. *The ensemble Kalman filter: Theoretical formulation and practical implementation.* eng. 2003 2003.

[37] P. M.O. Gebraad et al. "A Data-Driven Model for Wind Plant Power Optimization by Yaw Control". American English. In: 2014 American Control Conference, ACC 2014 ; Conference date: 04-06-2014 Through 06-06-2014. 2014, pp. 3128–3134. DOI: 10.1109/ACC.2014.6859118.

[38] Pieter M O Gebraad and J W van Wingerden. "A Control-Oriented Dynamic Model for Wakes in Wind Plants". In: *Journal of Physics: Conference Series* 524.1 (June 2014), p. 012186. DOI: 10.1088/1742-6596/524/1/012186. URL: https://dx.doi.org/10.1088/1742-6596/524/1/012186.

[39] PMO Gebraad et al. "Wind plant power optimization through yaw control using a parametric model for wake effects - a CFD simulation study". English. In: *Wind Energy* 19.1 (2016), pp. 95–114. ISSN: 1095-4244. DOI: 10.1002/we.1822.

[40] Kester Gunn. *Wind Turbine Wakes and Wake Mitigation*. 2025. URL: https://uk.rwe.com/press-and-news/uk-stat.

[41] Charlotte Bay Hasager et al. "Wind Speed-Up in Wind Farm Wakes Quantified From Satellite SAR and Mesoscale Modeling". English. In: *Wind Energy* 27.11 (2024), pp. 1369–1387. ISSN: 1095-4244. DOI: 10.1002/we.2943.

[42] International Electrotechnical Commission. *Wind energy generation systems – Part 12-1: Power performance measurements of electricity producing wind turbines*. Edition 2.0, published on 2017-03-03. Geneva, Switzerland, 2017. URL: https://webstore.iec.ch/en/publication/26603.

[43] Zahra Jafari et al. "A Novel Method for the Estimation of Sea Surface Wind Speed from SAR Imagery". In: *Journal of Marine Science and Engineering* 12.10 (2024). ISSN: 2077-1312. DOI: 10.3390/jmse12101881. URL: https://www.mdpi.com/2077-1312/12/10/1881.

[44] Prof. Dr. Clemens Jauch and Arne Gloe. *Simulation Model Design and Validation of a Gearless Wind Turbine – For Fast Power Control to Enhance Congestion Management*. Tech. rep. Accessed via ResearchGate. WETI, Fachhochschule Flensburg, Mar. 2016. DOI: 10.13140/RG.2.1.1697.5766.

[45] N.O. Jensen. *A note on wind generator interaction*. English. Risø-M 2411. Risø National Laboratory, 1983. ISBN: 87-550-0971-9.

[46] Jason Jonkman and Kelsey Shaler. *FAST.Farm User's Guide and Theory Manual*. American English. Other. 2021.

[47] I. Katic, J. Højstrup, and N.O. Jensen. "A Simple Model for Cluster Efficiency". English. In: *EWEC'86. Proceedings. Vol. 1*. Ed. by W. Palz and E. Sesto. European Wind Energy Association Conference and Exhibition, EWEC '86 ; Conference date: 06-10-1986 Through 08-10-1986. A. Raguzzi, 1987, pp. 407–410.

[48] Mark C. Kelly and Sven-Erik Gryning. "Long-Term Mean Wind Profiles Based on Similarity Theory". English. In: *Boundary-Layer Meteorology* 136.3 (2010), pp. 377–390. ISSN: 0006-8314. DOI: 10.1007/s10546-010-9509-9.

[49] Hyun-Goo Kim et al. "Evaluation of SAR wind retrieval algorithms in offshore areas of the Korean Peninsula". In: *Renewable Energy* 65 (2014). SI:AFORE 2012, pp. 161–168. ISSN: 0960-1481. DOI: https://doi.org/10.1016/j.renene.2013.08.013. URL: https://www.sciencedirect.com/science/article/pii/S0960148113004151.

[50] Kwang Ho Kim, Marta Bertelè, and Carlo L. Bottasso. "Wind inflow observation from load harmonics via neural networks: A simulation and field study". English. In: *Renewable Energy* 204 (Mar. 2023). Publisher Copyright: © 2022 The Author(s), pp. 300–312. ISSN: 0960-1481. DOI: 10.1016/j.renene.2022.12.051.

[51] L. Lanzilao and J. Meyers. "A parametric large-eddy simulation study of wind-farm blockage and gravity waves in conventionally neutral boundary layers". In: *Journal of Fluid Mechanics* 979 (2024), A54. DOI: 10.1017/jfm.2023.1088.

[52] Gunner C. Larsen et al. "Wake meandering: a pragmatic approach". In: *Wind Energy* 11.4 (July 2008), pp. 377–395. DOI: 10.1002/we.267.

[53] XiaoMing Li and Susanne Lehner. "Observation of TerraSAR-X for Studies on Offshore Wind Turbine Wake in Near and Far Fields". In: *IEEE Journal of Selected Topics in Applied Earth Observations and Remote Sensing* 6.3 (2013), pp. 1757–1768. DOI: 10.1109/JSTARS.2013.2263577.

[54] S Mahdavi et al. "A new method for speckle reduction in Synthetic Aperture Radar (SAR) images using optimal window size". In: *IOP Conference Series: Earth and Environmental Science* 34.1 (Apr. 2016), p. 012021. DOI: 10.1088/1755-1315/34/1/012021. URL: https://dx.doi.org/10.1088/1755-1315/34/1/012021.

[55] L. de Montera et al. “High-resolution offshore wind resource assessment at turbine hub height with Sentinel-1 synthetic aperture radar (SAR) data and machine learning”. In: *Wind Energy Science* 7.4 (2022), pp. 1441–1453. DOI: 10.5194/wes-7-1441-2022. URL: https://wes.copernicus.org/articles/7/1441/2022/.

[56] NASA Jet Propulsion Laboratory. *Polarimetry | Get to Know SAR – NASA-ISRO SAR Mission (NISAR)*. https://nisar.jpl.nasa.gov/mission/get-to-know-sar/polarimetry/. Accessed: 2025-06-07. 2024.

[57] National Renewable Energy Laboratory. *SOWFA - Simulator for Offshore Wind Farm Applications*. 2025. URL: https://www.nrel.gov/wind/nwtc/sowfa.

[58] S J Ollier, S J Watson, and C Montavon. “Atmospheric gravity wave impacts on an offshore wind farm”. In: *Journal of Physics: Conference Series* 1037.7 (June 2018), p. 072050. DOI: 10.1088/1742-6596/1037/7/072050. URL: https://dx.doi.org/10.1088/1742-6596/1037/7/072050.

[59] Ørsted A/S. *Offshore Wind*. 2025. URL: https://orsted.com/en/what-we-do/renewable-energy-solutions/offshore-wind (visited on 06/03/2025).

[60] Ørsted A/S. *Offshore Wind Measurement & Operational Data*. https://orsted.com/en/what-we-do/renewable-energy-solutions/offshore-wind/offshore-wind-data. Accessed: 2025-06-08. 2025.

[61] Abdalmenem Owda. “Enhancing SAR Data Analyses for Offshore Wind Energy and Coastal Applications”. English. PhD thesis. DTU Wind and Energy Systems, 2024.

[62] Abdalmenem Owda and Merete Badger. “Wind Speed Variation Mapped Using SAR before and after Commissioning of Offshore Wind Farms”. In: *Remote Sensing* 14.6 (2022). ISSN: 2072-4292. URL: https://www.mdpi.com/2072-4292/14/6/1464.

[63] Abdalmenem Owda et al. “Improving SAR wind retrieval through automatic anomalous pixel detection”. In: *International Journal of Applied Earth Observation and Geoinformation* 122 (2023), p. 103444. ISSN: 1569-8432. DOI: https://doi.org/10.1016/j.jag.2023.103444. URL: https://www.sciencedirect.com/science/article/pii/S1569843223002686.

[64] Alfredo Peña et al. *Remote Sensing for Wind Energy*. English. DTU Wind Energy E 0084(EN). Denmark: DTU Wind Energy, 2015.

[65] Fernando Porté-Agel, Majid Bastankhah, and Sina Shamsoddin. “Wind-Turbine and Wind-Farm Flows: A Review”. In: *Boundary-Layer Meteorology* 174.1 (Jan. 2020), pp. 1–59. ISSN: 0006-8314, 1573-1472. DOI: 10.1007/s10546-019-00473-0. URL: http://link.springer.com/10.1007/s10546-019-00473-0.

[66] J. Schneemann et al. “Cluster wakes impact on a far-distant offshore wind farm’s power”. In: *Wind Energy Science* 5.1 (2020), pp. 29–49. DOI: 10.5194/wes-5-29-2020. URL: https://wes.copernicus.org/articles/5/29/2020/.

[67] J. Schneemann et al. “Offshore wind farm global blockage measured with scanning lidar”. In: *Wind Energy Science* 6.2 (2021), pp. 521–538. DOI: 10.5194/wes-6-521-2021. URL: https://wes.copernicus.org/articles/6/521/2021/.

[68] J. Schreiber, A. Balbaa, and C. L. Bottasso. “Brief communication: A double-Gaussian wake model”. In: *Wind Energy Science* 5.1 (2020), pp. 237–244. DOI: 10.5194/wes-5-237-2020. URL: https://wes.copernicus.org/articles/5/237/2020/.

[69] J. Schreiber, C. L. Bottasso, and M. Bertelè. “Field testing of a local wind inflow estimator and wake detector”. In: *Wind Energy Science* 5.3 (2020), pp. 867–884. DOI: 10.5194/wes-5-867-2020. URL: https://wes.copernicus.org/articles/5/867/2020/.

[70] Mohsen Nourbakhsh Soltani et al. “Estimation of Rotor Effective Wind Speed: A Comparison”. In: *IEEE Transactions on Control Systems Technology* 21.4 (2013), pp. 1155–1167. DOI: 10.1109/TCST.2013.2260751.

[71] Justin E. Stopa et al. “Characterizing the Atmospheric Boundary Layer for Offshore Wind Energy Using Synthetic Aperture Radar Imagery”. In: *Wind Energy* 27.11 (Nov. 2024), pp. 1340–1352. DOI: 10.1002/we.2933. URL: https://hal.science/hal-04878514.

[72] Justin e. Stopa et al. “Automated global classification of surface layer stratification using high-resolution sea surface roughness measurements by satellite synthetic aperture radar”. In: *Geophysical Research Letters* 49.12 (2022). Ed. by American Geophysical Union (AGU), e2022GL098686 (11p.) DOI: 10.1029/2022GL098686. URL: https://doi.org/10.1029/2022GL098686.

[73] Jessica M.I. Strickland, Srinidhi N. Gadde, and Richard J.A.M. Stevens. “Wind farm blockage in a stable atmospheric boundary layer”. In: *Renewable Energy* 197 (2022), pp. 50–58. ISSN: 0960-1481. DOI: https://doi.org/10.1016/j.renene.2022.07.108. URL: https://www.sciencedirect.com/science/article/pii/S0960148122011119.

[74] Roland B. Stull. *An Introduction to Boundary Layer Meteorology*. Vol. 13. Atmospheric and Oceanographic Sciences Library. Springer, 1988. ISBN: 978-90-277-2768-3.

[75] Yuko Takeyama et al. “Comparison of Geophysical Model Functions for SAR Wind Speed Retrieval in Japanese Coastal Waters”. English. In: *Remote Sensing* 5 (2013). Open access, pp. 1956–1973. ISSN: 2072-4292. DOI: 10.3390/rs5041956.

[76] Juan-José Trujillo et al. “Light detection and ranging measurements of wake dynamics. Part II: two-dimensional scanning”. English. In: *Wind Energy* 14.1 (2011), pp. 61–75. ISSN: 1095-4244. DOI: 10.1002/we.402.

[77] U.S. Department of Energy. *Wind Turbines: the Bigger, the Better*. https://www.energy.gov/eere/articles/wind-turbines-bigger-better. Accessed: 2025-09-12. 2024.

[78] United Nations Environment Programme. *UNEP Official Website*. Accessed: 2025-06-02. 2024.

[79] A.J.M. Van Wijk et al. "Evaluation of stability corrections in wind speed profiles over the North Sea". In: *Journal of Wind Engineering and Industrial Aerodynamics* 33.3 (1990), pp. 551–566. ISSN: 0167-6105. DOI: https://doi.org/10.1016/0167-6105(90)90007-Y. URL: https://www.sciencedirect.com/science/article/pii/016761059090007Y.

[80] Georges Voronoi. "Nouvelles applications des paramètres continus à la théorie des formes quadratiques. Deuxième mémoire. Recherches sur les parallélloèdres primitifs." In: *Journal für die reine und angewandte Mathematik* 134 (1908), pp. 198–287. URL: http://eudml.org/doc/149291.

[81] Li Wang et al. "Wind turbine wakes modeling and applications: Past, present, and future". In: *Ocean Engineering* 309 (2024), p. 118508. ISSN: 0029-8018. DOI: https://doi.org/10.1016/j.oceaneng.2024.118508. URL: https://www.sciencedirect.com/science/article/pii/S0029801824018468.

[82] DTU Wind, Energy Systems, and World Bank Group. *Global Wind Atlas - Satellite Winds*. Accessed: 2025-06-06. 2024. URL: https://science.globalwindatlas.info/#/map/satwinds.

[83] Ka Ling Wu and Fernando Porté-Agel. "Flow Adjustment Inside and Around Large Finite-Size Wind Farms". In: *Energies* 10.12 (2017). ISSN: 1996-1073. DOI: 10.3390/en10122164. URL: https://www.mdpi.com/1996-1073/10/12/2164.

[84] Patrick Xie et al. "Sensing wind for environmental and energy applications". In: *25th IET Irish Signals & Systems Conference 2014 and 2014 China-Ireland International Conference on Information and Communications Technologies (ISSC 2014/CIICT 2014)*. 2014, pp. 64–69. DOI: 10.1049/cp.2014.0660.